

CALIFORNIA STATE UNIVERSITY, NORTHRIDGE

Formation of Intraplate Seamount Chains by Viscous Fingering Instabilities in the
Asthenosphere Using Low Reynolds Number Miscible Fluids with a Moving Surface
Boundary

A thesis submitted in partial fulfillment of the requirements
for the degree of Masters of Science
in Geology, Geophysics

By

Uchitha Suranga Nissanka Arachchige

May 2016

The thesis of Uchitha Suranga Nissanka Arachchige is approved by:

Dr. Gerald Simila, Ph.D

Date

Dr. Julian Lozos, Ph.D

Date

Dayanthie S. Weeraratne, Ph.D., Chair

Date

ACKNOWLEDGEMENTS

I would like to acknowledge Dr. Weeraratne for all her support, encouragements, ideas, and revisions. I would also like to thank my family for always supporting and encouraging me. Thanks to Dr. Simila and Dr. Lozos for being my patient thesis committee members. A big thank to everyone who helped me out in the lab: Danielle Brand, John Rincon, Bryan Sanchez, Ishara Perera and Jeffrey Ferree. I would also like to acknowledge Marc Parmentier for his revisions and thoughtful insights to this project.

TABLE OF CONTENTS

SIGNATURE PAGE	ii
ACKNOWLEDGEMENTS	iii
LIST OF TABLES	vi
LIST OF FIGURES	vii
ABSTRACT	ix
Chapter 1: INTRODUCTION.....	1
1.1 Motivation.....	1
1.2 Viscous Fingering	7
Chapter 2: METHODOLOGY	11
2.1 Experimental Parameters	11
2.2 Experimental Design.....	12
2.3 Non-dimensional Numbers	17
2.4 Image Analysis.....	20
Chapter 3: RESULTS	23
3.1 Stationary Plate Experiments.....	23
3.1.1 Varying Viscosity Ratio.....	23
3.1.2 Varying Absolute Viscosity.....	26
3.2 Moving Upper Plate Experiments.....	29
3.2.1. Method 1 - Varying Gamma (Γ).....	29
3.2.2. Method 2 - Constant Gamma (Γ).....	38
3.2.3. Method 3 – Varying Plate Spacing.....	39
3.2.4. Method 4 – Varying Fluid Density	43
3.2.5. Method 5 - Varying Ultra-Slow Injection Rate	46
Chapter 4: DISCUSSION	48

4.1. Scaling Laboratory Experiments to the Mantle	48
4.1.1. Gamma (Γ).....	48
4.1.2. Plate spacing (B).....	51
4.1.3. Initiation Radius (R_o).....	53
4.2. Scaling to the Earth using Non-Dimensional Numbers.....	54
4.3. Length Scales and Width of Linear Seamounts in South Pacific	57
Chapter 5: CONCLUSION.....	59
Chapter 6: FUTURE WORK.....	61
REFERENCES	64
APPENDIX A.....	67
APPENDIX B	69
APPENDIX C	85

LIST OF TABLES

Table 2.1. Summary of Experimental Parameter.....	11
Table 2.2. Summary of Fluid Properties.....	19
Table 3.1. Average Wavelength with Plate Spacing.....	43
Table 4.2. Comparison of experiments in the Earth's gamma range.....	51

LIST OF FIGURES

Figure 1.1. Map of volcanic seamount chains on the south Pacific.....	2
Figure 1.2. Gravity anomalies associated with seamount chains.....	3
Figure 1.3. Geochemical enrichment of seamount chains	4
Figure 1.4. Models for the gravity and velocity anomalies	6
Figure 1.5. Formation of Saffman – Taylor instabilities	8
Figure 1.6. Schematic of finger initiation from the fluid-fluid interface	9
Figure 2.1. Schematic of experimental apparatus.....	13
Figure 2.2. Method of analysis for the stationary plate setup.....	21
Figure 2.3. Method of analysis for the moving upper plate setup	21
Figure 3.1. Time evolution of viscous fingers for different VR.....	24
Figure 3.2. Small plate setup-time evolution of number of fingers	24
Figure 3.3. Wavelength and average wavelength versus viscosity ratio	25
Figure 3.4. Finger initiation radius versus viscosity ratio.....	26
Figure 3.5. Finger pattern with the absolute viscosity	27
Figure 3.6. Number of fingers versus viscosity ratio.....	27
Figure 3.7. Wavelength of fingers versus time	28
Figure 3.8. Initiations radius as a function of absolute viscosity	29
Figure 3.9. Time evolution of number of fingers for different gamma (Γ) ratio	30
Figure 3.10. Time evolution of number of fingers for constant fluid injection rate.....	31
Figure 3.11. Time evolution of number of fingers for constant plate velocity.....	31
Figure 3.12. Finger wavelengths for downstream direction	33
Figure 3.13. Finger wavelengths for upstream direction	33
Figure 3.14. Average wavelength of fingers for constant fluid injection	34
Figure 3.15. Average wavelength of fingers for constant plate velocity	35

Figure 3.16. Plot of initiation radius versus gamma ratio.....	36
Figure 3.17. Variation of initiation radius for constant injection rate	37
Figure 3.18. Variation of initiation radius for constant plate velocity.....	37
Figure 3.19. Experiment images for method 2	38
Figure 3.20. Time evolution of finger wavelength for method 2.....	39
Figure 3.21. Experimental images for varying plate spacing	40
Figure 3.22. Plot of finger initiation radius versus plate spacing	41
Figure 3.23. Plot of average wavelength versus plate spacing	42
Figure 3.24. Experimental images of fingers with varying fluid density	44
Figure 3.25. Variation of downstream wavelength different fluid densities	45
Figure 3.26. Variation of upstream wavelength different fluid densities	45
Figure 3.27. Plot of initiation radius versus fluid density.....	46
Figure 3.28. Rayleigh Taylor instabilities.....	47
Figure 4.1. Phase diagram.....	50
Figure 4.2. Images of Earth's gamma range	52
Figure 4.3. Scaling the initiation radius	54
Figure 6.1. Streamlines for four regimes	63

ABSTRACT

Formation of Intraplate Seamount Chains by Viscous Fingering Instabilities in the Asthenosphere Using Low Reynolds Number Miscible Fluids with a Moving Surface Boundary

By

Uchitha Suranga Nissanka Arachchige

Master of Science in Geology, Geophysics

Regional seismic tomography studies in the Pacific ocean and continental western U.S show linear bands of low velocity anomalies that are aligned with absolute plate motion and occur beneath volcanic lineaments located within the interior of plates far from plate boundaries. But their origin and the formation are still unclear. Small-scale convection provides one possible explanation for these lineations but does not predict age progressive seafloor volcanism nor progressive enrichment trends that opposes plate motion. I propose a new hypothesis where viscous fingering instabilities form due to hot and wet mantle plumes which rise and discharge into the upper mantle asthenosphere and displace higher viscosity depleted mantle. Here, I consider a physical fluid model which studies the viscous fingering in a Hele-Shaw cell using low Reynolds number miscible fluids. I perform laboratory fluid experiments scaled to the Earth's mantle, with stationary and moving surface plates that use glucose-water solutions with viscosities (μ) from 0.3 to 326 Pas and viscosity ratios (μ_2/μ_1) from 3 to 300. I test the effect of several physical properties including the viscosity ratio, absolute viscosity, gamma (Γ), plate spacing, density difference and ultra-slow fluid injection rate. Viscous fingers are observed to form for all viscosity ratios I consider and after an initial growth period, exhibit a constant

wavelength that depends on several parameters. Fingering wavelength is strongly dependent on plate spacing (and therefore asthenospheric layer thickness) but shows weak dependence on viscosity ratio and injection rate. For the case with a mobile upper plate, I define the flux ratio, Γ , as plume flux to plate velocity which varies from 0.005 to 12700 in our experiments and considers the range expected in the Earth (0.0006 – 56). My laboratory results indicate that fingers align with plate motion both upstream and downstream and indicate longer wavelengths in the downstream direction. Experiments scaled to the Earth's upper mantle show fingers form in the presence of surface plate motion for $\Gamma = 0.5$ if asthenospheric thickness is less than 386 km. The initiation radius, R_o , where fingers first form increases with increasing plate spacing. Scaling to study of the south Pacific seafloor shows fingers should develop for $R_o \leq 350$ km from the plume source. This new geodynamic model for viscous fingering in the asthenosphere links off-axis and rising mantle plumes indirectly to mantle return flow to the spreading centers where they contribute to melting, surface volcanism and the growth and formation of new lithosphere.

Chapter 1 Introduction

1.1 Motivation

Most mountain ranges are located on continental plates and are found adjacent and parallel to the plate boundaries. But there is a special group of seamount chains that are found far from tectonic plate boundaries, in the middle of oceanic plates (Sandwell et al., 1995; Smith & Sandwell, 1997; Forsyth et al., 1998). These intraplate seamounts occur in groups and have a linear, parallel orientation (Figure 1.1). Examples of these intraplate seamounts include the Musicians, the Cross-Grain Ridges, the GLIMPSE/MELT study area and the Foundation seamounts. Alternating bands of linear seismic low velocity anomalies are observed in the upper mantle beneath western North America (Obserbski et al., 2011) as well as beneath the Pacific plate (Weeraratne et al., 2007; Lekic and Romanowicz, 2011) which may indicate the mantle depth extent of these features. The low velocity anomalies are also have associated with linear gravity anomalies (Haxby and Weissel, 1986; Harmon et al., 2011) in the south Pacific that are parallel to the seamounts and absolute plate motion (Figure 1.2). Geochemical analyses of enriched volcanic samples (Mahoney et al., 1994) from seamounts along the Puka Puka ridge shows that enrichment decreases gradually from off-axis to the spreading centers (Figure 1.3). Thus, the origin and the formation of these intraplate seamounts must be different than common mountain ranges formed in a volcanic arc setting. To explain these combined observations I suggest a new mechanism to explain the source of intraplate seamounts by viscous fingering in the mantle asthenosphere. In this model low viscosity, volatile rich mantle material rising from off-axis plume sources is discharged into the upper mantle and transports material laterally towards the spreading center through the asthenosphere. This model may explain the geochemical enrichment, gravity and seismic low velocity

anomalies observed with intraplate seamounts and provide a link between Earth's large scale mantle convection and small scale flow in the upper mantle.

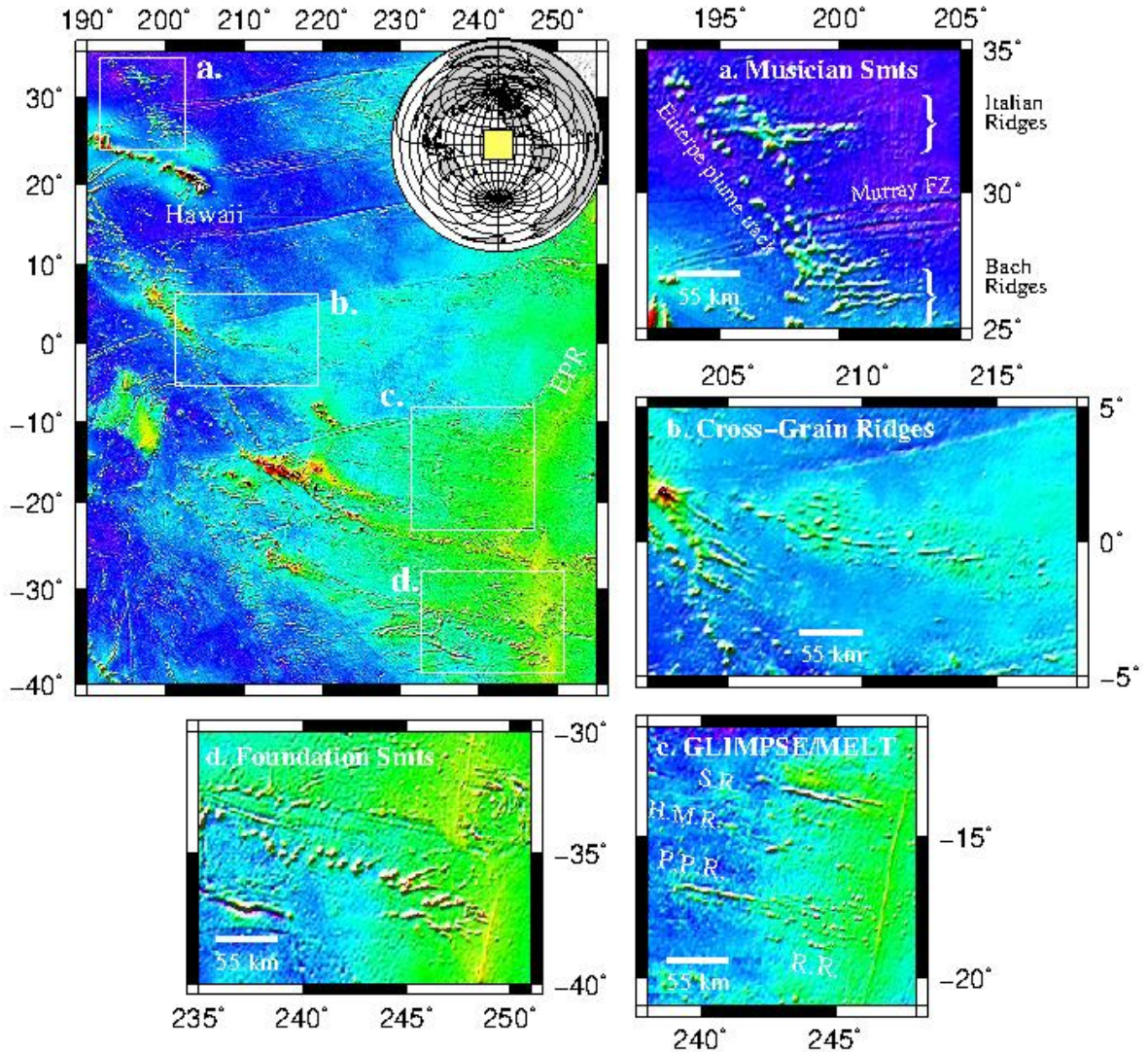


Figure 1.1. Map of volcanic seamount chains on the Pacific seafloor. Linear seamounts are expanded at high resolution shown by black boxes (a) Musician seamounts, (b) Cross-Grain ridges, (c) GLIMPSE/MELT study areas which include the Sojourn ridge (SR), Hotu Matua seamounts (HMR), Puka-Puka ridge (PPR) and the Rano Rahi (RR) seamount field, (d) Foundation seamounts. (After Smith & Sandwell, 1997).

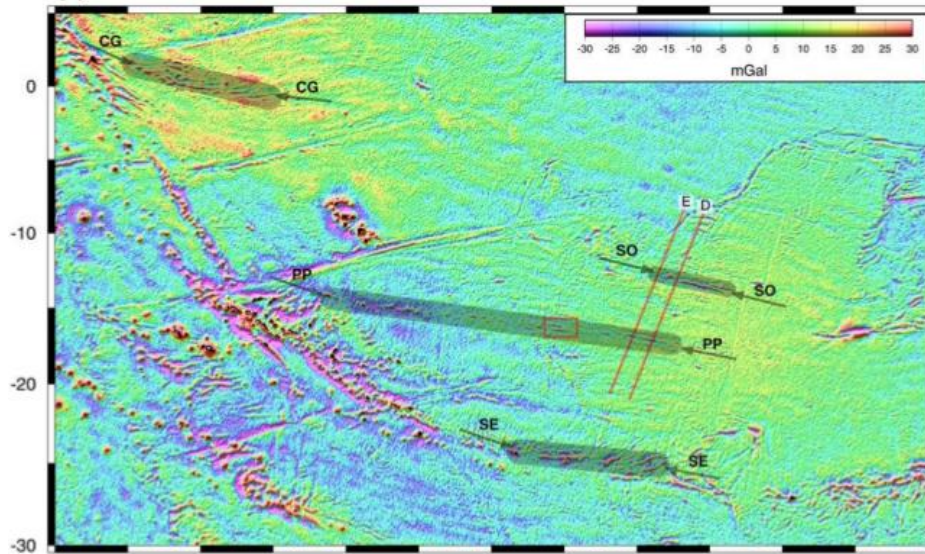


Figure 1.2. Gravity anomalies associated with seamount chains in the south Pacific reveal the close association between the gravity lineaments and the volcanic ridges (Sandwell and Fialko, 2004). Seamounts are superimposed shaded lineations. Red lines are track lines of R/V Conrad where bathymetry and gravity profiles were collected. Red box outlines a part of the Pukapuka ridges that was surveyed by R/V Melville (Sandwell et al., 1995). Prominent volcanic ridges in the area include cross-grain ridges (Winterer and Sandwell, 1987) CG; Pukapuka ridges (Sandwell et al., 1995) PP; the ridges of Searle et al. (1995) SE; and most recently the Sojourn Ridges (Forsyth et al., 2002) SO.

There are few models which explain the origin of intraplate volcanic ridges and gravity lineations. I summarize the five major theories here (Figure 1.4). The first model suggests that mini hot spots are responsible for linear seamounts and volcanic ridges (Fleitout and Moriceau, 1992; Shen et al., 1993). This model accounts for young volcanism occurring on the Pacific plate close to the east Pacific rise. The apparent nature of the flows and their younging direction towards the ridge axis are in accordance with the mini hotspot model. However, based on reliable $^{40}\text{Ar}/^{39}\text{Ar}$ age dating of dredged basalts from the Puka Puka ridge, a mini-hotspot cannot have formed the whole seamount system because the observed ages are inconsistent with this model. The Puka Puka ridge propagation estimated from this geochemical data is shown to be faster than the Pacific plate motion (Sandwell et al., 1995; Janney et al., 2000). Also, two or more aligned

hotspots (Sandwell et al., 1995) were unable to explain the direction of the gravity lineations and ages of the volcanic ridges.

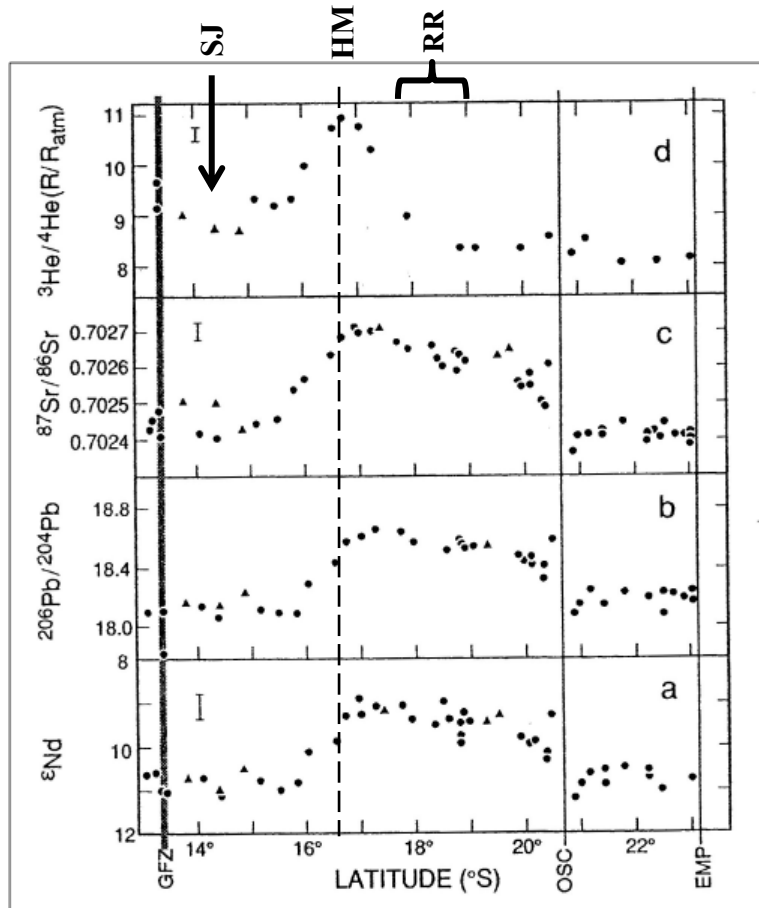


Figure 1.3. Geochemical enrichment of seamount chains (Mahoney et al., 1994). Isotopic variations versus latitude for axial lavas: (a) ϵ_{Nd} , (b) $^{206}Pb/^{204}Pb$, (c) $^{87}Sr/^{86}Sr$ and (d) $^3He/^4He$. Dots = N-MORBs; triangles = T-MORBs; vertical lines running through all panels = latitudes of the Garrett Fracture Zone (GFZ), 20.7°S OSC, and northern boundary of the Easter Microplate (EMP). Geochemical samples along the EPR show strong anomaly at Hotu Matua (HM), Sojourn Ridges (SR) and Rano Rahi (RR).

Small scale convective instability (Richter and Parsons, 1975; Haxby and Weissel, 1986; Buck, 1986; Ballmer et al., 2010) in the upper mantle is another long standing model to explain surface observations. In this model, convection occurs by two possible methods, as negatively buoyant instabilities dripping from a cooling and thickening upper thermal boundary layer (Jha et al., 1997), or instabilities within a melt rich asthenosphere

which are aligned into linear rolls by shear in the asthenosphere between the plate and the upper mantle cause the small scale convection. Although Buck and Parmentier (1986) have shown that these convective instabilities may form beneath seafloor ages as young as 5 Ma, formation at these young ages has been questioned on the basis of laboratory fluid studies (Daville and Jaupart, 1994). Studies of gravity and topography near the East Pacific Rise (EPR) have argued for convective instability (Harmon et al., 2003). Geochemical enrichment of volcanic samples (Mahoney et al., 1994; Donnelly et al., 2003) in this area cannot be simply explained by these upper mantle convective instabilities which predict flow that originates from the spreading axis and travels off-axis with time.

Another model uses lithospheric extension/stretching or boudinage to explain the elongate Cross-Grain ridges located on, or close to, the crest of lineated gravity highs on old sea floor (Winterer and Sandwell, 1987). In this model, a roughly north-south oriented tensional stress applied to the Pacific plate from the far field at plate boundaries would produce short wavelength swells and pinches in the lithosphere that are aligned in the direction of gravity lineations. This model indicates that most of the applied strain is accumulated in the topographic troughs. So that lithospheric extension or boudinage are expected to allow preexisting melt to percolate through lithosphere cracks on the ocean floor. Low velocities which extend to 100 km depth within the asthenosphere, however, are not consistent with this model. This model contradicts the idea of small scale convective instability theory.

Another model considers thermal contraction and states that thermo-elastic bending stresses produce lithosphere failure in the trough of the plate undulations (Gans et

al., 2003). Removal of preexisting melt to form volcanic ridges would cause anomalously high seismic velocities, but recent findings for low shear wave anomalies (Weeraratne et al., 2007; Lekic and Romonowicz et al., 2012; Harmon et al., 2008, 2011) observed in the upper mantle beneath volcanic ridges have argued these models.

Here, I propose a new geodynamic model considering viscous fingering instabilities in the Earth's mantle asthenosphere (Weeraratne et al., 2003, 2007), which forms when hot, volatile rich mantle material is produced from an off-axis mantle plume travels toward spreading centers through the asthenosphere. In this model laboratory experiments were used with high viscosity miscible fluid that scale to the Earth's upper mantle, which determine the characteristic behavior of the viscous fingering in the asthenosphere.

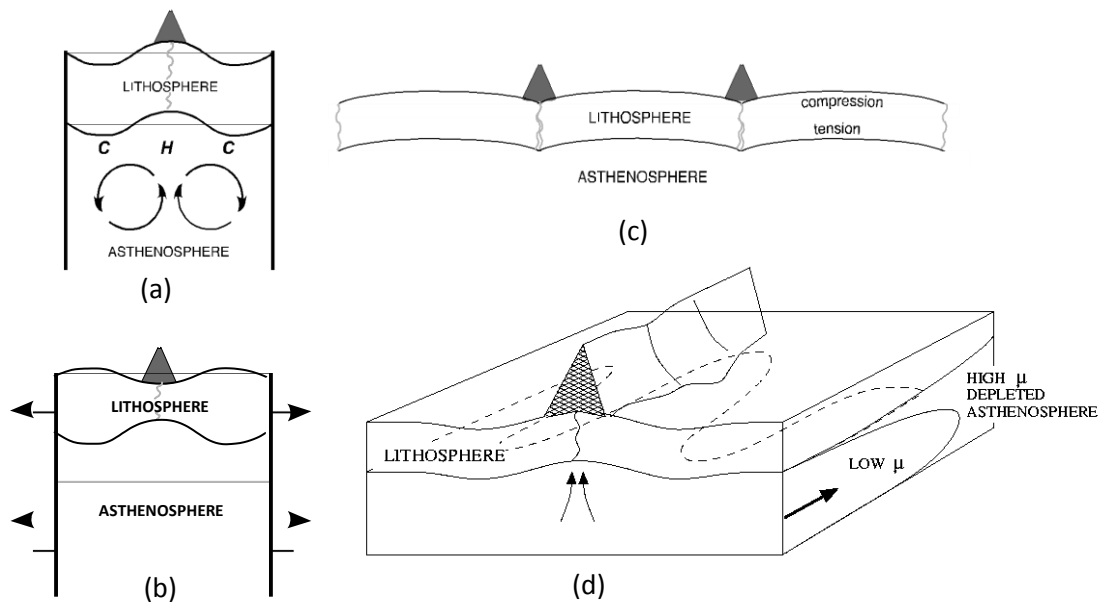


Figure 1.4. Conceptual models for formation of seamount chains and gravity lineations in the South Pacific. (a) Small-scale convection (Haxby and Weissel, 1986), (b) Lithospheric extension and cracking (Winterer and Sandwell, 1987), (c) Thermoelastic bending and cracking (Gans et al., 2003), (d) Viscous fingering instabilities showing low viscosity mantle intruded into a higher viscosity asthenosphere (Weeraratne et al., 2003b). Modified from Weeraratne et al., (2007)

The viscous fingering model is consistent with low velocity anomalies beneath the linear seamount chains in the Pacific plate (Lekic and Romanowicz, 2011) and geochemical anomalies observed along spreading ridge axes associated with nearby hotspot locations (Mahoney et al., 1994; Schilling et al., 2003). But this model did not consider the fingering instabilities for the case of moving upper plates to simulate plate motion in the Earth.

In my study, described here, I examine mantle flow in the form of viscous fingering beneath the oceanic plates simulated in the laboratory in the presence of a moving upper boundary. I expect to determine the influence of properties such as flow rate, fluid layer thickness, viscosity ratio and the ratio of plume flux to the plate velocity for the viscous fingering experiments with high viscosity miscible fluids.

1.2 Viscous Fingering

Viscous fingering occurs when a low viscosity fluid is injected into higher viscosity fluid. An initial planer interface forms between two viscous fluids that grow unstable in the presence of a pressure gradient in the flow direction (Figure 1.5). This instability is known as a Hill instability or more commonly as a Saffman-Taylor instability (Hill, 1952; Saffman and Taylor, 1958; Chouke et al., 1959) and was first observed in miscible fluids by Hill (1952) for sugar solutions. In this case fingering patterns are driven by the differences in viscosity and influenced by the diffusive mixing between the fluids (Homsy, 1987).

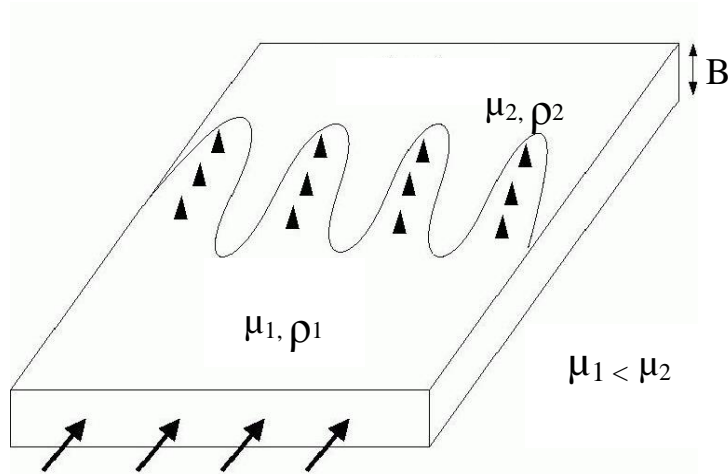


Figure 1.5. Low viscosity fluid (fluid 1, μ_1) displaces high viscosity (fluid 2, μ_2) fluid and form fingers as a result of Saffman-Taylor instabilities. Fingers are forming in the fluid injection direction (black arrows) due to the applied pressure gradient described by the Darcy flow. B is the plate spacing.

Saffman and Taylor (1958) first studied the fingering instabilities for immiscible fluids. Surface tension plays a major role in controlling the wavelength of fingering for the immiscible fluids. The governing equations for Saffman-Taylor instabilities are described in following equations considering an applied pressure gradient for Darcy flow,

$$\frac{dP}{dx} = \rho g - \mu U / b^2 \quad (1)$$

For a two component horizontal flow,

$$\delta P = \left[(\rho_2 - \rho_1) g \delta x - \frac{(\mu_2 - \mu_1) U}{b^2} \right] \delta x \quad (2)$$

Where, δP is the pressure different, ρ_1 and ρ_2 are the density of injecting and ambient fluid, μ_1 and μ_2 are the viscosity of the injecting and ambient fluid, U is the fluid velocity and b is the layer thickness. Density variations are neglected for horizontal flow (equation 2). So that, the fluid-fluid interface is unstable for $\mu_2 / \mu_1 > 1$ (equation 3) and starts to emerge as a finger from the fluid-fluid interface (Figure 1.6).

$$P = (\mu_2 - \mu_1) U / b^2 \quad (3)$$

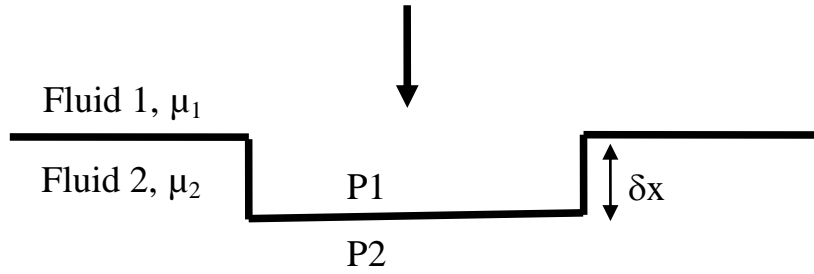


Figure 1.6. Schematic is showing the initiation of the instability at the fluid-fluid interface. Applied pressure gradient due to the fluid injection causes to become the fluid interface unstable forming Saffman-Taylor instability.

Stability analysis by Chouke et al., (1959) showed that smaller wavelengths of maximum instability for high flow rates are controlled by the thickness of the interface between the fluids. According to the studies by Homsy (1987), this interface thickness is expected to be influenced by diffusion and grows with the time the two fluids are in contact. Paterson (1985) considered fingering with miscible fluids and showed that there is a preferred wavelength which minimizes viscous dissipation in the displaced fluid. He showed that the wavelength (λ) of incipient fingers is 4 times the layer thickness (B) and is independent of the injection rate where the subsequent development of fingers is dependent of the injection rate.

Previous studies have considered fingering instabilities in Earth materials. Snyder and Tait (1995) have studied fluid mechanic experiments with the injection of low viscosity, dense magma flow into more viscous, less dense resident magma chambers and observed formation of fingers. These fingering structures are formed by Rayleigh-Taylor instabilities due to the buoyant low density material trapped at the flow front. In this case gravitational instability takes place in the presence of strong shear forces. But, in my study

viscous fingering instabilities occur due to the pressure gradient caused by viscosity contrast and are independent of density variations. Another laboratory study which investigates the magma chamber dynamics has illustrated the development of fingering structures in response to cooling of fluid with temperature-dependent viscosity (Whitehead and Helfrich, 1991).

Fingering instabilities of miscible fluids with a moving upper boundary has not been robustly studied in laboratory experiments. In this study I perform laboratory experiments using low Reynolds number miscible fluids for both stationary and mobile upper plate setup. My experiments will predict the wavelength of fingers that travel through the Earth's asthenosphere with different fluid parameters described above which scaled to the upper mantle and compare results to seismic, gravity and geochemical observations. These experiments are designed to carefully test the fingering instabilities and fluid behavior over a range of fluid properties (Table 1). Tests with stationary plates show that although fingering wavelength is only weakly dependent on viscosity ratio, the radius where the finger initiate show a strong dependence on viscosity ratio and may be important for scaling the Earth's upper mantle. Experiments with mobile upper boundary show fingers travel both upstream and downstream but have a complex finger pattern and fluid behavior compared to the stationary setup. These experiments provide strong evidence for the presence of a thin boundary layer above and/or below fingers. Lastly, I use Particle Image Velocimetry (PIV) visualization method to verify this boundary layer and to gain an insight of particle behavior within each fluid during the experiment.

Chapter 2 Methodology

2.1 Experimental Parameters

Laboratory experiments are performed using a two fluid system (f1 and f2) and varies five experimental parameters during which fluid behavior is quantitatively measured for each case. In each case, I keep all other experimental properties constant and vary one parameter for a subset of experiments. I investigate the viscous fingering instabilities as a function of viscosity ratio (μ_2/μ_1), plate spacing (B), density difference ($\rho_2 - \rho_1$), gamma (Γ), the ratio of the plume flux to the plate velocity and ultra-slow injection rates (Q_u). The range in the variation for each set of parameters is summarized in Table 1.

Parameter	Symbol	Unit
Viscosity Ratio	μ_2/μ_1	–
Plate spacing	B	mm
Gamma	$\Gamma = Q/(VBB)$	–
injection rate	Q	cm ³ /min
Plate velocity	V	cm/min
Density difference	$\Delta\rho = \rho_2 - \rho_1$	g/cm ³

Table.1 Summary of experimental parameters. The viscosity ratio is given by the high viscosity fluid (μ_2) over the low viscosity fluid (μ_1). The gamma (Γ) is defined as the ratio of plume flux (Q) to the plate velocity (V). The density difference ($\Delta\rho$) is given by the density contrast between the density of higher viscosity fluid (ρ_2) and low viscosity fluid (ρ_1).

2.2 Experimental Design

I study the viscous fingering instabilities using radial flow in a Hele-Shaw cell for two cases, with 1) stationary and 2) a moving upper plate. The Hele-Shaw cell is an analog for investigating two dimensional flows within a horizontal channel created by two horizontal plates placed a distance (B) apart. Two experimental designs are used for the stationary plate and moving upper plate experiments. A small plate setup was designed for stationary plate experiments using two horizontal plexiglass plates with dimensions $25.5 \text{ cm} \times 25.5 \text{ cm}$ square and 0.5 cm thickness each which are spaced a distance (B) apart (B is set to 1.65 mm in most cases) separated by metal washers of varying thickness. Experiments with moving upper plates were performed on a large plate setup with plate dimensions $39.5 \text{ cm} \times 39.5 \text{ cm}$ square and 2.5 cm thickness each which are spaced (B) in the range of 0.03 mm to 3.3 mm (Table 2).

In the experimental procedure, I first fill the space between horizontal plates with high viscosity glucose-water (Fluid 2) solution. Then the low viscosity glucose-water (Fluid 1) solution is injected between the two plexiglass plates into the high viscosity fluid through a tube connected to a threaded hole at the center of the lower plate. A custom high pressure Teledyne pump was used with high accuracy ($\pm 0.5 \% \text{ ml}$), in order to accomplish the high pressure and high viscosity fluid injection present between thin plate spacing. In my experiments, I varied the fluid injection rate of the low viscosity fluid from $0.001 \text{ cm}^3/\text{min}$ to $100 \text{ cm}^3/\text{min}$ and the high pressure Teledyne pump allows maintaining a constant injection rate during each experiment. A large LED light panel ($60 \text{ cm} \times 45 \text{ cm}$) was placed above the top plate for lighting and the experiments were performed using this light source to obtain high contrast images. Rapid time-lapse photographs (see schematic)

are taken using a high resolution digital 35mm camera. A mirror oriented at an angle of 45° to the horizontal plates is located few inches below the plates to provide a perfect reflection to the camera mounted on the tripod with a horizontal view to the mirror. Fluid 1 is colored (blue) using food dye and the fluid 2 is a natural translucent yellow hue enhancing the contrast between the two fluids for visualization by the light panel source.

Range of plate velocities scaled to the Earth was obtained using a gear-motor assembly (Figure 2.1) in mobile upper plate experiments. Plate motion was simulated using a thin sheet of mylar and the mylar roll was connected to the gear-motor assembly through the space between horizontal plexiglass plates to get different velocities. To ensure that the plate flexure during the experiments is at minimum and does not affect for the viscous fingering, a high pressure dial caliper was used for both setup. Measured plate flexure at the central point of small and large plate setup was 0.07 mm and 0.03 mm respectively.

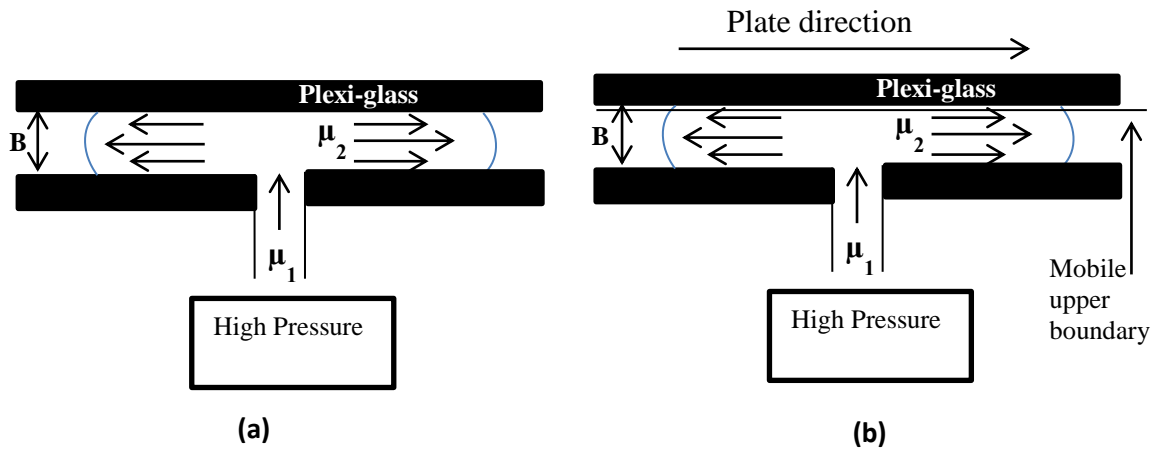


Figure 2.1. Schematic of the experimental apparatus. (a) Stationary plate experiment setup. (b) Experiment setup with moving upper plate. Plate motion is simulated using a moving mylar from left to right just below the top plate.

The fluid materials consist of glucose-water solutions of varying content to produce variations in fluid viscosities. These fluids are miscible, as required for application to the Earth, and surface tension is negligible. To achieve the full range of fluid viscosities for the lab experiments (Table 2), I dilute standard grade corn syrup with varying water concentrations. Pure corn syrup is received from the manufacturer with micro bubbles and is first heated in a hot box which thermally convects providing an even temperature environment that allows evaporation and removal of the micro bubbles. The fluid batch was then mixed with H₂O and allowed to cool to the room temperature. After evaporation and mixing, a portion of the fluid is poured into a graduated cylinder. Density of the fluid is measured using a glass hydrometer and viscosity is measured using the falling ball method for Stokes fluids. Steel balls with different densities and diameters are used for these calculations. The diameter of the graduated cylinder (3.8 cm) is sufficiently large to eliminate the wall effects when measuring fluid viscosities using ball diameter of 6.35 mm. This procedure is repeated 3-5 times for each fluid and providing an average Stokes descent velocity for accuracy. Viscosity of the ambient fluid is then calculated using the Stokes law for a rigid sphere is

$$\mu = 2a^2 \frac{(\rho_b - \rho_f)g}{9v} \quad (4)$$

where a is the radius of the ball, ρ_b and ρ_f are densities of the ball and the fluid respectively, v is the drop velocity and g is gravitational acceleration.

Density of glucose water solution is measured for each experiment to calculate fluid properties such as viscosity, density, etc. Solution is first poured into a graduated

cylinder and kept for a few hours until all air bubbles get evaporated. Density values of my experiments range from 1.02 g/cm^3 to 1.45 g/cm^3 . Ultra slow injection rate (Q_u) experiments are performed in order to consider the possible formation of linear striations within the viscous fingers (Weeraratne et al., 2005 – Ph.D. thesis from Brown), which form by Rayleigh-Taylor instabilities. For this method, the density of high viscosity glucose water solution (Fluid 2) is varied with addition of sodium bromide (NaBr) to obtain high density difference between the fluid 1 and fluid 2. This is achieved by dissolving sodium bromide in water solution to create saturate solutions of varying amounts, then mixing those solutions with pure corn syrup.

Experiments with moving upper boundary are performed using a thin sheet of mylar that is pulled horizontally underneath the upper plate by a gear-motor assembly. Linear velocity of the moving plate (V) is varied from 0.29 cm/min to 80 cm/min and different gear configurations are used to obtain this range of velocities. Diameter of gears is varied from 4.8 cm to 15.4 cm and a motor with 10 rpm is used to facilitate the linear motion of the upper boundary. High viscosity fluid (μ_2) is first poured on to the bottom horizontal plexiglass plate and then the thin sheet of mylar is carefully placed on the high viscosity fluid while avoid air bubbles or air pockets. The mylar is connected to the gear-motor assembly and starts to move at the prescribed linear velocity for each experiment. Injection of fluid 1 is then started from the injection pump. The purpose of this is to perform the fluid injection while the upper plate is moving and to simulate plate motion in the Earth.

Two parameters are varied for stationary plate experiments viscosity ratio (μ_2/μ_1) and absolute viscosity of both fluids. In the first set of experiments, viscosity ratio is varied

(μ_2/μ_1) from 3 to 300. The plate spacing and the injection rate are held constantly for all viscosity ratios. For viscosity ratios 3, 10, 20, 50 and 200 a manual injection method is used with a syringe. The high pressure syringe pump is used to inject the low viscosity fluid (μ_1) for experiments with viscosity ratio 100 and 300. In the second set of experiments, viscosity ratio is held constant at 50 and absolute viscosity of the low (0.006 Pa.s to 5.1 Pa.s) and high (0.3 Pa.s to 267 Pa.s) viscosity fluids is varied accordingly.

Experiments with a mobile upper plate are performed running 5 sets of experiments which varying five different parameters. In the first set of experiments, I vary Γ to describe the relative rates of fluid injection (Q) and plate motion (V), which assess the ratio of mass flux to plate velocity in the upper mantle. Gamma (Γ) is estimated for laboratory experiments using following equation

$$\Gamma = \frac{Q}{VB} \quad (5)$$

where Q is the fluid injection rate, V is the linear velocity of moving mylar and B is the plate spacing. This ratio, Γ , varies from 0.005 to 12700 in my experiments. To scale lab experiments to the mantle asthenosphere, I estimate this non-dimensional ratio for plume flux in Marqueses and Tahitian ocean islands at 3.3 Mg/s (Sleep, 1990) and Pacific plate velocity at 10 cm/y. Calculated gamma ratio for the upper mantle range from 0.0006 to 55.48). In second set of experiments I vary the plate injection and plate velocity keeping gamma constant at $\Gamma=127$. Plate spacing is also kept constant (B=1.65 mm) for above two methods. In the third set of experiments, I vary plate spacing from 0.03 mm to 3.3 mm and hold Γ fixed at 127 (as above). All above methods are performed using viscosity ratio, $\mu_2/\mu_1 = 100$ at room temperature.

A set of experiments are performed varying the density of displacing fluid (μ_2) to identify the influence of density difference on the formation and evaluation of viscous fingering. The density of F2 is varied from 1.382 g/cm³ to 1.45 g/cm³ and the plate velocity, injection rate and gamma ratio are kept constant. For the last set of experiments, I use ultra-slow injection rates (Q_{in}) to consider possible formation of linear striations within viscous fingers. Fluid injection rate is varied from 0.001 ml/min to 1 ml/min and the lowest plate velocity ($v = 0.29$ cm/min) is used for these experiments. Finally a few preliminary experiments are designed and performed to identify the presence of a thin boundary layer above and/or below the fingers. For this, I use Particle Image Velocimetry (PIV) visualization method with silver coated microspheres as tracer particles. First, fluid 2 (μ_2) is seeded with tracer particles and a Helium-Neon (red) laser beam is fired through the space between two plexiglass plates. Then the photographs are taken to analyze the presence of a thin film boundary layer and the particle behavior.

2.3 Non-dimensional Numbers

Several non-dimensional numbers are used to characterize and scale lab experiments to the Earth's upper mantle. I use Reynolds number (Re) to determine the importance of flow regimes of viscous fluids in my experiments. The Reynolds number (Re) is the ratio of inertial forces to the viscous forces

$$Re = \frac{\rho VB}{\mu} \quad (6)$$

where ρ is the fluid density, V is the finger velocity, B is the plate spacing and μ is the viscosity of ambient (displacing) fluid. When Reynolds number $Re \ll 1$, viscous forces

are dominant and inertial forces are negligible. In this case, the behavior of fluid mostly depends on its viscosity and the flow is steady, smooth or laminar, known as Stokes flow. For Reynolds number, $Re \gg 1$, viscous forces are negligible and inertial forces are dominant. In this case the momentum of the fluid determines the behavior and the flow is unstable or turbulent.

Experimental Reynolds numbers range from 1.27×10^{-6} - 4.35×10^{-5} indicating that my experiments are in laminar flow regime. Reynolds number for the upper mantle is calculated by assuming age progression of volcanic samples from Puka-Puka ridge (Sandwell et al., 1995) are formed by asthenospheric flow velocity at 20 cm/y and gives Re in the range of 2×10^{-19} - 2×10^{-21} . This suggests the Earth's mantle's flow regime is laminar flow governed by Stokes velocity. Reynolds numbers in my experiments are higher than calculated for the upper mantle, however, they are much less than one indicating that viscous forces dominate and inertial forces are unimportant and are governed by Stokes flow dynamics in both cases. Thus fluid flow in my experiments and Earth's upper mantle shows laminar flow and are comparable.

The Peclet number (Pe) is the ratio of material transported by advection to the chemical diffusion between fluids

$$Pe = \frac{UB}{D} \quad (7)$$

where U is the finger velocity, B is the plate spacing and D is the chemical diffusion. Diffusion can cause fluids to mix over time and reduce the viscosity difference. This may change the scale of viscous fingering and subdue the development of fingers.

Experimental Peclet number indicates that diffusion is small compared to the flow velocities. Peclet number for the Earth's mantle is range from 1×10^7 to 6.3×10^8 and well represented by the same order of magnitude in my experiments. Laboratory and Earth ranges for fluid properties are summarized in Table 2.2.

Property	Symbol	Unit	Lab	Earth
Viscosity (Fluid 1)	μ_1	Pa S	0.006 - 86.9	$10^{18} - 10^{20}$ *
Viscosity (Fluid 2)	μ_2	Pa s	0.3 - 326.4	$10^{21} - 10^{22}$ *
Viscosity ratio	μ_2 / μ_1	-	3 - 300	$10^2 - 10^4$
Density (Fluid 1)	ρ_1	g/cm ³	1.05 - 1.381	2.2 - 3.2**
Density (Fluid 2)	ρ_2	g/cm ³	1.12 - 1.431	3.3-4.5**
Density difference	$\Delta\rho$	g/cm ³	0.05 - 0.4	1.1-1.2
Layer thickness	B	mm	0.03 - 3.3	$(30-100) \times 10^6$
Plate velocity	V	cm/min	0.29 - 80	$(2.6 - 78) \times 10^6$
Injection rate	Q	cm ³ /min	0.001 - 100	$(9.09-158) \times 10^6$
Gamma	Γ	-	0.005 - 12700	0.0006 - 55.48
Chemical Diffusivity	D	m ² /s	6×10^{-10}	10^{-12} ***
Reynolds Number	Re	-	1.27×10^{-6} - 4.35×10^{-5}	2×10^{-19} - 2×10^{-21}
Peclet number	Pe	-	4.02×10^5 - 1.36×10^8	1×10^7 - 6.3×10^8

Table 2.2 Summary of fluid properties. * Buck and Parmentier (1986), Hirth and Kohlstedt (2003). ** Haxby and Weissel (1986), Sleep (1990). *** Hoffman and Hart (1978)

2.4 Image Analysis

Experimental photographs are taken automatically using a timer and the initial time (t_0) is considered as the time when the low viscosity (μ_1) fluid is first injected to the Hele-Shaw cell. Timing of the photographs is varied according to the fluid injection rate and plate velocity. Images are analyzed to quantify fingering behavior using ImageJ software and each photo is considered for each time frame. Parameters such as the number of fingers, finger wavelength and velocity, stream flow within and surrounding the fingers and finger initiation time are measured as function of time. This is the key to identify fingering behavior and the scale of finger instabilities in my experiments.

Time lapse photographs for the stationary plate experiments are used to analyze the parameters mentioned above. Finger patterns show a radial formation with the stationary plate setup (Figure 2.2). Average radius is the half of the finger length measured from the inner radius. For each time period, average radius and the number of fingers crossing the perimeter are measured and the finger wavelength (λ_f) is then calculated accordingly. For the experiments with moving upper plate, I introduce two new parameters as downstream and upstream fingering. Fingers which grow in the direction of plate motion are considered downstream fingering and fingers which grow in the opposite direction opposing the plate motion are describe as upstream fingering. Wavelength calculation method of the moving upper plate experiments (Figure 2.3) is different from the stationary plate setup due to the elliptical formation of fingers.

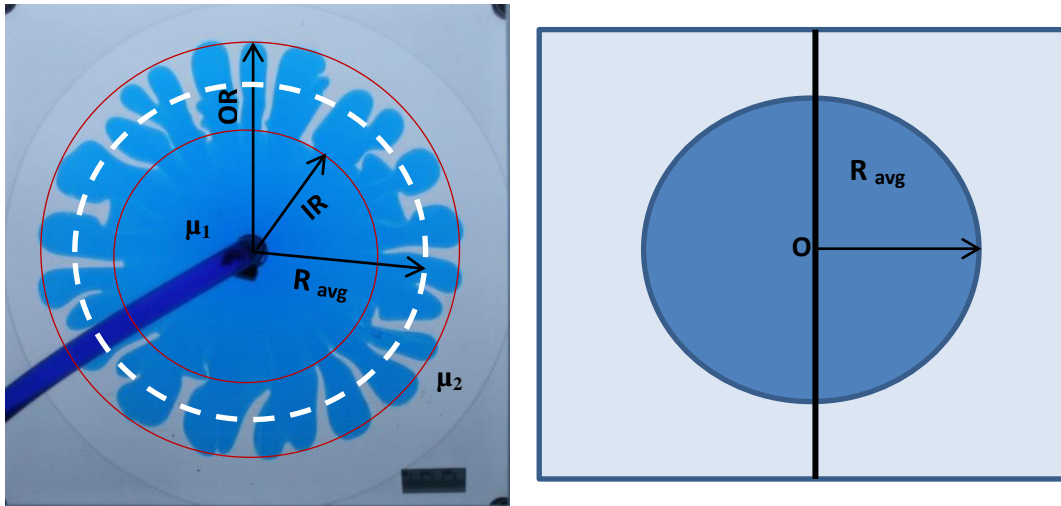


Figure 2.2. Analysis method of viscous fingering for the stationary plate setup. Left) Experiment images showing different radius points considered for the analysis, μ_1 - low viscosity (displacing) fluid, μ_2 – high viscosity (displaced) fluid OR- Outer Radius, IR- Inner Radius, R_{avg} - Average Radius = $(IR+OR)/2$. Right) Method of measuring the finger wavelength (λ), where $\lambda = (2 \pi R_{avg}) / N$. N is the number of fingers crossing the circle with radius R_{avg} . and O is the injection point.

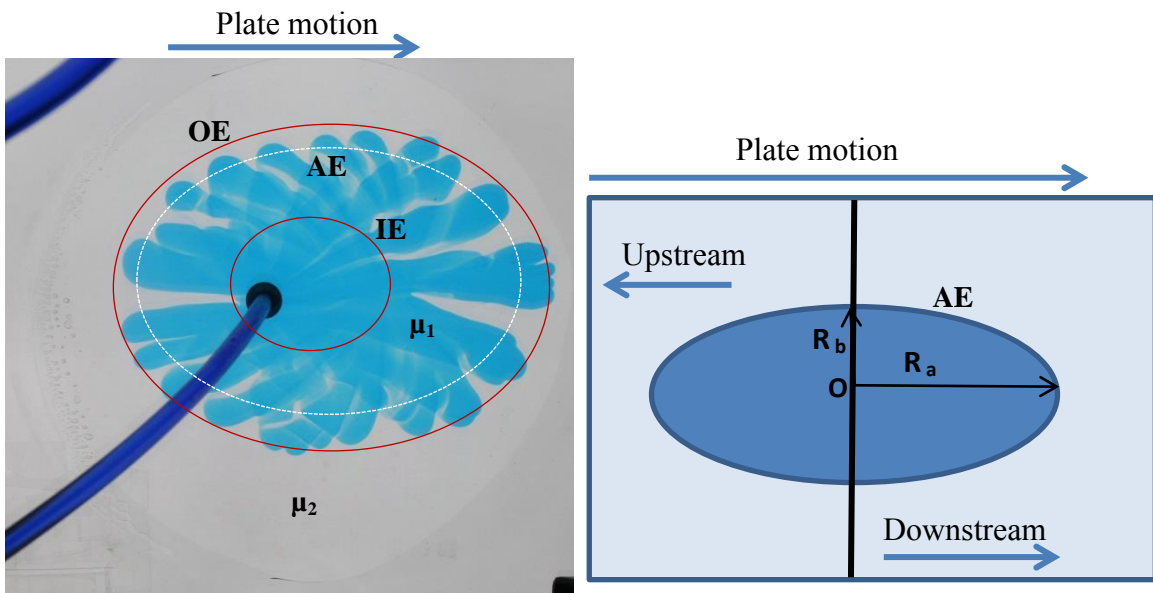


Figure 2.3. Analysis method of viscous fingering for the moving upper plate setup. Left) Experiment image showing different ellipses considered for the analysis, μ_1 - low viscosity (displacing) fluid, μ_2 – high viscosity (displaced) fluid, OE- Outer Ellipse, IE- Inner Ellipse, AE- Average Ellipse (3/4 of finger length). Right) Method of measuring the finger wavelength (λ), R_a and R_b are the major and minor radius of the average ellipse.

Measurements of finger wavelengths are more complicated in mobile upper plate experiments compared to the stationary experiments. The fingering pattern is more elliptical and grows toward both downstream and upstream directions and has reduced finger growth in directions perpendicular to plate motion direction. Fingering wavelength is then calculated for both directions considering a perimeter of an ellipse with radius of $\frac{3}{4}$ of finger length

$$(\lambda_D \text{ or } \lambda_U) = \frac{\left(\frac{P}{2}\right)}{N} \quad (8)$$

where, λ_D is the wavelength of downstream fingers, λ_U is the wavelength of upstream fingers, P is the perimeter of the ellipse with radius of $\frac{3}{4}$ of finger length and N is the number of fingers crossing the perimeter (downstream or upstream).

Chapter 3 Results

I examine the effect of viscosity ratio, plate spacing, flow rate, plate velocity, ratio of plume flux to the plate velocity and density of injecting and ambient fluids on viscous fingering instabilities as well as the length scale and the time scale of viscous fingering. Here, I measure the fluid flow characteristics of fingering such as, time evolution of fingers, wavelength, initiation radius and finger velocity to interpret the formation of intraplate seamount chains and recent tomography results of the oceanic upper mantle in the south Pacific.

3.1 Stationary Plate Experiments

3.1.1. Varying Viscosity Ratio

I conduct a series of experiments that vary viscosity ratio (μ_2/μ_1) of fluid 1 (μ_1) and fluid 2 (μ_2) for both small and large plexi glass plates. I varied the viscosity ratio from 3 to 300 and kept the absolute viscosity of fluids constant. Photographs for the stationary plate experiments are shown in Figure 3.1. Viscous fingers grow in a radial pattern around the injection point and the growth rate of fingers increases rapidly during the initial stage and it slows with time (Figure 3.2). The highest number of fingers occurs for the lowest viscosity ratio and the gradient decreases with increasing viscosity ratio. Time evolution of wavelength for viscosity ratio 3 to 300 is shown in Figure 3.3a. The experiment is ended when the outer fluid reaches to the edge of the plate. The wavelengths of fingers increase with time and reach a steady state (Figure 3.3a). The highest wavelength occurs for the highest viscosity ratio as shown in Figure 3.3b. I calculate average wavelength by selecting a time at which the wavelength of fingers starts to grow at a constant growth

rate. Average wavelengths for these experiments are increasing with increasing viscosity ratio (Figure 3.3b).

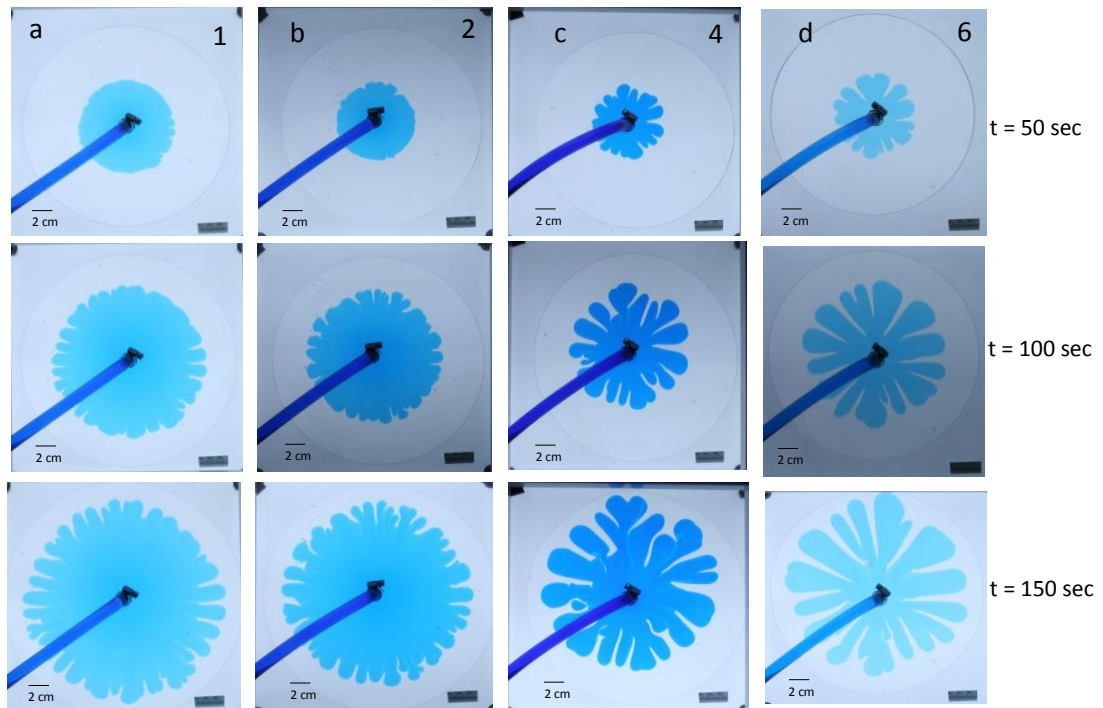


Figure 3.1. Time evolution of viscous fingering for different viscosity ratios (VR). For each experiment I selected photographs for three time values as 50,100 and 150 seconds. Outer white circle is the edge of the high viscosity (μ_2) ambient fluid (fluid 2) and the fluid with dyed blue is the low viscosity (μ_1) injecting fluid (fluid 1). Plate spacing, B is constant at 1.65 mm. The number on upper right corner shows the experiment number (Exp#). a) Exp #1, VR 3. b) Exp #2, VR 10. c) Exp# 4, VR 50. d) Exp #6, VR 200.

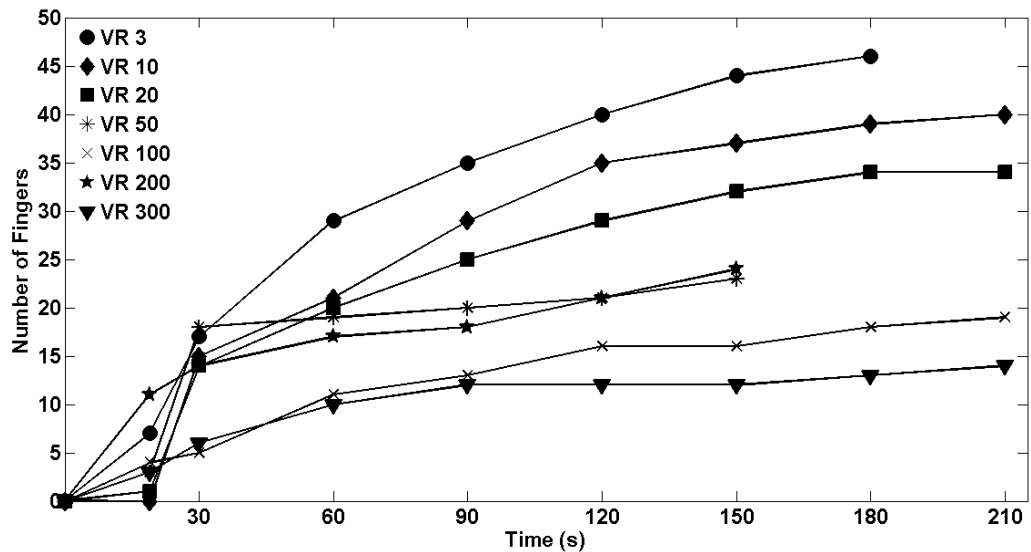


Figure 3.2. The graph of number of fingers versus time. The viscosity ratio (VR) is varied from 3 to 300. In all these experiments plate spacing and fluid injection rate are held constant at 1.65 mm

and 10 ml/min respectively. Solid circles (VR 3) - Exp #1, Solid diamonds (VR 10) - Exp #2, Solid squares (VR 20) - Exp #3, Asterisks (VR 50) - Exp #4, Crosses (VR 100) - Exp #5, Solid pentagams (VR 200) - Exp #6, Solid downward triangles (VR 300) - Exp #7.

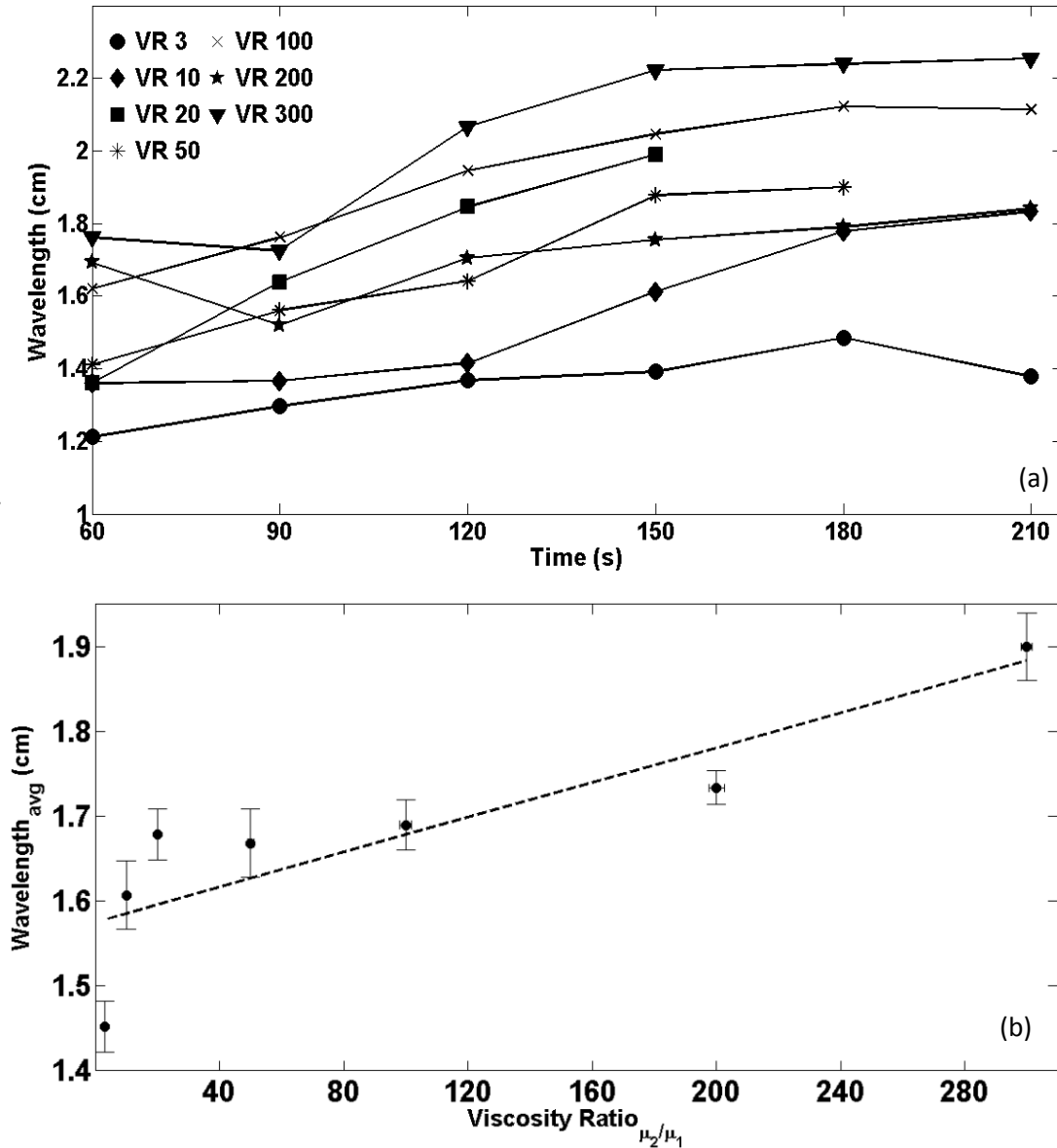


Figure 3.3. a) Wavelength of fingers is plotted as a function of time. The wavelength is calculated using the equation shown in Figure 2.2. First point is considered when the number of fingers starts to show a constant growth rate. Solid circles (VR 3) - Exp#1, Solid diamonds (VR 10) - Exp#2, Solid squares (VR 20) - Exp#3, Asterisks (VR 50) - Exp#4, Crosses (VR 100) - Exp#5, Solid pentagams (VR 200) - Exp#6, Solid downward triangles (VR 300) - Exp#7. b) The average wavelength of fingers as a function of viscosity ratio (VR). Some horizontal error bars are not shown as errors are smaller than the point. The black dash line represents the linear curve fit for the data. VR 3 (Exp #1), VR 10 (Exp #2), VR 20 (Exp #3), VR 50 (Exp #4), VR 100 (Exp #5), VR 200 (Exp #6) and VR 300 (Exp #7).

The initiation radius (R_o), where fingers first start to grow shows different radius values (R_o) with changing viscosity ratio. Initiation radius in my experiments decreases exponentially with increasing viscosity ratio. The highest and the lowest initiation radius occur with the lowest and the highest viscosity ratios respectively (Figure 3.4).

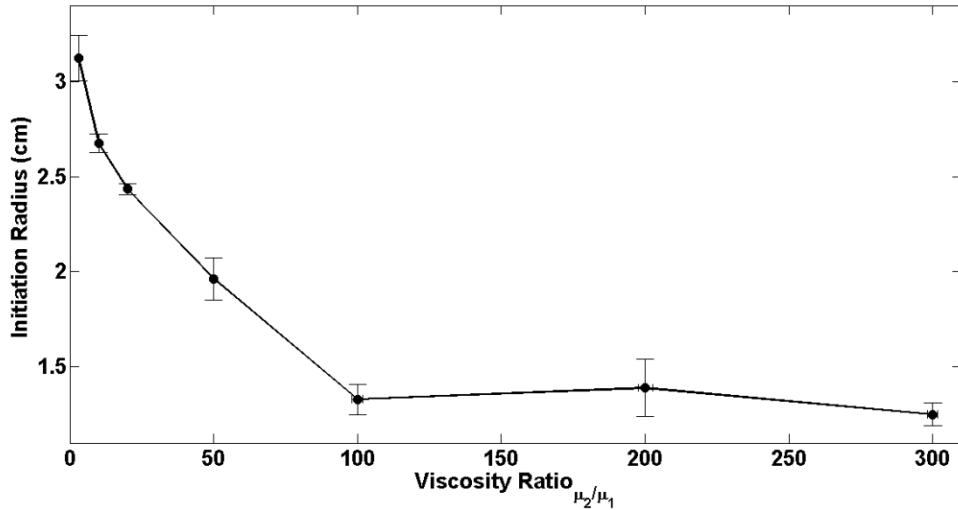


Figure 3.4. Finger initiation radius is plotted versus viscosity ratio. Fluid injection ($Q=10\text{ml/min}$) and the plate spacing ($B=1.65\text{mm}$) is kept constant for all these experiments. Horizontal error bars shown on the graph are not visible as they are smaller than the data points. VR 3 (Exp #1), VR 10 (Exp #2), VR 20 (Exp #3), VR 50 (Exp #4), VR 100 (Exp #5), VR 200 (Exp #6) and VR 300 (Exp #7).

3.1.2 Varying Absolute Viscosity

I investigate the influence of absolute viscosities for the formation and growth of viscous fingers. The series of images in Figure 3.5 demonstrate how the fingering pattern changes as the absolute viscosity of the fluids are increased for a constant viscosity ratio. In these experiments, μ_1 is much less than 1.0 and is essentially inviscid. Most of the variation between experiments then can be dominantly attributed to variations in μ_2 . The number of fingers initially increases rapidly and the growth rate slows with time (Figure 3.6). The experiment with the lowest absolute viscosities (black solid circles) shows the highest number of fingers.

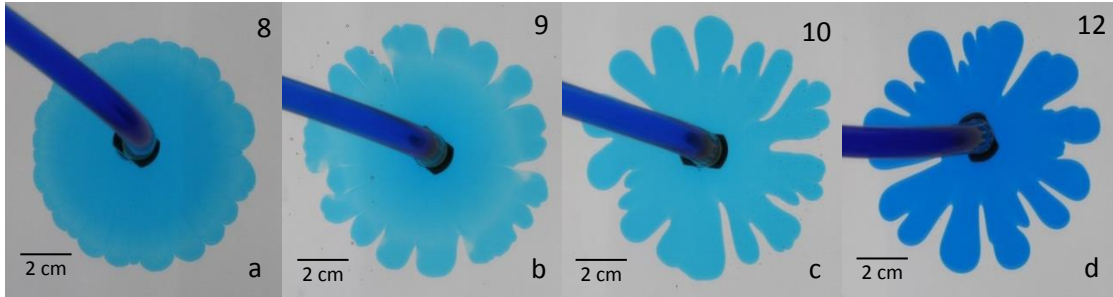


Figure 3.5. Formation of viscous fingers with changing absolute viscosity. For all these experiments, viscosity ratio is constant at 50 and $B = 1.65$ mm. Fluid injection rate (Q) is constant at 3.45 ml/min. The numbers in the upper right corner show experiment number (see appendix A and B). (a) Exp #8, $\mu_1 = 0.006$ Pa.s, $\mu_2 = 0.3$ Pa.s. (b) Exp #9, $\mu_1 = 0.06$ Pa.s, $\mu_2 = 3$ Pa.s. (c) Exp #10, $\mu_1 = 0.6$ Pa.s, $\mu_2 = 26$ Pa.s. (d) Exp #12, $\mu_1 = 5.1$ Pa.s, $\mu_2 = 267$ Pa.s.

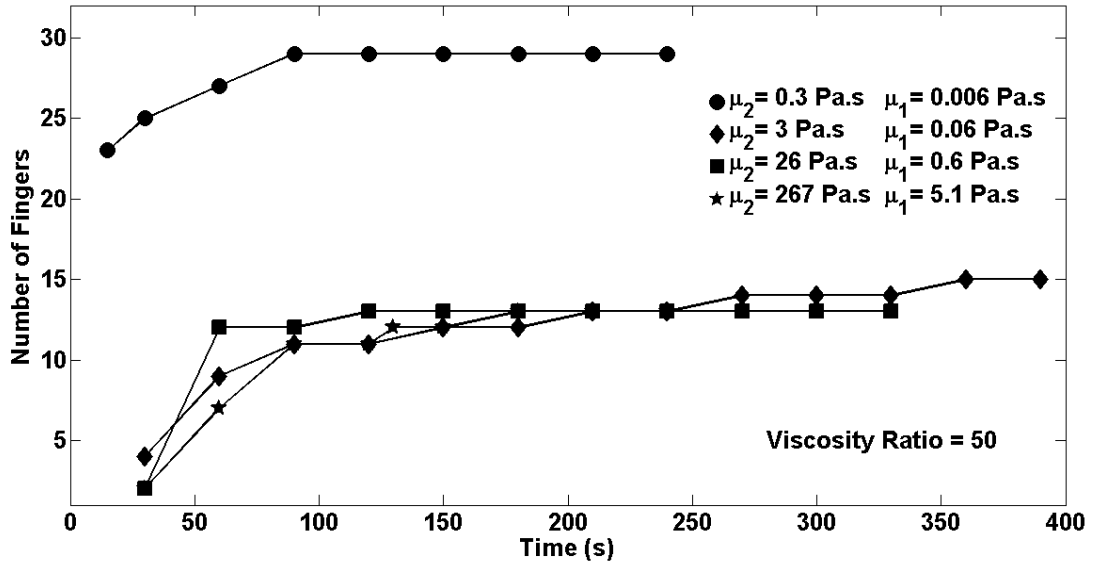


Figure 3.6. Time evolution of number of fingers varying absolute viscosity. All these experiments are performed with constant viscosity ratio ($VR = 50$), fluid injection rate ($Q = 3.45$ ml/min) and plate spacing ($B = 1.65$ mm). Solid circles ($\mu_1 = 0.006$ Pa.s, $\mu_2 = 0.3$ Pa.s)- Exp #8, Solid diamonds ($\mu_1 = 0.06$ Pa.s, $\mu_2 = 3$ Pa.s)- Exp #9, Solid squares ($\mu_1 = 0.6$ Pa.s, $\mu_2 = 26$ Pa.s)- Exp #10, Solid pentagrams ($\mu_1 = 5.1$ Pa.s, $\mu_2 = 267$ Pa.s)- Exp #12.

Experiments which have the highest number of fingers show smaller wavelengths and all wavelengths increase with time. The highest and the lowest wavelengths occur with the highest and the lowest absolute viscosities.

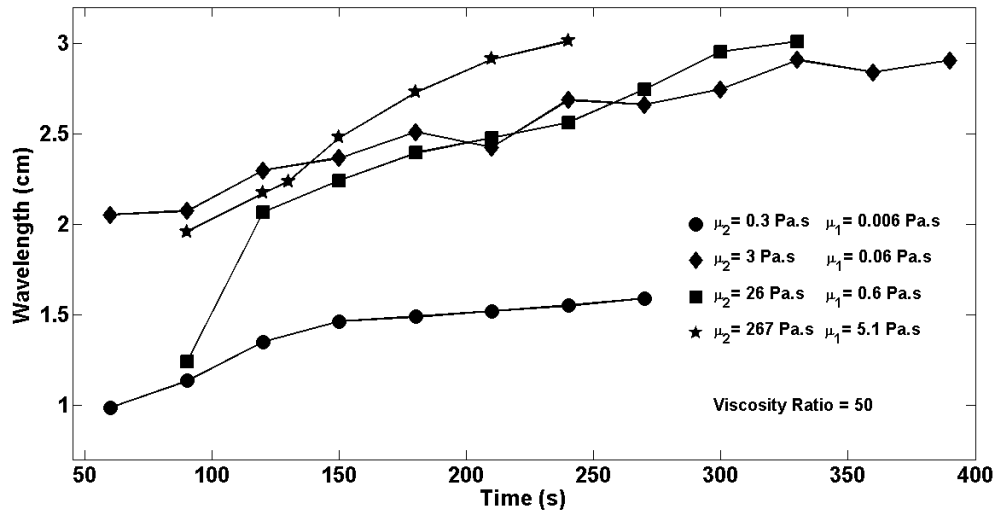


Figure 3.7. Finger wavelength is plotted as a function of time for the absolute viscosities. B and VR are constant for all these experiments at 1.65 mm and 50 respectively. Fluid injection rate is 3.45 ml/min. Solid circles ($\mu_1 = 0.006$ Pa.s, $\mu_2 = 0.3$ Pa.s)- Exp #8, Solid diamonds ($\mu_1 = 0.06$ Pa.s, $\mu_2 = 3$ Pa.s)- Exp #9, Solid squares ($\mu_1 = 0.6$ Pa.s, $\mu_2 = 26$ Pa.s)- Exp #10, Solid pentagrams ($\mu_1 = 5.1$ Pa.s, $\mu_2 = 267$ Pa.s)- Exp #12.

The radius where fingers begin to initiate (R_o) is measured where fingers first start to emerge the concentric circle formed by the fluid 1 – fluid 2 interface. Figure 3.8 shows the variation of initiation radius with absolute viscosity of μ_2 . Fingers start to form at a smaller radius for low absolute viscosities and R_o increases with increasing μ_2 . For this set of experiments initiation radius is independent of viscosity ratio. The pressure difference across the fluid-fluid interface at the highest μ_2 values is damping the growth of fingers and extending the initiation radius. Fingers initiate at small radii without a strong pressure gradient across the fluid-fluid interface. Number of fingers and the wavelength increase with time for both methods and fingering behavior can change within same viscosity ratio but with different absolute viscosity values. Observed finger initiation radius decreases exponentially with increasing viscosity ratio but it increases with increasing absolute

viscosities of both injecting and ambient fluids. These results suggest that the absolute viscosity of fluids or μ_2 influence the length and time scale of viscous fingering when μ_1 is considered to be invicid.

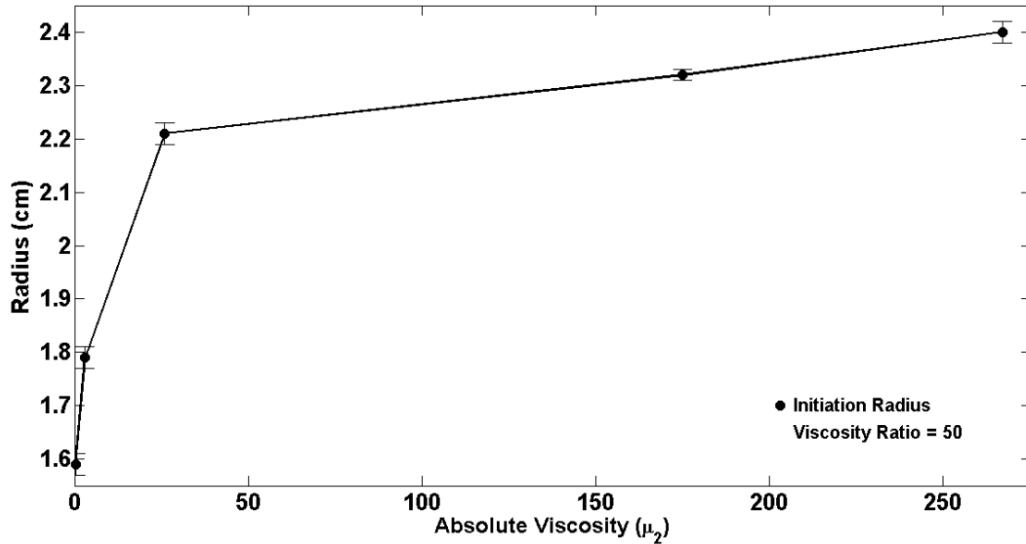


Figure 3.8. Initiation radius is plotted as a function of the absolute viscosity of the fluid 2. Viscosity ratio is held constant at 50 and the absolute viscosity of the ambient fluid is varied from (0.3-267) Pa.s. Fluid injection rate = 3.45 ml/min and the plate spacing is 1.65 mm. Here, μ_2 (0.3 Pas) - Exp #8, μ_2 (3 Pas) - Exp #9, μ_2 (26 Pas) - Exp #10, μ_2 (267 Pas) - Exp #12,

3.2 Moving Upper Plate Experiments

I performed radial fingering experiments with a stationary upper plate to model viscous fingering in the oceanic mantle. I performed five sets of viscous fingering experiments with a mobile upper plate to model viscous fingering with tectonic plate motion over an asthenospheric channel.

3.2.1. Method 1 - Varying Gamma (Γ)

In this method, viscous fingering experiments are performed by varying gamma (see Table 1) and I describe relative rates of fluid injection (Q) and mylar velocity (V_p) using this non-dimensional ratio to scale the ratio of plume flux to plate velocity in the

Earth. Out of 16 experiments only 9 experiments show the formation of non-radial fingers where fluid injection is higher than 1ml/min. Other experiments ($Q < 1\text{ml/min}$) show one linear finger growing only toward the direction of plate motion. The number of fingers initially increases rapidly and growth rate slows with time (Figure 3.9). Experiments with high gamma ratio, where $Q > 10\text{ ml/min}$ and low plate velocities $V < 10\text{ cm/min}$ show rapid growth of fingers at early times that slows at long times and finger growth becomes more steady. Experiments with intermediate plate velocities ($0.29\text{ cm/min} \leq V \leq 10\text{ cm/min}$) and fluid injection rates ($0.001\text{ ml/min} \leq V \leq 10\text{ cm/min}$) show a slow rate and longer period of finger growth. The highest number of fingers occurs with high fluid injection rates. The number of fingers decrease with decreasing injection rate. In this case, fluid injection rate is an important parameter for the finger growth and the fingering wavelength.

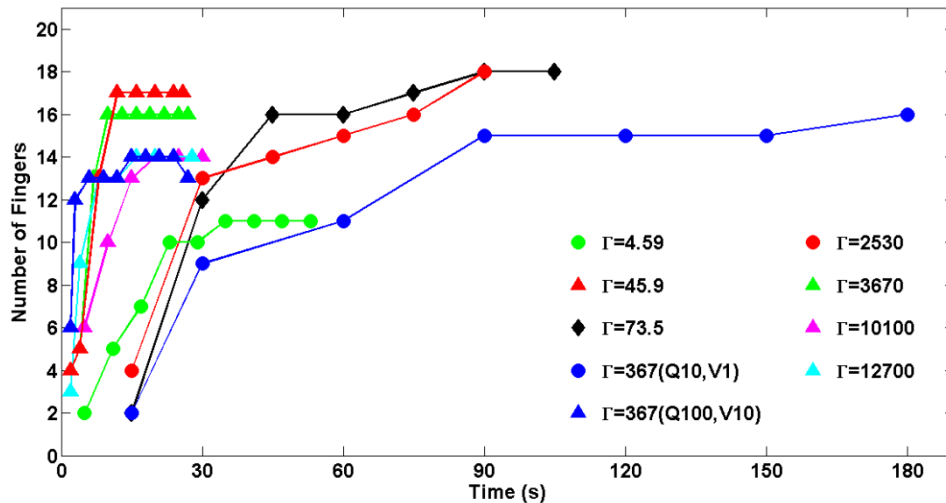


Figure 3.9. Time evolution of number of fingers for different gamma experiments. In the 9 experiments shown above fluid injection and plate spacing are varied and all other physical properties are held constant, where viscosity ratio is 100 and plate spacing is 1.65 mm. Initiation time (t_0) for the experiment is considered as the time at which fluid injection first starts. Gamma is 4.59 (Green circles- Exp #29), 45.9 (Red triangles- Exp #37), 73.5 (Black diamonds- Exp#31), 367- Q10, V1 (Blue circles- Exp #28), 367 – Q100, V10 (Blue triangles- Exp #36), 2530 (Red circles- Exp #32), 3670 (Green triangles- Exp #35), 10100 (Magenta triangles- Exp #33) and 12700 (Cyan triangles- Exp #34).

In order to identify the effect of fluid injection rate and plate velocity on viscous fingering for a moving upper plate system, I performed two sets of experiments varying plate velocity (with Q constant) and fluid injection (with V constant). Figure 3.10 shows the time evolution of fingers for experiments with constant fluid injection rate.

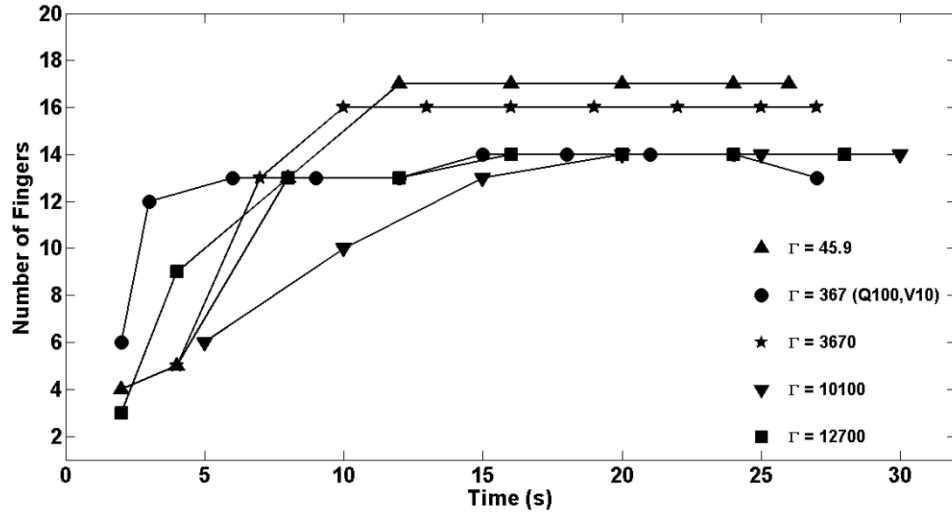


Figure 3.10. Time evolution of fingers for constant fluid injection rate. In all these experiments the injection rate and the plate spacing are constant at 100 ml/min and 1.65 mm respectively. The plate velocity is varied from 0.29 cm/min to 80 cm/min. For $\Gamma = 367$ experiment, Q and V values are given as there is another experiment with the same gamma value ($Q = 10$ ml/min, $V = 1$ cm/min). Gamma is 45.9 (Upside triangles- Exp# 37), 367 (Circles- Exp #36), 3670 (Pentagrams- Exp #35), 10100 (Downside triangles- Exp #33) and 12700 (Squares- Exp#34).

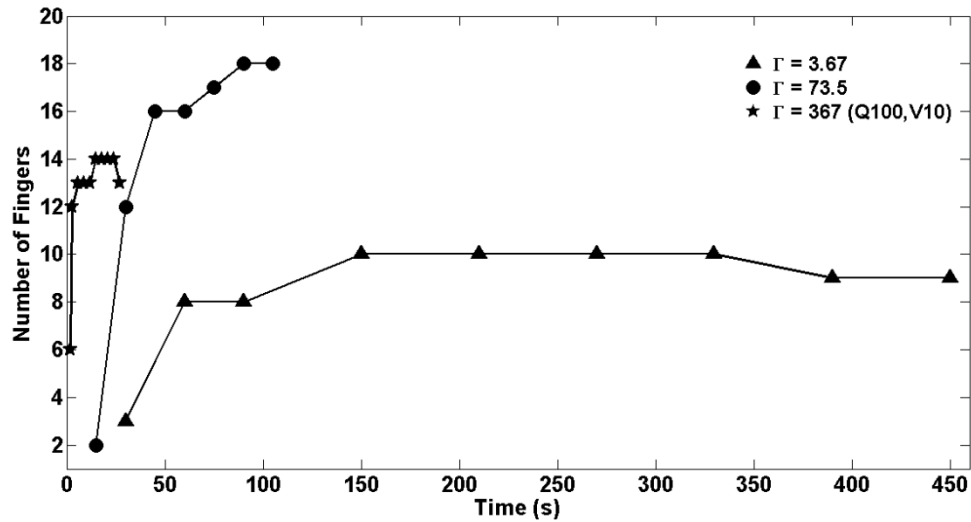


Figure 3.11. Time evolution of fingers for constant plate velocity. Plate velocity and viscosity ratio are constant at 10 cm/min and 100 respectively. Fluid injection is varied from 1ml/min to 100

ml/min. Gamma is 3.67 (Triangles- Exp #27), 73.5 (Circles- Exp #31) and 367 (Pentagrams- Exp #36).

Experiments with low plate velocity values (ex; $\Gamma = 12700$ and $\Gamma = 10100$) show a small number of fingers (square and downward facing triangles) which increases with increasing plate velocity (upward facing triangles). I observe that each experiment reach a time where the number of fingers starts to be constant (steady state). For all five experiments, a steady state number of fingers range from 12 to 16 and shows an increasing pattern with increasing plate velocity. Figure 3.11 shows time evolution of the number of fingers for constant plate velocity for three experiments. The experiment with the lowest fluid injection rate (black solid circle, $Q = 1$ ml/min) shows the lowest number of fingers and it increases with the increasing fluid injection rate.

I calculate the wavelength of fingers for this method using equation 4 (see chapter 2) considering both upstream and downstream directions. Finger wavelength increases with time for all the experiments and there are two dominant slopes for each direction (Figure 3.12 and Figure 3.13). The lower slopes represents low injection rates ($Q < 20$ ml/min) and low plate velocity ($V < 10$ cm/min). The steeper slopes represent high fluid injections ($Q > 80$ ml/min). The experiments with $\Gamma = 73.5$, 367(Q_{10} , V_1), and 2530 show approximately similar gradients compared to the other ratios. The experiments with longer time periods represent slower plate velocities. Thus, the finger wavelength (both downstream and upstream) changes with both fluid injection rate and plate velocity.

Wavelengths for a longer period of time represent small plate velocity and fluid injection rates. Plate dimensions in my experiments restrict the longer growth of viscous fingers for high injection rates and high plate velocities. In order to have viscous fingers

for the whole range of parameters described above, I choose viscosity ratio of 100 after testing several experiments with different viscosity ratios. In all these experiments except $\Gamma = 73.5$, the wavelength of downstream fingers is higher than upstream fingers. This suggests that there are fewer fingers advancing towards the direction of plate motion and a more fingers advancing in the direction opposing plate motion. So the wavelength of fingers depends on the fluid injection rate as well as the plate velocity.

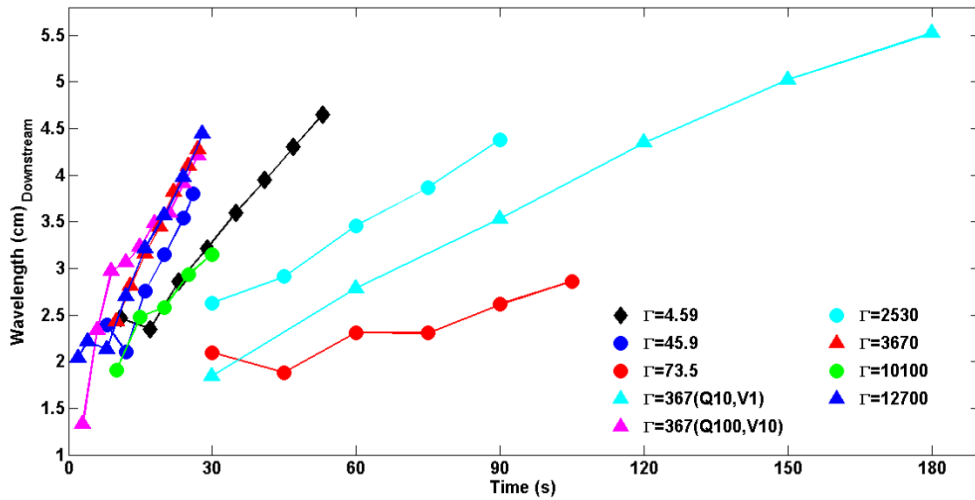


Figure 3.12. Fingering wavelength for downstream (direction of plate motion) fingers with time for different gammas. For all these experiments plate spacing ($B=1.65$ mm) and viscosity ratio ($VR = 100$) are constant. Gamma is 4.59 (Black diamonds- Exp #29), 45.9 (Blue circles- Exp #37), 73.5 (Red circles- Exp #31), 367 – Q10, V1 (Cyan triangles- Exp #28), 367 – Q100, V10 (Magenta triangles- Exp #36), 2530 (Cyan circles- Exp #32), 3670 (Red triangles- Exp #35), 10100 (Green circles- Exp #33) and 12700 (Blue triangles- Exp #34).

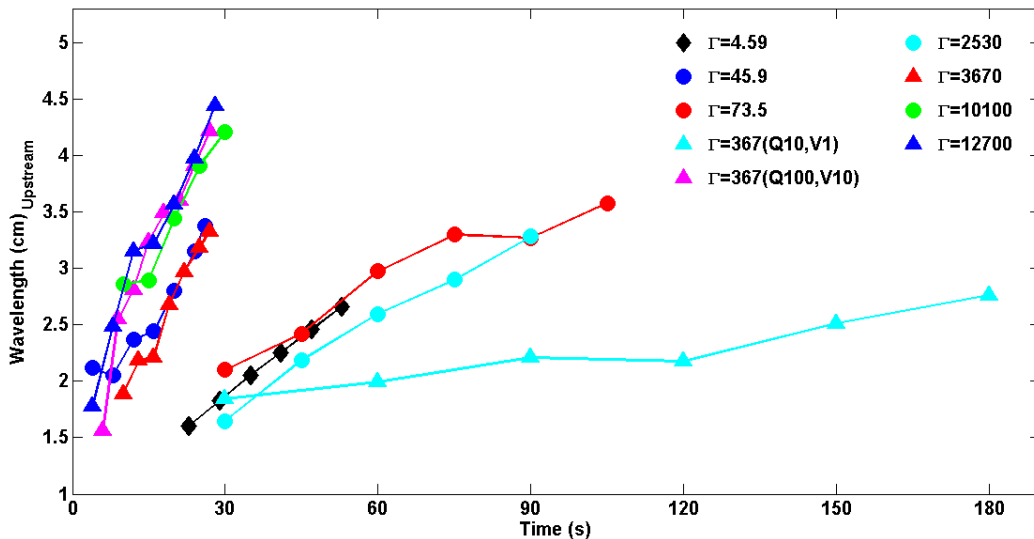


Figure 3.13. Fingering wavelength for upstream (direction of plate motion) fingers with time for different gammas. For all these experiments plate spacing ($B=1.65$ mm) and viscosity ratio ($VR = 100$) are constant. Gamma is 4.59 (Black diamonds- Exp #29), 45.9 (Blue circles- Exp #37), 73.5 (Red circles- Exp #31), 367 – Q10, V1 (Cyan triangles- Exp #28), 367 – Q100, V10 (Magenta triangles- Exp #36), 2530 (Cyan circles- Exp #32), 3670 (Red triangles- Exp #35), 10100 (Green circles- Exp #33) and 12700 (Blue triangles- Exp #34).

Figure 3.14 shows a comparison of the average wavelength for downstream and upstream directions with a constant fluid injection rate. The average wavelength of downstream and upstream directions increases with decreasing plate velocity keeping the downstream wavelength greater than the upstream. The highest value of the average wavelength for both directions occurs for the lowest plate velocity ($V= 0.29$ cm/min). The average wavelength for a stationary experiment with same properties (Figure 3.14, dotted line) is close to the upstream wavelength of the lowest plate velocity. This suggests that, in moving upper plate experiments, the growth of fingers and their wavelengths depends on the velocity of the upper boundary and finger growth is similar to the stationary plate experiments for slow plate velocities.

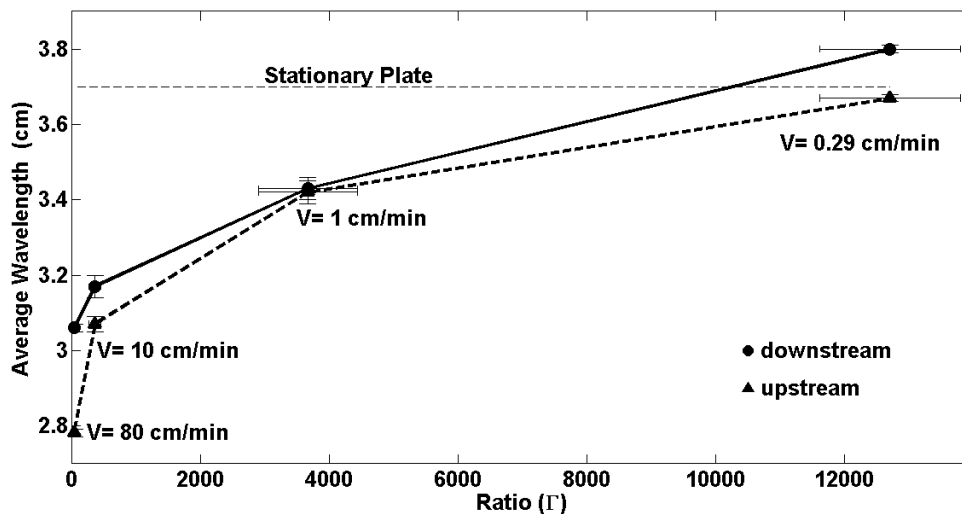


Figure 3.14. Average wavelength of downstream (circles) and upstream (triangles) fingers for constant fluid injection. B and Q are constant at 1.65 mm and 100 ml/min respectively. The error bars on the vertical axis are smaller and show good accuracy with the wavelength measurement. Dotted straight line shows the average wavelength of stationary plate experiment with same parameters. Thick dashed line shows the wavelength for upstream direction. $V = 80$ cm/min- Exp #37, $V = 10$ cm/min- Exp #36, $V = 1$ cm/min- Exp #35, $V = 0.29$ cm/min- Exp #34.

In order to identify the influence of the fluid injection rate on fingering instabilities, I performed four experiments by varying the fluid injection but holding plate velocity fixed. Figure 3.15 shows the behavior of upstream and downstream wavelengths for a constant plate velocity experiments. Only three data points are shown in the figure as the experiment with the lowest gamma value ($\Gamma = 0.36$) did not give measurable fingering patterns because of the low injection rate ($Q = 0.1 \text{ ml/min}$) and high plate velocity ($V = 10 \text{ cm/min}$). The finger wavelength changes slightly with the fluid injection rate, indicating that wavelength has little or no dependence on the fluid injection rate, but it strong dependence on the plate velocity. Fingers which are formed perpendicular to the plate motion turn and bend toward both downstream and upstream directions of moving upper boundary. This decreases the wavelength of fingers with increasing plate velocity for both directions as shown in Figure 3.14.

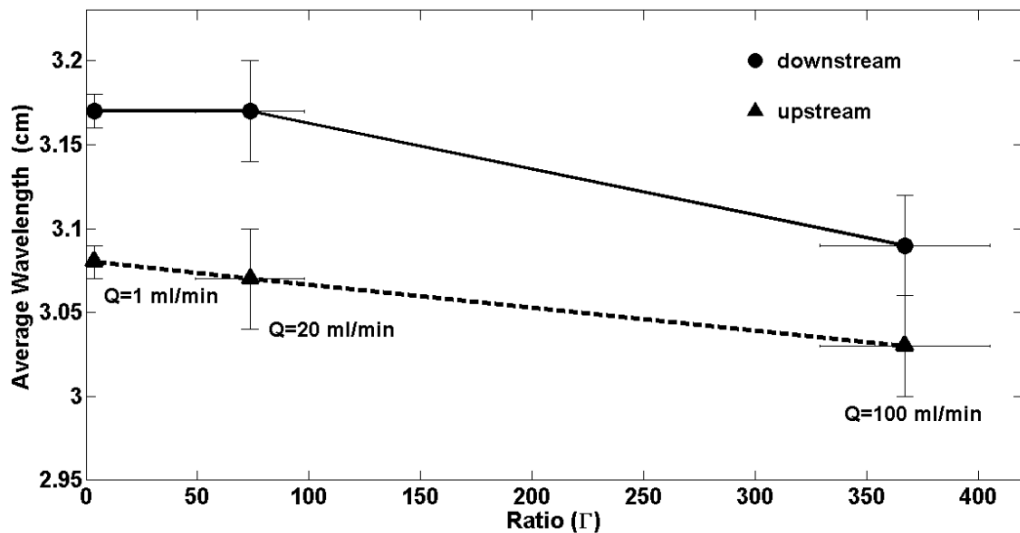


Figure 3.15. Average wavelength of downstream (circles) and upstream (triangles) fingers for constant plate velocity. B and V are constant at 1.65 mm and 10 cm/min respectively. $Q = 1 \text{ ml/min}$ - Exp #27, $Q = 1 \text{ ml/min}$ - Exp #31, $Q = 1 \text{ ml/min}$ - Exp #36. Dashed line shows the average wavelength for the upstream direction.

Figure 3.16 shows the initiation radius for different gammas. The elevated points on the graphs (above 1.8 cm) are the experiments with fluid injection rate less than 20 ml/min. All the points close to a 1.2 cm of initiation radius occur with a high fluid injection rate above 20 ml/min. The initiation radius in my experiments with the moving upper plate slightly depends on the velocity of the overriding plate, but it changes with changing fluid injection rate. Figure 3.17 and Figure 3.18 show the variation of the initiation radius with the plate velocity and the fluid injection rate respectively. The highest and the lowest points on the graph (Figure 3.17) occur with the highest and the lowest velocity of the experiments. In figure 3.18, initiation radius is shown only for injection rates above 1 ml/min because multiple fingers are not observed for $Q < 1$ ml/min with the moving upper plate. The initiation radius decreases with increasing gamma for both cases. But the relative change in the initiation radius is smaller for the experiments with changing velocity compared to the varying fluid injection rate. This suggests that finger initiation depends on both fluid injection rate and velocity of the upper boundary, but the effect is larger for the changes in the fluid injection rate.

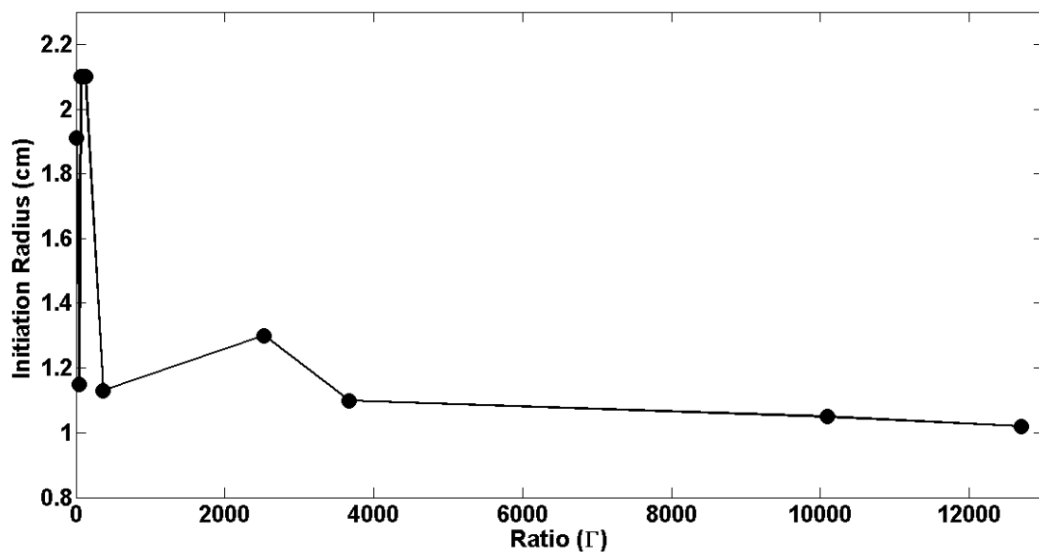


Figure 3.16. Initiation radius (R_o) of fingers plotted as a function of gamma. The viscosity ratio (VR=100) and plate spacing (B=1.65) are constant for all these experiments. The lower points on the graph ($R_o \sim 1.2$ cm) are all the experiments with $Q > 20$ ml/min. Exp #29, $\Gamma = 4.59$. Exp #37, $\Gamma = 45.9$. Exp #31, $\Gamma = 73.5$. Exp #26, $\Gamma = 127$. Exp #36, $\Gamma = 367$. Exp #32, $\Gamma = 2530$. Exp #35, $\Gamma = 3670$. Exp #33, $\Gamma = 10100$. Exp #34, $\Gamma = 12700$.

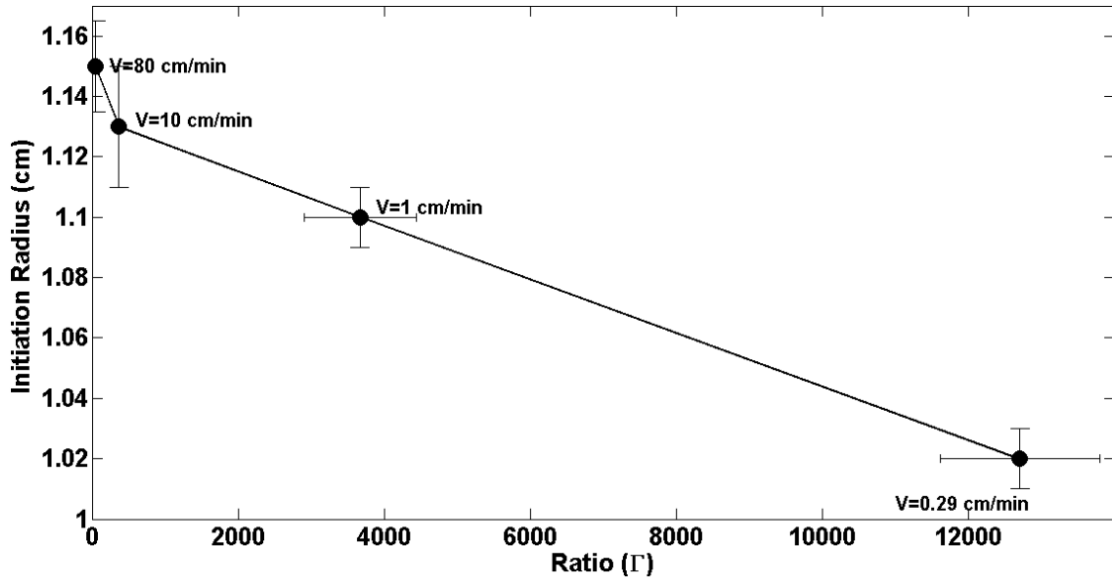


Figure 3.17. The plot of initiation radius (circles) versus gamma for constant fluid injection. B and Q constant for all above experiments at 1.65 mm and 100 ml/min. In this series of experiments, the plate velocity of the upper boundary is varied from 0.29 cm/min to 80 cm/min. V = 80 cm/min- Exp #37, V = 10 cm/min- Exp #36, V = 1 cm/min- Exp #35, V = 0.29 cm/min- Exp #34.

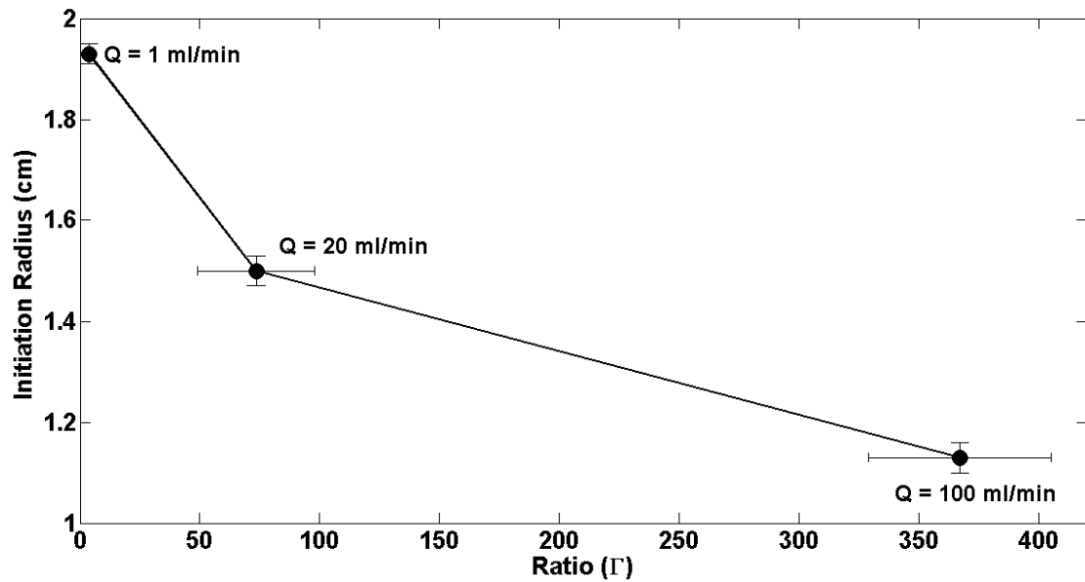


Figure 3.18. The plot of initiation radius (circles) versus gamma for constant plate velocity. B and V are constant for all above experiments at 1.65 mm and 10 cm/min. In this series of experiments, the fluid injection rate varied from 1 ml/min to 100 ml/min. Q = 1 ml/min- Exp #27, Q = 1 ml/min- Exp #31, Q = 1 ml/min- Exp #36,

3.2.2. Method 2 - Constant Gamma (Γ)

In order to test the finger instabilities for a constant gamma in the case of moving upper boundary, I ran a series of four experiments in which I varied fluid injection rate and plate velocity. The fluid injection rate and the plate velocity are chosen to give a constant gamma within the available experiment parameter range. Finger growth increases with time as prescribed and shows a dominant elliptical pattern Figure 3.19.

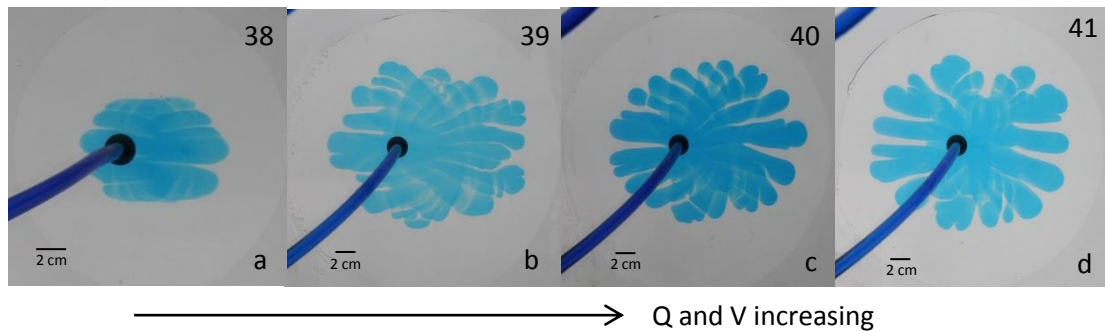


Figure 3.19. The finger growth and the behavior for a constant gamma. The fluid injection rate and plate velocity are varied holding gamma ($\Gamma = 127$) and plate spacing ($B = 1.65$) constant. a) Q = 1 ml/min, V = 0.29 cm/min, Exp #38. b) Q = 3.45 ml/min, V = 1 cm/min, Exp #39. c) Q = 17.1 ml/min, V = 5 cm/min, Exp #40. d) Q = 34.5 ml/min, V = 10 cm/min, Exp #41. The numbers in the upper right corner represents the experiment number (see Appendix A and B).

Fingers first start radially away from the injection point for a small time and turn into both downstream and upstream directions forming an elliptical pattern. The width of the fingers is almost similar to each other and the finger length decreases as fluid injection and plate velocity increase. Finger wavelengths for both downstream and upstream directions show a similar increasing pattern with time as shown in Figure 3.20. The wavelength increases with time due to the slow growth rate and the increasing distance away from the injection rate. The downstream wavelength is slightly higher than the

upstream for experiments with injection rates greater than 3.45 ml/min. Linear fingers travel both downstream and upstream in my experiments and form a complex pattern at later stages of growth. This pattern is completely different from what is observed in the stationary plate experiments. So that it is important to identify the flow behavior within plate spacing B with the moving upper boundary. I explain this flow in moving upper plate experiments using theory of streamlines in the next chapter.

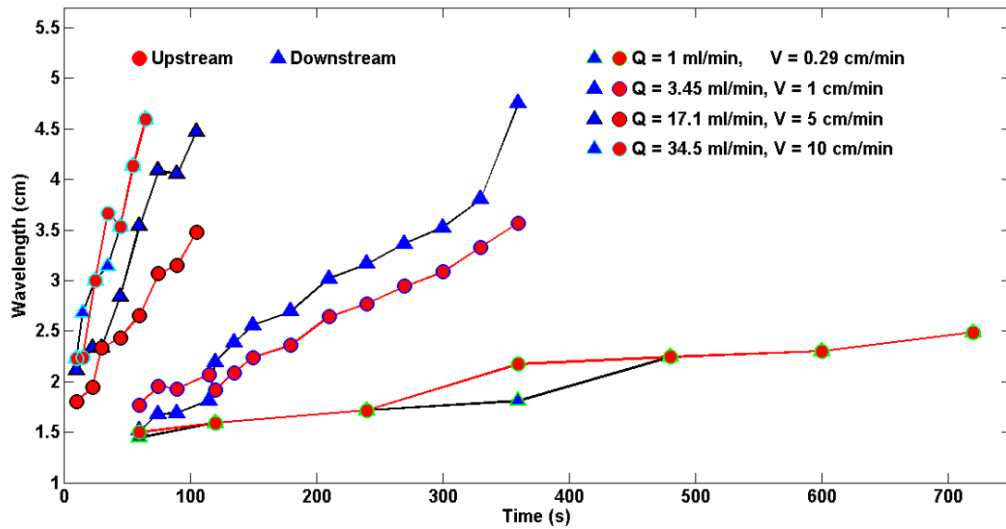


Figure 3.20. Time evolution of downstream and upstream wavelength for four different experiments with constant $\Gamma = 127$. Plate spacing is kept constant at $B = 1.65$ mm. Wavelength of both directions increases with time and the highest gradient observed for the highest fluid injection ($Q = 34.5$ ml/min) and plate velocity ($V = 10$ cm/min). $Q = 1$ ml/min, $V = 0.29$ cm/min (Exp #38). $Q = 3.45$ ml/min, $V = 1$ cm/min (Exp #39). $Q = 17.1$ ml/min, $V = 5$ cm/min (Exp #40). $Q = 34.5$ ml/min, $V = 10$ cm/min (Exp #41).

3.2.3. Method 3 – Varying Plate Spacing (B)

I performed a set of six experiments with moving upper plate to test the fingering behavior for different plate spacing. Increasing the plate spacing should have a large effect on the overall pattern because more volume is required to fill the plate space. As more volume is required to fill the plate spacing, and the volumetric injection rate is constant,

this subsequently leads to a decrease in the effective velocity of the injecting fluid (μ_1). The larger the plate spacing, the slower the effective finger velocity and subsequently thicker the fingers in the pattern that forms. Figure 3.21 shows how the fingers become thicker and how the pattern becomes less complex as the plate spacing increases. I choose images at a time when the fingers in each experiment reach to approximately the same radial distance from the injecting point.

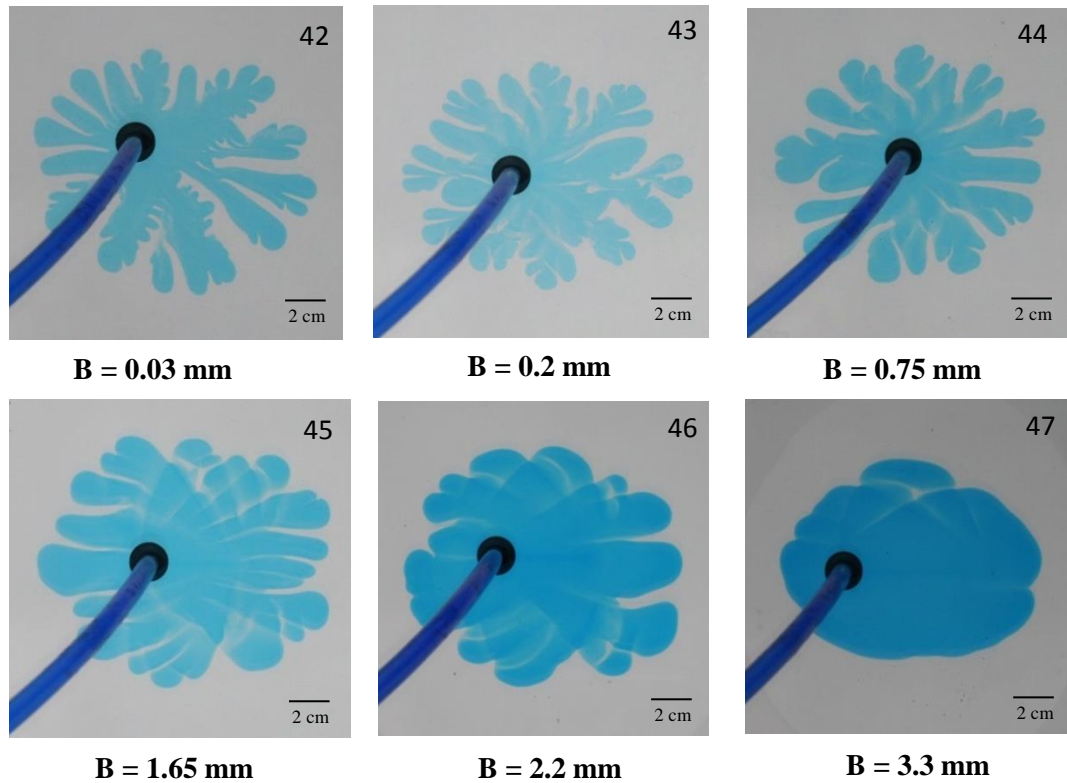


Figure 3.21. Behavior of the finger pattern by varying plate spacing. In this series of experiments, the injection rate is constant at 3.45 ml/min and the plate velocity is fixed at 1 cm/min which gives the gamma constant at 127. The experiment number is given in upper right corner. Exp #42, B = 0.03 mm. Exp #43, B = 0.2 mm. Exp #44, B = 0.75 mm. Exp #45, B = 1.65 mm. Exp #46, B = 2.2 mm. Exp #47, B = 3.3 mm.

The experiment with B = 3.3 mm, well developed fingers do not form as more time and a larger radius are needed to grow separate fingers from the fluid-fluid interface. Finger initiation time should have a great dependence on the plate spacing for constant

fluid injection and plate velocity. Out of six experiments performed in this method, I did not observe well developed longer for the experiment with the largest plate spacing ($B = 3.3$ mm). This occurs because of the low effective velocity of the fingers and high initiation radius in the case of high plate spacing. Finger initiation radius increases with increasing plate spacing (Figure 3.22). The gradient of the line becomes slightly higher after $B = 2.2$ mm. Due to the decreasing effective velocity for the large plate spacing, initiation time also increases with increasing plate spacing.

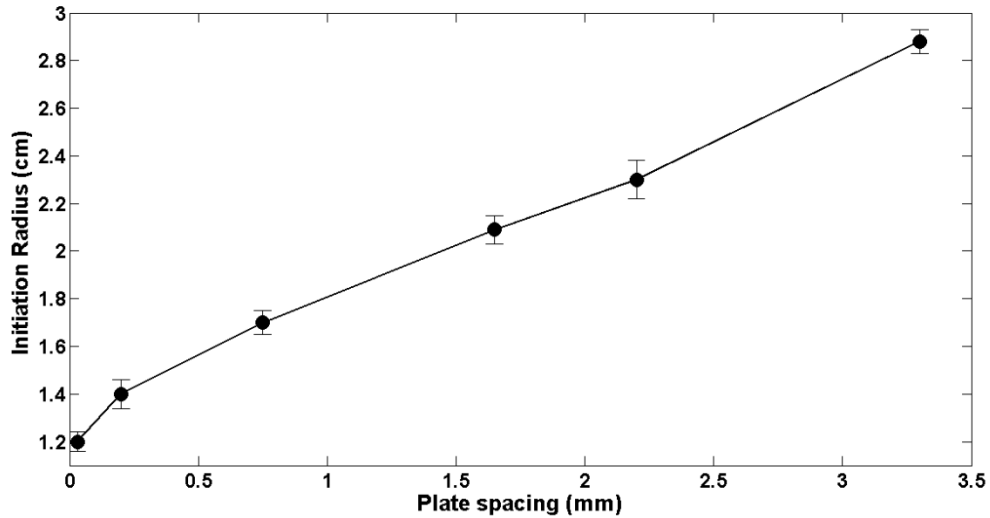


Figure 3.22. Finger initiation radius (circles) is plotted as a function of plate spacing. The plate velocity and the fluid injection are constant at 1 cm/min and 3.45 ml/min for all above experiments. The plate spacing is varied from 0.03 mm to 3.3 mm. $B = 0.03$ mm, Exp #42. $B = 0.2$ mm, Exp #43. $B = 0.75$ mm, Exp #44. $B = 1.65$ mm, Exp #45. $B = 2.2$ mm, Exp #46. $B = 3.3$ mm, Exp #47.

This suggests that for a constant fluid injection and moving upper boundary, the fluid system needs more time and distance away from the injection point to form fingers while increasing plate spacing. For very low gap thicknesses, pressure in the fluid-fluid boundary would cause to start the fingering instability at a low radius.

Tip-splitting, a phenomenon in which the initial stage of fingers split into two or more fingers, can also be observed at lower plate spacing ($B = 0.03$ mm to $B = 0.75$ mm) in both downstream and upstream directions. I do not observe tip splitting for experiments with $B > 0.75$ mm but, fingers tend to form wider and linear in both directions. Visually, a large number of small wavelength fingers and more radial pattern are observed for small plate spacing (Figure 3.21). Small wavelength instabilities are present for a small time and appear to be damped out. In this case, viscous fingering instabilities prevail in moving upper boundary experiments only when the plate spacing is favorable.

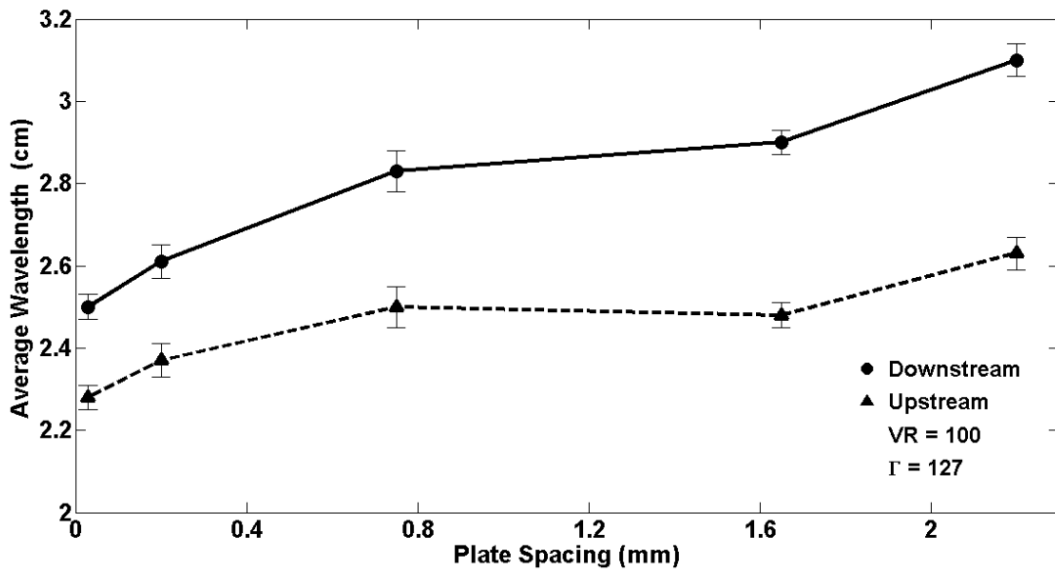


Figure 3.23. Average finger wavelength as a function of plate spacing. The viscosity ratio ($VR = 100$), the plate velocity ($V = 1$ cm/min) and the fluid injection rate ($Q = 3.45$ ml/min) are constant for above experiments. The plate spacing is varied from 0.03 mm to 3.3 mm. The upstream and downstream wavelengths are shown in triangles (dashed line) and circles (solid line) respectively. $B = 0.03$ mm, Exp #42. $B = 0.2$ mm, Exp #43. $B = 0.75$ mm, Exp #44. $B = 1.65$ mm, Exp #45. $B = 2.2$ mm, Exp #46. $B = 3.3$ mm, Exp #47.

The average finger wavelength for this method is shown in Figure 3.23 for both downstream and upstream directions. For both directions, the average wavelength

increases with increasing plate spacing but the individual values are higher in downstream fingers compared to the upstream direction.

B (cm)	λ_{avg} (cm)	$(\lambda/B)_{\text{avg}}$
0.003	2.39	796
0.020	2.49	124
0.075	2.67	36
0.165	2.69	16
0.220	2.82	12

Table 3.1. Table shows measured wavelengths for different plate spacing experiments. Downstream and upstream wavelengths are averaged to get the λ_{avg} and the ratio of average wavelength to the plate spacing is $(\lambda/B)_{\text{avg}}$.

I averaged the wavelengths of the upstream and downstream directions (see Table 3.1). These ratios vary as a multiple of 4 and are consistent with the results of previous studies by Paterson (1985) and Weeraratne et al., (2013). Scaling and the geological implication of this ratio will be discussed in the next chapter.

3.2.4. Method 4 – Varying Fluid Density

I performed a set of fingering experiments in which I varied the density of the high viscosity fluid. In these experiments, I investigated the influence of the fluid density on the formation of viscous fingers with a moving upper boundary. A series of images shown in Figure 3.24 demonstrate how the fingering pattern change as the density variation of the fluids is increased. Approximately same width and wavelengths of fingers occur with increasing the density of the high viscosity fluid. Finger growth shows more controlled behavior on both upstream and downstream, and there is no visible change in the pattern of fingers with increasing fluid density. Fingers tend to form as narrow and travel for

longer distance without changing their width. Tip splitting at the edge of the fingers are not visible in this set of experiments.

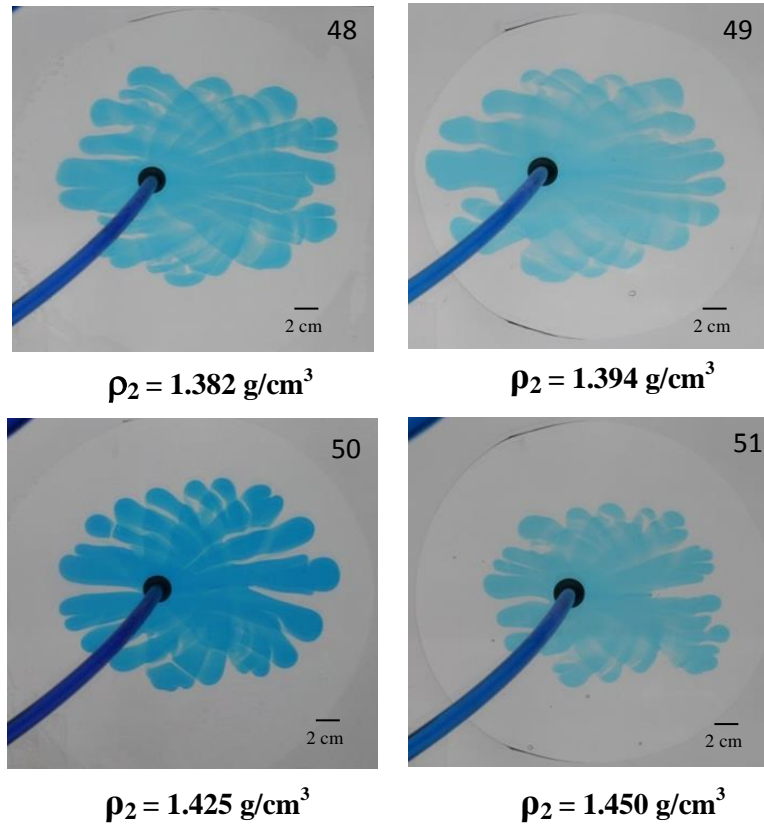


Figure 3.24. Fingering behavior with changing the density difference. Density of the injecting fluid is constant at $\rho_1 = 1.12 \text{ g/cm}^3$ and the fluid injection rate and the plate velocity are fixed at $Q = 3.45 \text{ mL/min}$ and $V = 1 \text{ cm/min}$. Density of the ambient fluid (ρ_2) is varied from 1.382 g/cm^3 to 1.450 g/cm^3 . Exp #48, $\rho_2 = 1.382 \text{ g/cm}^3$. Exp #49, $\rho_2 = 1.394 \text{ g/cm}^3$. Exp #50, $\rho_2 = 1.425 \text{ g/cm}^3$. Exp #51, $\rho_2 = 1.450 \text{ g/cm}^3$.

As described in equation 2 (chapter 2) for the Saffman-Taylor instabilities, density variations are negligible for a horizontal Hele-shaw cell. So fingering behavior is expected occur independently with changing the density difference. The wavelengths for these experiments are shown in Figure 3.25 and Figure 3.26 for downstream and upstream directions respectively.

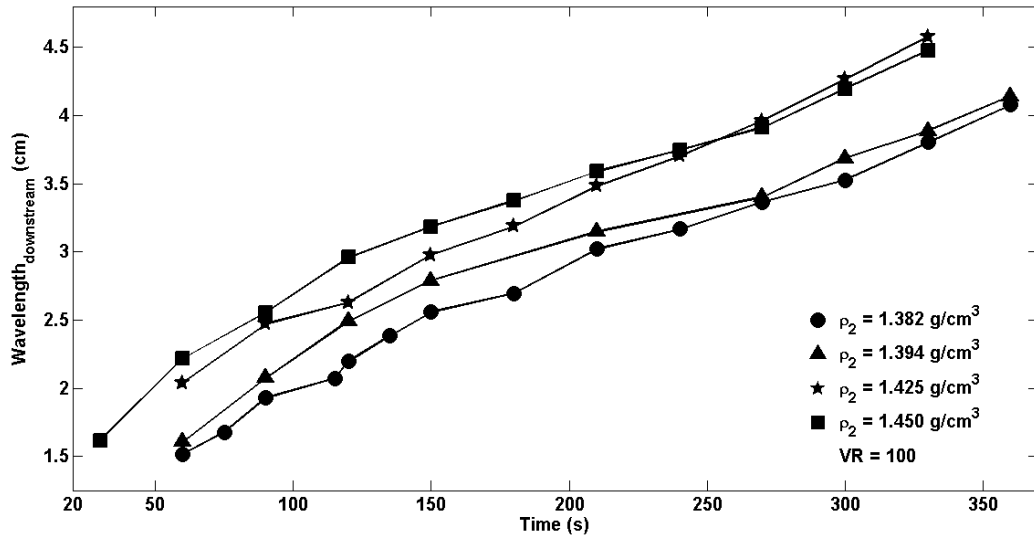


Figure 3.25. Variation of downstream wavelength with time with varying density difference. The viscosity ratio ($VR = 100$), plate velocity ($V = 1$ cm/min) and fluid injection rate ($Q = 3.45$ ml/min) are constant for above experiments. The density of the fluid 1 is constant at 1.12 g/cm³ and the density of the fluid 2 varies from 1.382 g/cm³ to 1.45 g/cm³. Circles- Exp #48, $\rho_2 = 1.382$ g/cm³. Triangles- Exp #49, $\rho_2 = 1.394$ g/cm³. Pentagrams- Exp #50, $\rho_2 = 1.425$ g/cm³. Squares- Exp #51, $\rho_2 = 1.450$ g/cm³.

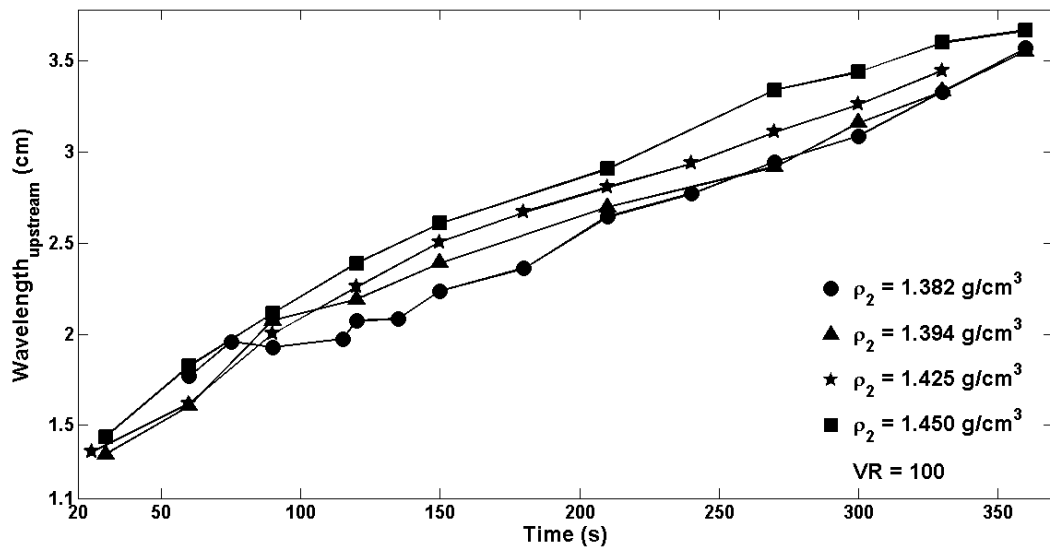


Figure 3.26. Variation of upstream wavelength with time with varying density difference. The viscosity ratio ($VR = 100$), plate velocity ($V = 1$ cm/min) and fluid injection rate ($Q = 3.45$ ml/min) are constant for above experiments. The density of the fluid 1 is constant at 1.12 g/cm³ and the density of the fluid 2 varies from 1.382 g/cm³ to 1.45 g/cm³. Circles- Exp #48, $\rho_2 = 1.382$ g/cm³. Triangles- Exp #49, $\rho_2 = 1.394$ g/cm³. Pentagrams- Exp #50, $\rho_2 = 1.425$ g/cm³. Squares- Exp #51, $\rho_2 = 1.450$ g/cm³.

In both directions wavelength increases with time and shows close behavior to each experiment for different density values. The lowest and the highest wavelengths occur with the lowest and the highest density differences respectively. As all the other physical parameters are held constant, this further confirms that the effect of the density variations is negligible for finger wavelength for a horizontal setup. However, the initiation radius shows a decreasing pattern with increasing density difference (Figure 3.27), though the range of change is very small compared to the other experimental methods.

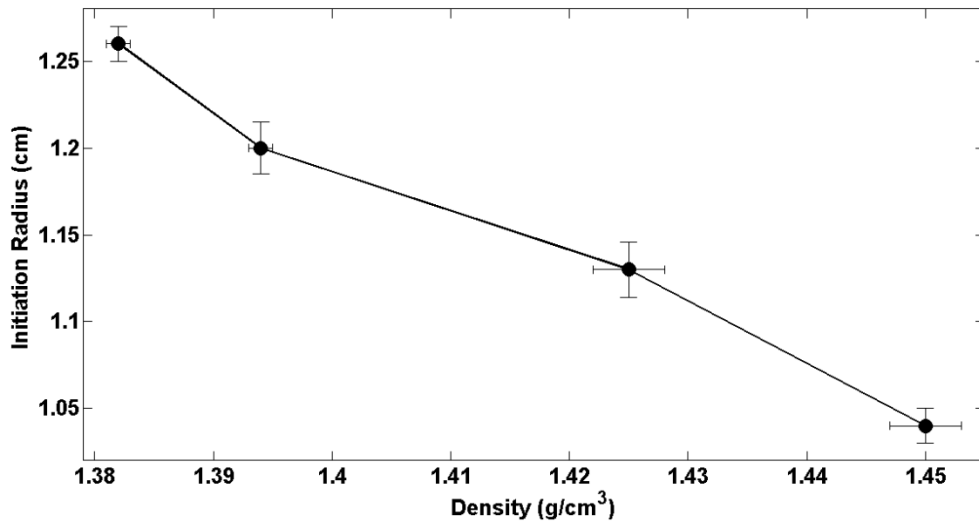


Figure 3.27. Initiation radius as a function of fluid density (fluid 2). The density of the fluid 1 is constant at 1.12 g/cm^3 and the density of the fluid 2 varies from 1.382 g/cm^3 to 1.45 g/cm^3 . Density difference varies from 0.26 g/cm^3 to 0.3 g/cm^3 . The viscosity ratio ($\text{VR} = 100$), plate velocity ($V = 1 \text{ cm/min}$) and fluid injection rate ($Q = 3.45 \text{ ml/min}$) are constant for above experiments. Exp #48, $\rho_2 = 1.382 \text{ g/cm}^3$. Exp #49, $\rho_2 = 1.394 \text{ g/cm}^3$. Exp #50, $\rho_2 = 1.425 \text{ g/cm}^3$. Exp #51, $\rho_2 = 1.450 \text{ g/cm}^3$.

3.2.5. Method 5 – Varying Ultra-Slow Injection Rate (Q_u)

In order to test the Rayleigh-Taylor instabilities with a moving upper boundary, I ran a series of experiments that vary plate velocity and fluid density. I observe these instabilities as linear striations which develop within each finger. These striations form parallel to the fingering direction and show regular spacing within each finger. I observe

striation development for both stationary and moving upper plate experiments. The stationary plate experiment with viscosity ratio 100 (Figure 3.28) shows regular spaced linear striations which are formed in each finger.

This gravitational instability occurs due to the density variations of the injecting and ambient fluid for a horizontal fluid flow. I suggest that the density variations are caused by the presence of a film layer of the high viscosity (ambient) fluid that attach to the top and the bottom of the plate even as low viscosity fingers penetrate to the plate spacing with a moving upper boundary. This film layer is denser due to the high sugar concentration and high viscosity. The dense fluid close to the mobile upper plate is gravitationally unstable and starts to form striations whereas the film layer at the bottom of the plate is stable.

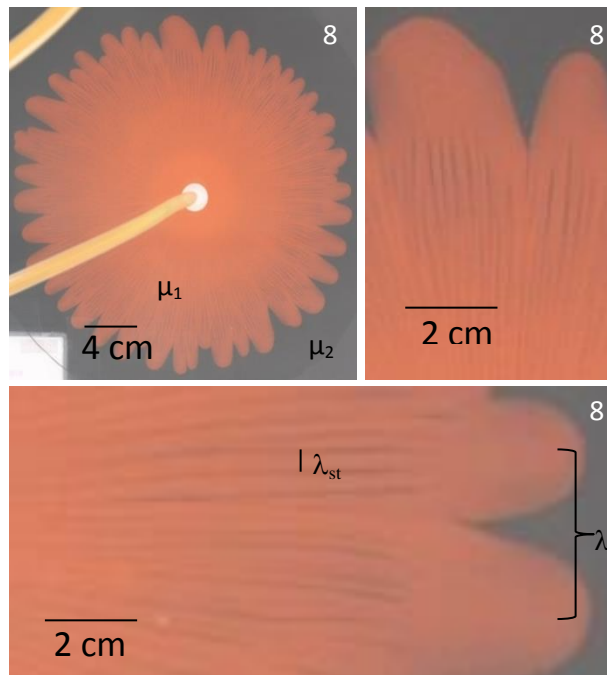


Figure 3.28. Linear striations in viscous fingers for stationary plate setup. Finger wavelength (λ) and wavelength of striations (λ_{st}) are measured as shown in the figure above. Fluid injection rate and the viscosity ratio are constant at 10 ml/min and 100 respectively. Images are taken from the experiment number 8.

Chapter 4 Discussion

4.1 Scaling Laboratory Experiments to the Mantle

In my experiments, I find that the parameters B and Γ have the strongest influence on fingering behavior. The parameter Γ ($\Gamma = Q/VB^2$) is controlled dominantly by V and B . Fluid injection rate (Q) is a minor factor. In many cases, the fluid-fluid interface remains intact and undisturbed, growing as a concentric ring around the initiation point with no fingers. Fingers form later from a point defined by the radius of initiation, R_o (similar to IR as shown in Figure 2.2). I find that R_o depends on several factors including plate spacing (B), viscosity ratio (VR), absolute viscosity, and plate velocity (V). Other parameters such as Q and the density difference ($\Delta\rho$) have a minor effect. Below I discuss the major factors which control fingering and consider scaling to the Earth's upper mantle.

4.1.1 Gamma (Γ)

I use radial fingering experiments with a moving upper boundary to model viscous fingering in the oceanic mantle and plate motion over an asthenosphere. The non-dimensional gamma ratio mentioned in the previous chapters describes the relative rates of fluid injection and plate motion as $\Gamma = (\text{flux} / V_{\text{plate}})$ which is the ratio of mass flux to plate velocity (equation 2). This ratio varies from 0.005 to 12700 in my experiments. To scale laboratory fingering experiments to the oceanic mantle, I use buoyancy and volume flux values for ocean islands (Sleep 1990) to estimate Q in the oceanic upper mantle. Calculated Γ for the Earth's upper mantle varies from 0.0006 to 56. The lowest and the highest Q came from the plume fluxes (Sleep, 1990 and Davies, 1988) of the St. Helena and Kerguelen (0.5 Mgs^{-1}) and the Hawaiian volcanic chains (8.7 Mgs^{-1}), respectively. I

consider asthenospheric thickness to vary from 30 to 100 km and plate velocities from 0.5 to 15 cm/y for the calculations above. The assumed average plume radius ranges from 100 km to 500 km (Sleep, 1990). I am able to represent all but the very lowest Γ values for the Earth in my experiments.

The behavior of the fingers and the fluid interface can be explained according to the phase diagram as shown in Figure 4.1 which relates Q to V . In regime 1, Q is high and V is low and fingers form radially in nearly all directions and the finger formation is similar to the stationary plate case. In regime 2, radial fingering patterns become more elliptical with increasing V . Low viscosity fluid (Fluid 1) fingers travel in both downstream and upstream directions parallel to the plate motion direction while fingers perpendicular to plate motion are damped out. Fluid behavior and the fingering in regime 4 are expected to occur similar to the regime 3 except little bit of upstream fingering due to the slow plate velocity. When Q and V are both slow as depicted in regime 4, fluid 1 is dominantly controlled by plate velocity and travels mostly downstream. Fingers do not occur unless Q increases sufficiently, as shown in experiment# 27. Regime 3 in my experiments corresponds to the Γ values in the Earth's upper mantle (Figure 4.1, dashed box outline). The finger formation of this regime is largely controlled by the higher velocity of the moving upper plate, V , rather than fluid injection rates, Q , which are slow. In regime 3, fluid 1 dominantly flows in the downstream direction forming only one or two fingers in most cases. In the next section (4.2.1), I discuss variations in plate spacing, B , within regime 3.

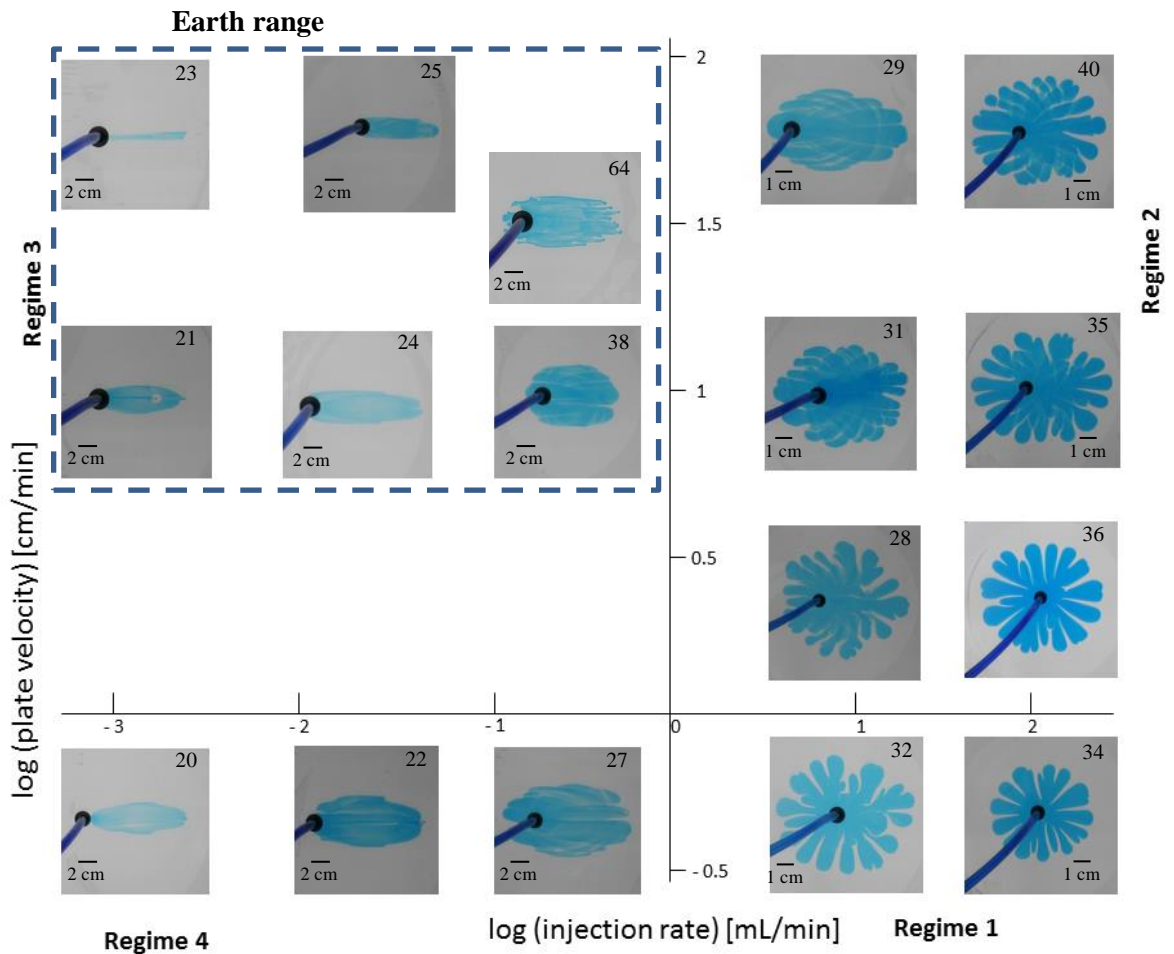


Figure 4.1. Phase diagram showing the fingering experiments with different γ . Four regimes are marked considering finger formation and behavior. Image of each experiment is selected using the same distance away from the injection point. In all experiments, B and VR constant at 1.65 mm and 100 respectively. The dashed box indicates the regime for scaling to the Earth. Experiment #64 has $\gamma = 0.5$, $B = 0.78$ mm, $Q = 0.1$ cm³/min and $V = 40$ cm/min. The number on the upper right corner gives the experiment number of each image.

I scaled the Γ values to the Earth using the plume flux values given in the Sleep (1990). Sleep (1990) determined plume flux from the cross sectional area of the swell and the spreading rate of the plate, assuming an asthenospheric thickness of 100 km. However, magma flux may not be constant within the full radius of the plume axis and also may not be constant at greater distance away from the plume, as material in the asthenosphere supplies the spreading center and may also vary with time. Thus, the calculated Γ for the upper mantle can vary with the plume flux values. More accurate data for the plume fluxes

in the oceanic upper mantle would improve estimates for Γ and evaluation of viscous fingering behavior in the Earth's upper mantle.

4.1.2 Plate Spacing (B)

The experimental results show finger initiation, and the wavelength of the fingers is strongly influenced by plate spacing (B). Both initiation radius and finger wavelength increase with increasing B (Figure 3.22, Figure 3.23).

Plate spacing(B) (mm)	Gamma (Γ)	Downstream/Up stream Fingering
0.07	51.01	Yes*
0.20	6.250	Yes*
0,50	1.100	Yes
0.78	0.500	Yes
1.10	0.180	No
1.65	0.091	No
3.30	0.023	No

Table 4.1 Comparison of moving upper plate fingering experiments in the Earth's gamma range. Several parameters are kept constant for all experiments, fluid injection rate, $Q = 0.1 \text{ cm}^3/\text{min}$ and the plate velocity, $V = 40 \text{ cm}/\text{min}$, $\mu_1 = 2.6 \text{ Pa}\cdot\text{s}$, $\mu_2 = 270 \text{ Pa}\cdot\text{s}$. gamma varies by definition due to changing B. Experiments marked with * show no plate movement during the experiment due to the high pressure from the extremely thin plate spacing, B. The mylar thickness is 0.014 cm for all experiments.

I perform a set of fingering experiments in the Earth's range for Γ (Table 4.1) and consider different plate spacing, B. I find that upstream and downstream fingers form up to a critical plate spacing, $B = 0.78 \text{ mm}$ (Figure 4.2). The photographic image for experiment #64 (Figure 4.1) shows the threshold of B below which fingers are observed. These fingers travel in both downstream as well as upstream directions and may have small wavelengths (see Exp#64 in Figure 4.1). Above this threshold, fluid 1 flows downstream without fingers (or as a single finger). Experiments with $B = 0.07 \text{ mm}$ and B

= 0.2 show formation of radial fingering as the pressure is too high to pull the mylar from the gear assembly.

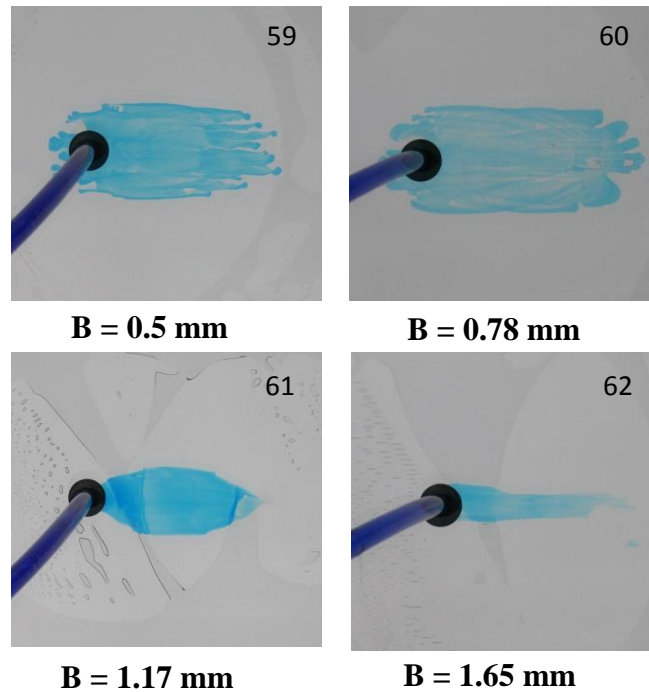


Figure 4.2. Images of moving upper plate fingering experiments in the Earth's gamma range. The fluid injection rate, $Q = 0.1 \text{ cm}^3/\text{min}$ and the plate velocity, $V = 40 \text{ cm}/\text{min}$ are constant. The plate spacing B varies from 0.07 mm to 3.3 mm. Photographs for different B values are selected considering the same distance away from the injection point. $\mu_1 = 2.6 \text{ Pa}\cdot\text{s}$, $\mu_2 = 270 \text{ Pa}\cdot\text{s}$. Exp #59, $B = 0.5 \text{ mm}$. Exp #60, $B = 0.78 \text{ mm}$. Exp #61, $B = 1.17 \text{ mm}$. Exp #62, $B = 1.65 \text{ mm}$.

I consider the asthenospheric thickness where fingering is predicted by our experiments by scaling B to the Earth using the dimensionless ratio, $\Gamma = Q / (VBR_p)$. Here I use R_p as plume radius. I estimate the maximum asthenospheric thicknesses for $\Gamma = 0.5$ by using the maximum possible flux ($Q = 8.7 \text{ Mgs}^{-1}$) in the Hawaiian chains, the minimum plate velocity ($V = 0.5 \text{ cm}/\text{y}$) in the Earth, and minimum $R_p = 100 \text{ km}$ given 387 km for asthenospheric thickness. I obtain the minimum asthenospheric thickness from the minimum flux ($Q = 0.5 \text{ Mgs}^{-1}$) of the St. Helena and Kerguelen volcanic chains, maximum plate velocity of 15 cm/y, and find a maximum $R = 500 \text{ km}$ given 23 km for

asthenospheric thickness. This indicates that viscous fingering is expected to form if the asthenospheric thickness is sufficiently thin < 387 km. Seismic tomography studies of the oceanic upper mantle have imaged the mantle asthenosphere beneath the intraplate seamount chains in the south Pacific (Weeraratne et al., 2007, Lekic and Romanowicz, 2011) showing an average asthenospheric thickness of 80 ± 15 km which falls within the predicted range for fingering suggesting by my study. This suggests that viscous fingering may be a valid model of mantle flow beneath tectonic plates.

4.1.3 Initiation Radius (R_0)

Initiation radius, where fingers first start to form from the fluid-fluid interface strongly depends on the Q (Figure 3.18), V_p (Figure 3.17), VR (Figure 3.4), absolute viscosity, μ_2 (Figure 3.8), B , and density of fluid 2, (Figure 3.27) This is an important and complex measurement as it changes with several parameters. According to my experimental results, the initiation radius would be smaller for high injection rates, viscosity ratios and densities (fluid 2). Fingers initiate at smaller radius for small plate spacing and low absolute viscosities (Figure 4.3). I derive an equation for variation of the initiation radius (R_0) with plate spacing using previous theory for the growth rate of fingers (Chuoke et al., 1959; Homsy, 1987)

$$R_0 = (\Delta\rho/\Delta\mu)(t_c g/12) B^2 \quad (8)$$

where $\Delta\rho$ and $\Delta\mu$ are density and viscosity contrast respectively. B is the plate spacing and t_c is the finger initiation time. I compare experimental initiation radius values with predicted values from equation 8 in figure 4.3. The slopes given by theory are slightly higher than the slope of the data, but fits well for the range of plate spacing shown. I

consider application of the theory to the mantle asthenosphere. I calculate the initiation radius of the Puka Puka linear volcanic chain using the above equation (Eq. 8), taking the asthenosphere thickness ($B = 60$ km), density contrast ($\Delta\rho = 2.2$ gcm⁻³) and viscosity contrasts ($\Delta\mu = 10^{18}$ – 10^{22} Pa.s) in the mantle asthenosphere, giving $R_o \leq 344$ km. This value is an upper bound based on the over prediction of our theory. This is physically reasonable given the Puka Puka ridges extend over 3000 km from their origin near the south Pacific Superswell to the East Pacific Rise spreading center. The distance from the origin of the Superswell to the start of the Puka Puka ridges is less than 400 km.

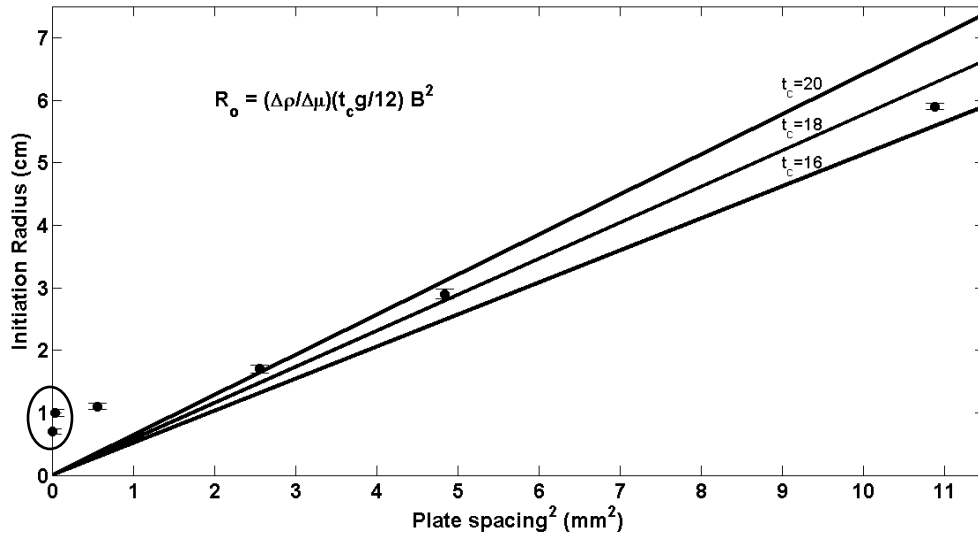


Figure 4.3. The plot of experimental and theoretical variation of the initiation radius with plate spacing. The time it takes to initial finger formation (t_c) is varied from 16 s to 20 s. Theoretical data line with $t_c = 18$ sec best fits the experimental data points. Data points within the black circle on the vertical axis show experiments which R_o is less than the tube attachment and therefore the true R_o cannot be viewed and measured. Exp #42, $B = 0.03$ mm. Exp #43, $B = 0.2$ mm. Exp #44, $B = 0.75$ mm. Exp #45, $B = 1.65$ mm. Exp #46, $B = 2.2$ mm. Exp #47, $B = 3.3$ mm.

4.2 Scaling Experiments to the Earth Using Non-Dimensional Parameters

I used the non-dimensional Reynolds number and Peclet number to determine effects of viscous forces and diffusive mixing for both the laboratory and the Earth's upper mantle systems. Experimental Reynolds numbers range from 1.3×10^{-6} - 4.3×10^{-5} indicating

that experiments are in the laminar flow regime and inertial forces are negligible. The Reynolds number for the upper mantle using the Puka-Puka ridge velocity at 20 cm/yr (Sandwell et al., 1997) is in the range of 2×10^{-19} - 2×10^{-21} . Thus, the flow regime for the oceanic upper mantle is governed by laminar flow and will be in the Stokes flow regime where viscous forces dominate and inertial forces are negligible. Reynolds numbers in my experiments are higher than calculated for the upper mantle; however, $Re \ll 1$ in both systems indicates that viscous forces dominate and inertial forces are unimportant. So, fluid flow in my experiments and Earth's upper mantle are in the laminar flow regime and are comparable.

Viscosity variations for the miscible fluids in my experiments are caused by chemical differences due to concentration gradients. The sharpness of the viscosity contrast across the fluid-fluid interface is dictated by the rate of chemical diffusion for these miscible fluids. The Peclet number due to chemical diffusion in my experiments varies from 40 to 13580, indicating that chemical diffusion is small compared to the radial flow velocities. For the asthenosphere, assuming the plate velocity of the Puka Puka ridge ($V = 20$ cm/y) and diffusivity of a partial melt phase acting along grain boundaries is $D = 10^{-12}$ m²/s (Hofman and Hart, 1978; Kohlstedt and Mackwell 1998), the Peclet number, $Pe = 1 \times 10^7$ to 6.3×10^8 . The Peclet number for laboratory results presented here are consistent with this range from $Pe = 4.0 \times 10^5$ - 1.4×10^8 . The large Peclet numbers for the Earth and experiments indicates that diffusion is expected to be negligible and very slow compared to the time for viscous fingers to form and evolve, thus viscosity contrasts will be maintained and sharp over long times. Thermal diffusion times are much faster and may dissipate thermally before fingers reach the spreading center. Chemical differences

may be prevalent and strong in the Earth due to dehydration gradients between the depleted asthenosphere (Hirth and Kohlstedt, 2003) and volatile rich plume material (Workman et al., 2006) arriving at the upper mantle and emptying into the asthenosphere.

Previous work by Chouke (1959) shows fingers are expected to grow exponentially with time and the growth rate fingers is given by,

$$\sigma = \pi \left(\frac{\mu_2 - \mu_1}{\mu_2 + \mu_1} \right) U \lambda \sim \pi U \lambda , \quad (9)$$

where σ is growth rate and λ is the wavelength of fingering. The boundary condition for the finger growth is $\mu_2 / \mu_1 \gg 1$. In my experiments, I vary this ratio from 2 to 300 and only observe formation of fingers for viscosity ratios greater than three ($VR > 3$). Thus the growth rate of fingering should be independent of the viscosity ratio when it is above 3. Another analysis by Paterson (1985) argues that for a large viscosity ratio, the width of the fingers and the finger wavelength also does not depend on the viscosity ratio. Thus, the results in my experiments can be scaled to the mantle as viscosity ratio is not important for the fingering instabilities as long as $\mu_2 / \mu_1 \gg 1$. Viscosity variations in the asthenosphere may vary due to the thermal gradient (temperature difference), amount of water present in the mineral (olivine and garnet) phases and the amount of melt or other fluids phases present. According to petrological laboratory results by Hirth and Kohlstedt (2003), variation of water content in the upper mantle may change the viscosity variations by a factor of 100 or more.

4.3. Length Scale and Width of Linear Seamounts in the South Pacific Plate

Previous multidisciplinary studies, such as the GLIMPSE and the MELT study in the south Pacific focus on the origin of volcanic ridges and gravity lineations through detailed petrological and geochemical analysis in an area at 17° S near the East Pacific Rise (EPR). Refraction/reflection data from ocean bottom seismometers (OBS), shipboard gravity data, magnetometer data and geochemistry of dredged basalts provides a more detailed constrain of low seismic velocity anomalies beneath spreading axis (Forsyth et al., 1998; Conder et al., 2002; Evans et al., 2005). The MELT experiment shows both along axis and the across axis asymmetry of the EPR. They observed strong low velocity anomalies and seismic anisotropy for the Pacific plate compared to the Nazca plate side of the EPR.

Rayleigh wave tomography beneath intraplate volcanic ridges in the south Pacific (Weeraratne et al., 2007) shows a negative seismic velocity gradient observed at 40 ± 15 km which defines the base of the lithosphere (and top of the asthenosphere). At 70 km depth the low velocity gradient changes to a sharp positive gradient that extends down to 120 km depth. They define the asthenosphere at these boundaries at 40 - 120 km depth. Anomalously low shear wave velocities appear to be located beneath the Sojourn Ridge, Puka Puka and Hotu Matua volcanic chains with higher velocities in-between them (Weeraratne et al., 2007; Harmon et al., 2009).

Volcanic samples collected from these intraplate seamounts shows geochemical enrichment far from the spreading center and increasing concentration away from the ridge axis. Geochemical analysis of Puka Puka (Mahoney et al., 1994), Sojourn and Hotu

Matua (Donnelly et al., 2003) ridges in the south Pacific indicate enrichment concentration decreases progressively from west to east. Isotopes He, Sr, Pb and Nd along the EPR axis from north to south show a peak in geochemical enrichment where the Hotu Matua seamount meets the EPR (Mahoney et al., 1994) 17°S latitude. In this model we suggest that this geochemical anomaly may be a viscous finger of enriched mantle material which transports material from western Pacific to the EPR spreading center. The width of the geochemical anomaly may reflect the width of the asthenospheric finger which is travelling from off axis to the EPR.

A study by Forsyth et al., (2006) suggests that active melt production in the asthenosphere could explain the linear orientation, width of the seamounts and the volume of melts. If pressure release melting is aligned with absolute plate motion and travels along the gradient at the base of the cooling and thickening lithosphere, the viscous fingering model may transport material as linear fingers caused by the Saffman Taylor instabilities in both downstream and upstream directions. They further suggest that the Puka Puka ridge, Sojourn and Brown ridges appear to develop with densely scattered seamounts, later they build up into distinct ridges with regular spacing. This is observed in method 5 (Figure 3.29), where linear striations are formed by Rayleigh Taylor instabilities beneath the moving upper plate.

The viscous fingering model, scaled to the Earth's upper mantle, suggests transport of enriched mantle material from off axis enriched sources horizontally through the asthenospheric channel to the spreading center. This model may explain the organized pattern of intraplate volcanic chains. The mechanism of melt transportation from off-axis to the spreading center has been suggested as pressure gradients from deformation of the

viscous mantle matrix (Spiegelman and Mckenzie, 1987) and this model uses the same mechanism to form viscous fingers laterally through the plate spacing. This model may link the Earth's large scale mantle convection system to small scale flow in the upper mantle as well as contribute to plate formation at spreading centers

Chapter 5 Conclusion

I conducted a series of laboratory experiments on viscous fingering using glucose-water solutions. I varied viscosity ratio, absolute viscosity, gamma ratio, plate spacing and fluid density (see Table 2.2). I used both stationary and moving upper plate setup to compare the fingering instabilities for parameters prescribed. The experimental Reynolds number scaled to the Earth is higher than the calculated value for the upper mantle, but is less than 1 indicating viscous forces are dominant and the flow regime is laminar. Large Peclet numbers for both lab and Earth indicate that diffusion is expected to be negligible.

Wavelength and initiation radius of fingering instabilities with stationary plates depends on both the viscosity ratio and absolute viscosities. I observed Rayleigh-Taylor instabilities (linear striations) for the stationary plate setup with ultra-slow fluid injection rates. In moving upper plate experiments, finger wavelength and the initiation radius of are strongly influenced by the gamma, plate spacing, fluid injection rate and plate velocity. My laboratory results indicate that fingers align with plate motion both upstream and downstream and indicate longer wavelengths in the downstream direction. Experiments scaled to the Earth's upper mantle show fingers form in the presence of surface plate motion for $\Gamma = 0.5$ if asthenospheric thickness is less than 386 km. Scaling to

study the south Pacific seafloor shows fingers should develop for $R_o \leq 350$ km from the plume source. Results show that viscous fingering in the Earth's upper mantle is a plausible mechanism which can be used to explain the organized pattern of intraplate volcanic chains. The viscous fingering model suggests transports of enriched mantle material horizontally through the asthenospheric channel to the spreading center from off-axis enriched sources. This new geodynamic model for viscous fingering in the asthenosphere links off-axis and rising mantle plumes indirectly to mantle return flow to the spreading centers where they contribute to melting, surface volcanism and the growth and formation of new lithosphere.

Chapter 6 Future Work

In this chapter, I list future work that will advance this research, help quantify my results, and increase laboratory method efficiency.

1) Increase density variations steadily for each experiment to analyze the Rayleigh-Taylor instability with an upper moving boundary in order to ascertain how density difference is affected to the formation of linear striations.

2) Use lower injection rates from the fluid pump to observe viscous fingers within the calculated gamma range in the Earth.

3) Perform experiments with lower plate velocities using a modified gear-motor assembly to identify the length scale and time scale of striations within a viscous finger.

These are Rayleigh-Taylor striation instabilities which form within Saffman-Taylor viscous fingering instabilities and only for experimental durations that last a longer period of time, upto 10 hours or more. I observed some of these forming in a few cases mentioned above. But a full set of new experiments which use ultra-slow plate velocities need to be done to study this phenomenon of striations and to also determine whether they form for gamma values within the range of the Earth.

4) Measure finger width of the experiments for all five methods for moving upper boundary experiments to scale the Length/Width (L/B) ratio of viscous fingers to the Earth's upper mantle.

5) Measure how much fluid high viscosity fluid is around the viscous fingers in upstream and downstream directions for both stationary and mobile plate experiments.

6) Use a modified Particle Image Velocimetry (PIV) method to analyze the fluid behavior within each fluid and fluid-fluid interface (Figure 6.1). This will further explain the theory of streamlines and the return flow opposite to the plate motion.

7) Vary thickness of the injection hole to see if a wide hole reduces the two-layer flow and a thin hole increases the two-layer flow.

8) Do experiments where, the relationship between shear stress and strain rate $n \neq 1$. This applies for dislocation creep regime in the upper mantle.

9) Use CMC fluids with small B to study fingers like gamma range for the Earth. Do future experiments with $B \leq 0.78$ mm and a set of experiments without mylar which seems to produced fingers easily.

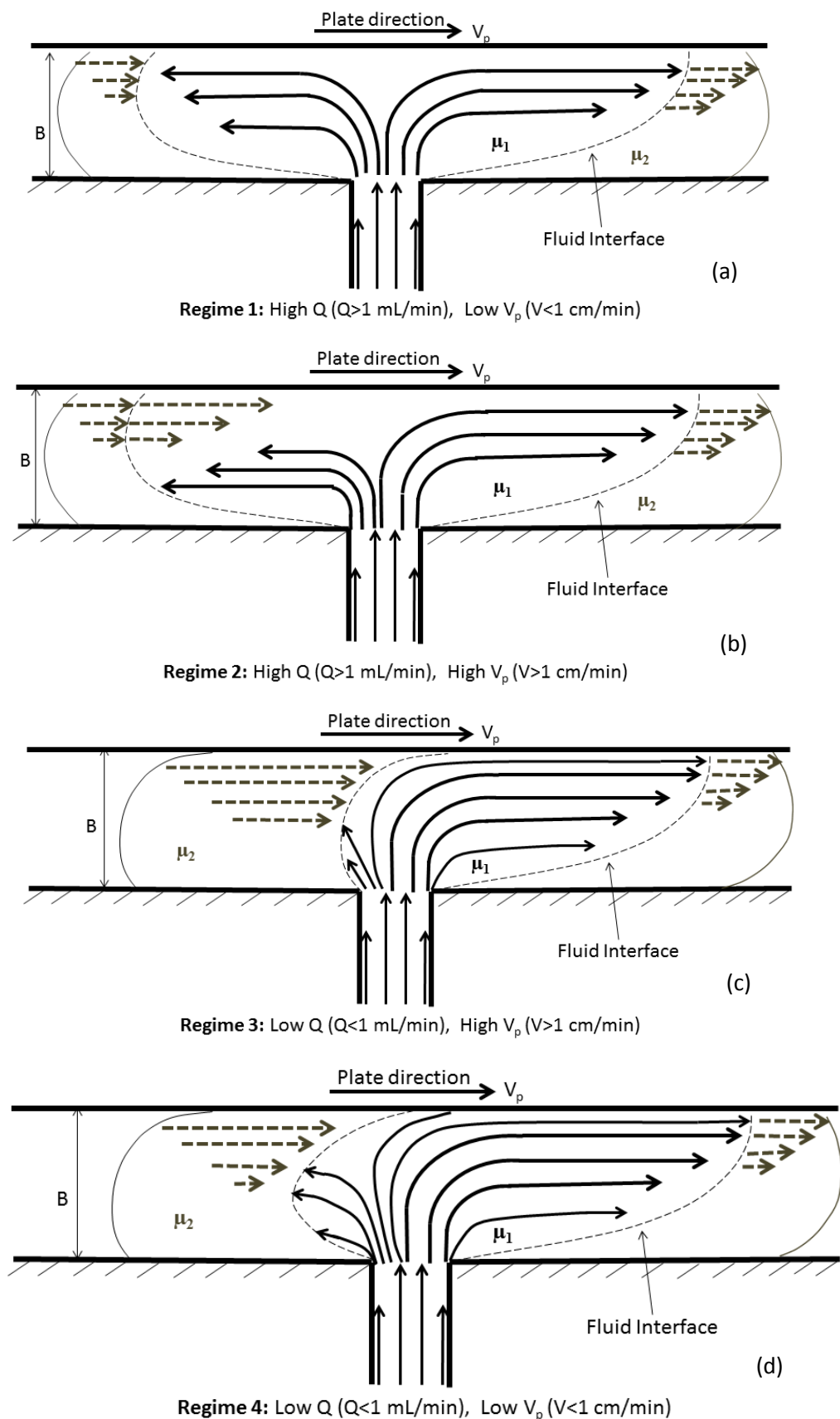
10) I used two methods to make CMC fluids for the experiments.

Step 1: Add boiling water to the CMC fluid or CMC fluid to the boiling water.

Step 2: Mix well until the CMC powder dissolve completely and use a strainer to get the liquid part to a beaker.

Step 3: Put the water + CMC solution in the hot frog box for about 2 days.

Step 4: Take the fluid out and measure the density and viscosity of fluid using the standard measuring method.



Regime 1: High Q ($Q > 1$ mL/min), Low V_p ($V < 1$ cm/min)

Regime 2: High Q ($Q > 1$ mL/min), High V_p ($V > 1$ cm/min)

Regime 3: Low Q ($Q < 1$ mL/min), High V_p ($V > 1$ cm/min)

Regime 4: Low Q ($Q < 1$ mL/min), Low V_p ($V < 1$ cm/min)

Figure 6.1. Behavior of fluid streamlines in each regimes for experiments with varying gamma. (a) Regime 1, (b) Regime 2, (c) Regime 3, (d) Regime 4. Black solid arrows show movement of low viscosity fluid over plate spacing B. Black dash arrows show velocity gradients for downstream and upstream directions.

References

- Ballmer, M.D., G. Ito, J. van Hunen, P. J. Tackley, 2010. Small-scale sublithospheric convection reconciles geochemistry and geochronology of 'Superplume' volcanism in the western and south Pacific, *Earth and Planet. Sci. Lett.*, 290, 224-232.
- Ballmer, M.D., C.P. Conrad, E.I. Smith, N. Harmon, 2013. Non-hotspot volcano chains produced by migration of shear-driven upwelling toward the East Pacific Rise, *Geology*, 41, 479-482.
- Buck, W. R., and E. M. Parmentier, 1986. Convection beneath young oceanic lithosphere: implications for thermal structure and gravity, *J. Geophys. Res.*, 91, 1961-1974.33
- Chouke, R.L. 1959. Stability analysis for secondary miscible displacement with an initially sharp solvent-oil interface, appendix in Gardner, J.W., and J.G.J. Ypma, 1982, An investigation of phase behavior-macroscopic bypassing interaction in CO₂ flooding, SPE 10686 Soc. Pet. Eng., Dallas, Texas.
- Conder, J.A., D.W. Forsyth, and E.M. Parmentier, 2002. Asthenospheric flow and asymmetry of the East Pacific Rise, MELT Area, *J. Geophys. Res.*, 107, B12, 2344, doi: 10.1029/2001JB000807.
- Conrad, C.P., T.A. Bianco, E.I. Smith, P. Wessel, 2011. Patterns of intraplate volcanism controlled by asthenospheric shear, *Nature Geoscience*, 4, doi: 10.1038/NGE01111.
- Davies, G. F., Ocean bathymetry and mantle convection, 1, Large-scale flow and hotspots, *J. Geophys. Res.*, 93, 10,467-10,480, 1988a
- Donnelly, K.E., C. H. Langmuir, S. L. Goldstein, 2003. Geochemical constraints on melting process in the GLIMPSE region, EOS Trans. AGU, Abstract, Fall.
- Evans, R.L., G. Hirth, K. Baba, D. Forsyth, A. Chave, and R. Mackie, 2005. Geophysical evidence from the MELT area for compositional controls on oceanic plates, *Nature*, 437, 249-252.
- Forsyth, D. W., S. C. Webb, L. M. Dorman, Y. Shen, 1998. Phase velocities of Rayleigh waves in the MELT experiment on the East Pacific Rise, *Science*, 280, 1235-1237.
- Forsyth, D. W., N. Harmon, D. S. Scheirer, and R.A. Duncan, 2006. Distribution of recent volcanism and the morphology of seamounts and ridges in the GLIMPSE study area: Implications for the lithospheric cracking hypothesis for the origin of intraplate, nonhot

- spot volcanic chains, *J. Geophys. Res.*, 111, B11406, doi: 10.1029/2005JB004071.
- Harmon, N. D. W. Forsyth, D.S. Scheirer, 2006. Analysis of gravity and topography in the GLIMPSE study region; isostatic compensation and uplift of the Sojourn and Hotu Matua Ridge systems, *J. Geophys. Res.*, 111.
- Harmon, N., D. W. Forsyth, D. S. Weeraratne, Y. Yang, S. C. Webb, S C., 2011. Mantle Heterogeneity and off axis volcanism on young Pacific seafloor. *Earth Planet. Sci. Lett.*, 311, 306-315, doi:10.1016/j.epsl.2011.09.038.
- Haxby, W.F., J. K. Weissel, 1986. Evidence for small-scale mantle convection from Seasat altimeter data, *J. Geophys. Res.*, 91, 3507-3520.
- Hill, S., 1952. Channelling in packed columns, *Chem. Eng. Sci.*, 1, 247-53.
- Hirth, G., D. L. Kohlstedt, 2003. Rheology of the mantle wedge, in Eiler, J., ed., *Inside the Subduction Factory: American Geophysical Union Geophysical Monograph 138*, 83105.
- Homsy, G.M. 1987. Viscous fingering in porous media, *Ann.Rev. Fluid Mech.*, 19, 271-311.
- Janney, P. E., J. D. Macdougall, J. H. Natland, M. A. Lynch, 2000. Geochemical evidence from the Pukapuka volcanic ridge system for a shallow enriched mantle domain beneath the south Pacific superswell, *Earth Planet. Sci. Lett.*, 181, 47-60.
- Lekic, V., B. Romanowicz, 2011a. Inferring upper-mantle structure by full waveform tomography with the spectral element method, *Geophys. J. International*, 185, 799-831.
- Lekic, V. and B. Romanowicz, 2011b. Tectonic regionalization without a priori information: a cluster analysis of tomography, *Earth Planet Sci. Lett.*, 308, 151-160.
- Lynch, M.A., 1999. Linear ridge groups: Evidence for tensional cracking in the Pacific Plate, *J. of Geophys. Res.*, 104, 29321-29333.
- Mahoney, J.J., J. M. Sinton, M. D. Kurz, J. D. Macdougall, K. J. Spencer, G.W. Lugmair, 1994. Isotope and trace element characteristics of a super-fast spreading ridge: East Pacific Rise, 13-23S, *Earth Planet. Sci. Lett.*, 121, 173-193.
- McNutt, M.K., 1998. Superswells, *Rev. Geophys*, 36, 211-851 244.
- Melt Seismic Team, 1998. Imaging 852 the deep seismic structure beneath a mid-ocean ridge: The MELT Experiment, *Science*, 280, 1215-1218.
- Montagner, J.P., 2002. Upper mantle low anisotropy channels below the Pacific Plate, *Earth and Planet. Sci Lett.*, 202, 263-274.
- Montelli, R., G. Nolet, F. A. Dahlen, G. Masters, E.R. Engdahl, S. Hung, 2004. Finite frequency tomography reveals a variety of plumes in the mantle, *Science*, 303, 338-343.
- Morgan, W. J., 1972. Plate motions and deep mantle convection, *Mem. Geol. Soc. Am.*, 132, 7-22.

- Morgan, W. J. , 1978. Rodriguez, Darwin, Amsterdam, second type of hotspot island, *J. Geophys. Res.*, 83, Issue B11, pp.5355-5360.
- Nishimura, C. E., D.W. Forsyth, 1988. Rayleigh wave phase velocities in the Pacific with implications for azimuthal anisotropy and lateral heterogeneities, *Geophys. J.*, 94, 479-501.
- Obrebski, M., R. M. Allen, F. Pollitz, S. Hung, 2011. Lithosphere-asthenosphere interaction beneath the western United States from the joint inversion of body-waves travel times and surface waves phase velocities, *Geophys. J. Int.*, 185, 1003-1021.
- Paterson, L., 1985. Fingering with miscible fluids in a Hele Shaw cell. *Phys. Fluids*, 28, 26-30.
- Richter, F.M., and B. Parsons, 1975. On the interaction of two scales of convection in the mantle, *J. Geophys. Res.*, 80, 2529-2541.
- Sandwell, D. T., E. L. Winterer, J. Mammerrickx, R. A. Duncan, M. A. Lynch, D. A. Levitt, C. L. Johnson, 1995. Evidence for diffuse extension of the Pacific plate from Pukapuka ridges and cross-grain gravity lineations, *J. Geophys. Res.*, 100, 15087-15099.
- Sandwell, D.T. & Fialko, Y., 2004. Warping and Cracking of the Pacific Plate by Thermal contraction, *J. Geophys. Res.*, 109, B10411, doi:10.1029/2004JB0030912004.
- Saffman, P. G., G. T. Taylor, 1958. The penetration of a fluid into a porous medium or Hele Shaw cell containing a more viscous liquid, *Proc. R. Soc. London Ser. A*, 245, 312-29.
- Scheirer, D.S., K.C. Macdonald, D.W. Forsyth, and Y. Shen, 1995. Abundant seamounts of the Rano Rahi seamount field near the southern East Pacific Rise, 15 S to 19 S, 897 *Marine Geophys. Res.*, 18, 13-52, doi:10.1007/BF00286202.
- Sleep, N.H., 1990. Hotspots and mantle plumes, some phenomenology, *J. Geophys. Res.*, 95, 6715-6736.
- Smith, W. H. F., and D. T. Sandwell, 1997. Global seafloor topography from satellite altimetry and ship depth soundings, *Science*, 277, 1957-1962, 26.
- Snyder, D., and S. Tait, 1995. Replenishment of magma chambers: comparison of fluid-mechanic experiments with field relations, *Contrib. Mineral Petrol.*, 122, 230-240.
- Weeraratne, D. S., D. 920 W. Forsyth, Y. Yang, and S. C. Webb, 2007. Rayleigh wave tomography beneath intraplate volcanic ridges in the South Pacific, *J. Geophys. Res.*, 112, B06303, doi:10.1029/2006JB004403.
- Whitehead, J.A., and D.S. Luther, 1975. Dynamics of laboratory diapir and plume models, *J. Geophys. Res.*, 80, 705-717.
- Whitehead, J. A., and K. R. Helfrich, 1991. Instability of Flow with Temperature-Dependent Viscosity: A Model of Magma Dynamics, *J. Geophys. Res.*, 96, 4145-415.
- Winterer, E.L., and D. T. Sandwell, 1987. Evidence from en-echelon cross-grain ridges for

tensional cracks in the Pacific plate, *Nature*, 329, 6139, 534-537.

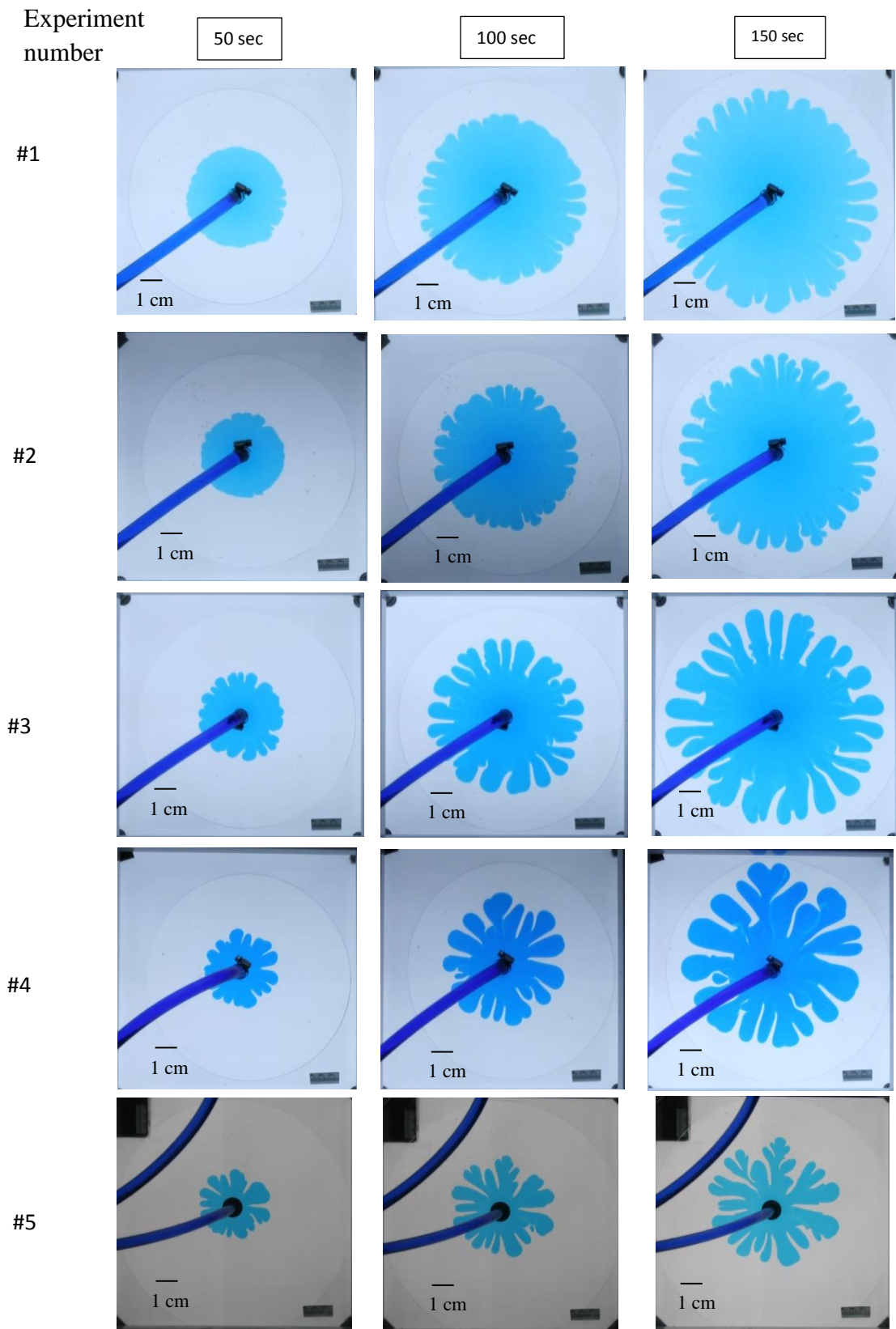
Yang, Y, D.W.Forsyth, D. S. Weeraratne, 2007. Seismic attenuation near the East Pacific Rise and the origin of the low-velocity zone, *Earth Planet. Sci. Lett.*, doi:10.1016/j.epsl.2007.03.040.

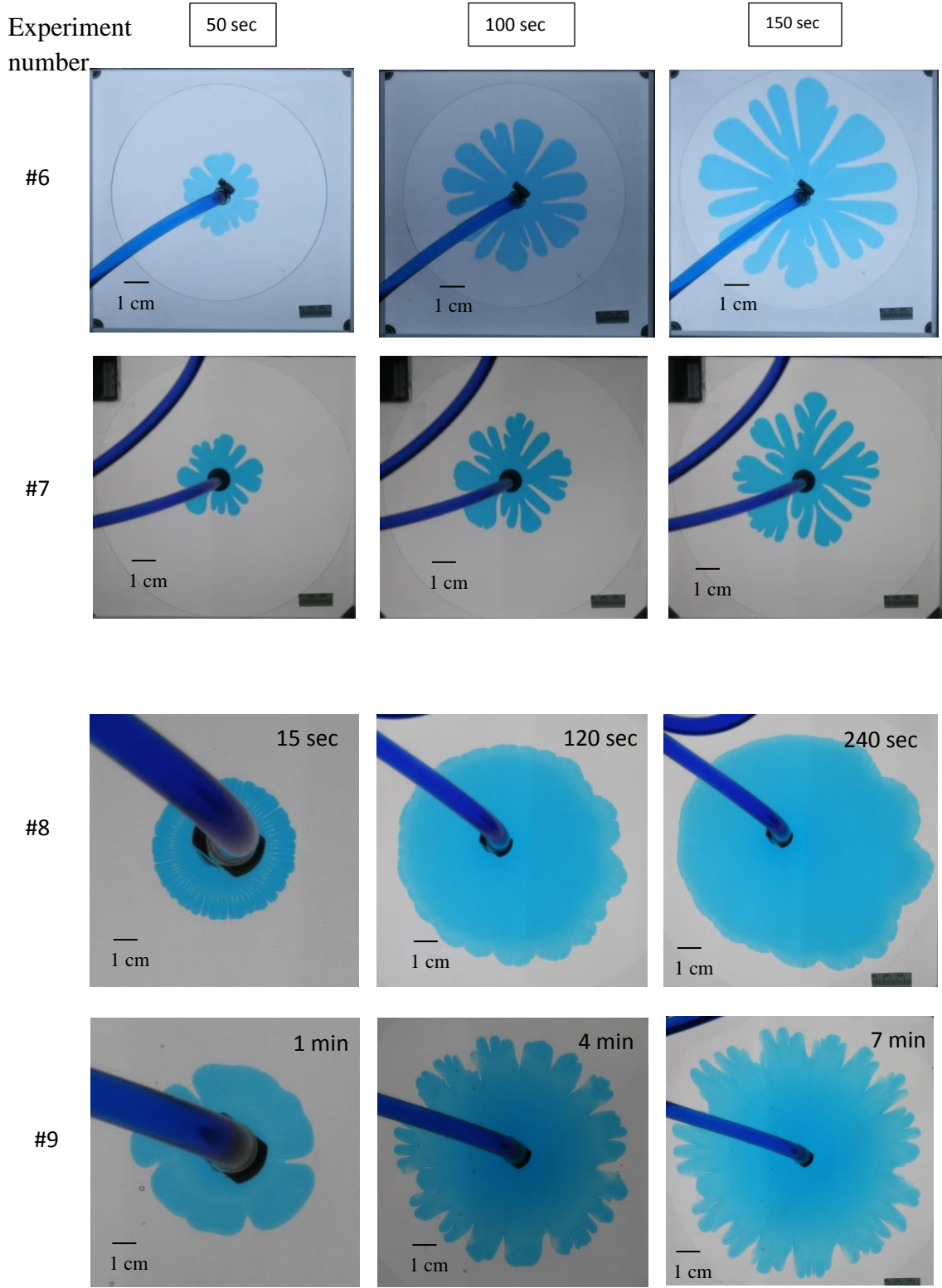
Appendix A

Exp #	VR	μ_1 Pa.s	μ_2 Pa.s	ρ_1 g/cm ³	ρ_2 g/cm ³	B mm	Q ml/min	Vp cm/min	Vf cm/min	Gamma
1	3	86.9	267	1.381	1.423	1.65	9.5	—	3.68	—
2	10	26.4	267.4	1.376	1.425	1.65	10.3	—	3.69	—
3	20	13	267	1.374	1.423	1.65	9.5	—	4.16	—
4	50	5.2	267.5	1.362	1.425	1.65	9	—	2.91	—
5	100	2.7	264.4	1.362	1.425	1.65	10	—	1.76	—
6	200	1.7	326.4	1.346	1.431	1.65	9.5	—	1.57	—
7	300	0.91	276.4	1.341	1.425	1.65	10	—	1.49	—
8	50	0.006	0.3	1.068	1.286	1.65	3.45	—	1.24	—
9	50	0.06	3	1.241	1.368	1.65	3.45	—	0.93	—
10	50	0.6	26	1.315	1.376	1.65	3.45	—	0.97	—
11	50	3.5	175	1.358	1.402	1.65	3.45	—	0.81	—
12	50	5.1	267	1.362	1.425	1.65	3.45	—	1.8	—
13	3	112	265	1.388	1.421	1.65	10	—	1.13	—
14	10	26.7	265	1.378	1.421	1.65	10	—	1.33	—
15	20	13.2	265	1.372	1.421	1.65	10	—	0.96	—
16	50	5.1	265	1.362	1.421	1.65	10	—	1.57	—
17	100	2.5	265	1.36	1.421	1.65	10	—	0.94	—
18	200	1.2	265	1.331	1.421	1.65	10	—	1.42	—
19	400	0.64	265	1.321	1.421	1.65	10	—	1.34	—
20	100	2.7	267.4	1.362	1.425	1.65	0.001	0.29	0.63	0.120
21	100	2.62	267	1.36	1.425	1.65	0.01	0.29	0.83	1.260
22	100	2.64	264.5	1.36	1.423	1.65	0.01	1	1.55	0.367
23	100	2.62	267	1.36	1.425	1.65	0.01	10	1.17	0.037
24	100	2.7	267	1.362	1.425	1.65	0.01	80	12.61	0.005
25	100	2.64	267	1.36	1.425	1.65	0.1	10	3.55	0.367
26	100	2.64	267.4	1.362	1.425	1.65	1	0.29	5.11	126.700
27	100	2.7	267.4	1.362	1.425	1.65	1	10	1.81	3.670
28	100	2.7	267	1.36	1.425	1.65	10	1	5.31	367.300
29	100	2.64	267.4	1.362	1.425	1.65	10	80	13.6	4.600
30	100	2.64	267.4	1.362	1.425	1.65	20	1	9.65	735.000

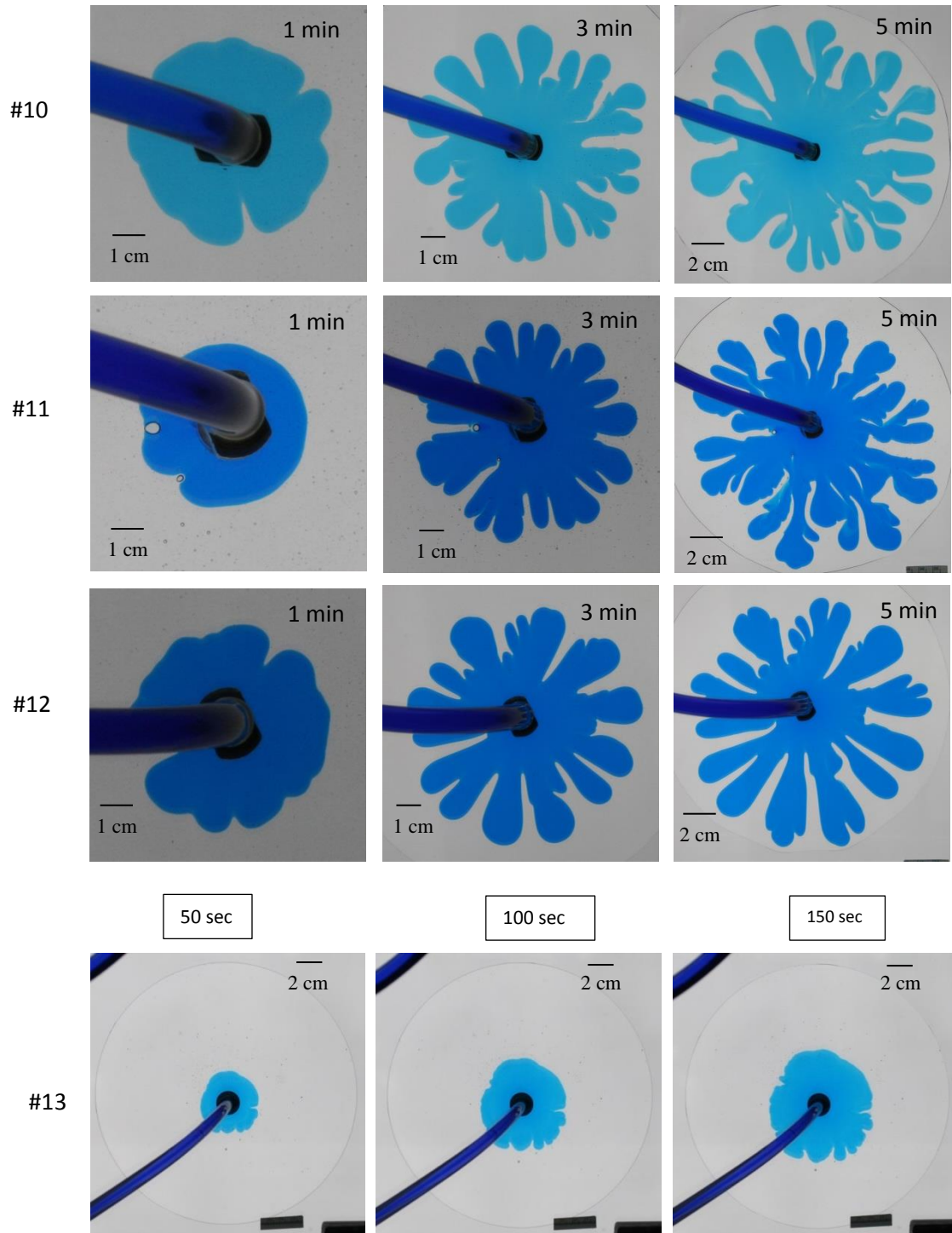
31	100	2.64	267.4	1.362	1.425	1.65	20	10	12.5	73.500
32	100	2.7	267	1.36	1.425	1.65	20	0.29	8.65	2533.200
33	100	2.64	267.4	1.362	1.425	1.65	80	0.29	23.3	10100.100
34	100	2.64	267.4	1.362	1.425	1.65	100	0.29	21.85	12700.800
35	100	2.7	267	1.36	1.425	1.65	100	1	29.63	3670.100
36	100	2.64	267.4	1.362	1.425	1.65	100	10	20.61	367.300
37	100	2.7	267.4	1.362	1.425	1.65	100	80	29.7	45.900
38	100	2.7	267	1.36	1.425	1.65	1	0.29	5.11	127.000
39	100	2.64	267	1.36	1.425	1.65	3.45	1	2.51	127.000
40	100	2.7	267.4	1.362	1.425	1.65	17.1	5	9.2	127.000
41	100	2.64	267.4	1.362	1.425	1.65	34.5	10	13.23	127.000
42	100	2.6	270	1.36	1.425	0.03	3.45	1	4.82	127.000
43	100	2.6	270	1.36	1.425	0.2	3.45	1	4.92	127.000
44	100	2.6	270	1.36	1.425	0.75	3.45	1	2.24	127.000
45	100	2.6	270	1.36	1.425	1.65	3.45	1	2.51	127.000
46	100	2.6	270	1.36	1.425	2.2	3.45	1	1.86	127.000
47	100	2.6	270	1.36	1.425	3.3	3.45	1	1.94	127.000
48	100	0.2	20	1.12	1.382	1.65	3.45	1	1.662	127.000
49	100	0.2	20	1.12	1.394	1.65	3.45	1	1.265	127.000
50	100	0.2	20	1.12	1.425	1.65	3.45	1	1.35	127.000
51	100	0.2	20	1.12	1.45	1.65	3.45	1	1.66	127.000
52	100	0.026	2.6	1.125	1.36	1.65	0.001	0.29	0.63	0.120
53	100	0.026	2.6	1.125	1.36	1.65	0.01	0.29	0.83	1.260
54	100	0.026	2.6	1.125	1.36	1.65	0.1	0.29	1.35	12.600
55	100	0.026	2.6	1.125	1.384	1.65	0.7	0.29	2.66	88.600
56	100	0.026	2.6	1.125	1.384	0.75	0.5	0.29	2.15	153.250
57	100	2.6	270	1.36	1.425	0.07	0.1	40	5.11	127.000
58	100	2.6	270	1.36	1.425	0.2	0.1	40	5.11	15.830
59	100	2.6	270	1.36	1.425	0.5	0.1	40	0.8	30.650
60	100	2.6	270	1.36	1.425	0.78	0.1	40	2.11	306.500
61	100	2.6	270	1.36	1.425	1.17	0.1	40	2.15	153.250
62	100	2.6	270	1.36	1.425	1.65	0.1	40	2.11	306.500
63	100	2.6	270	1.36	1.425	3.3	0.1	40	2.15	153.250

Appendix B

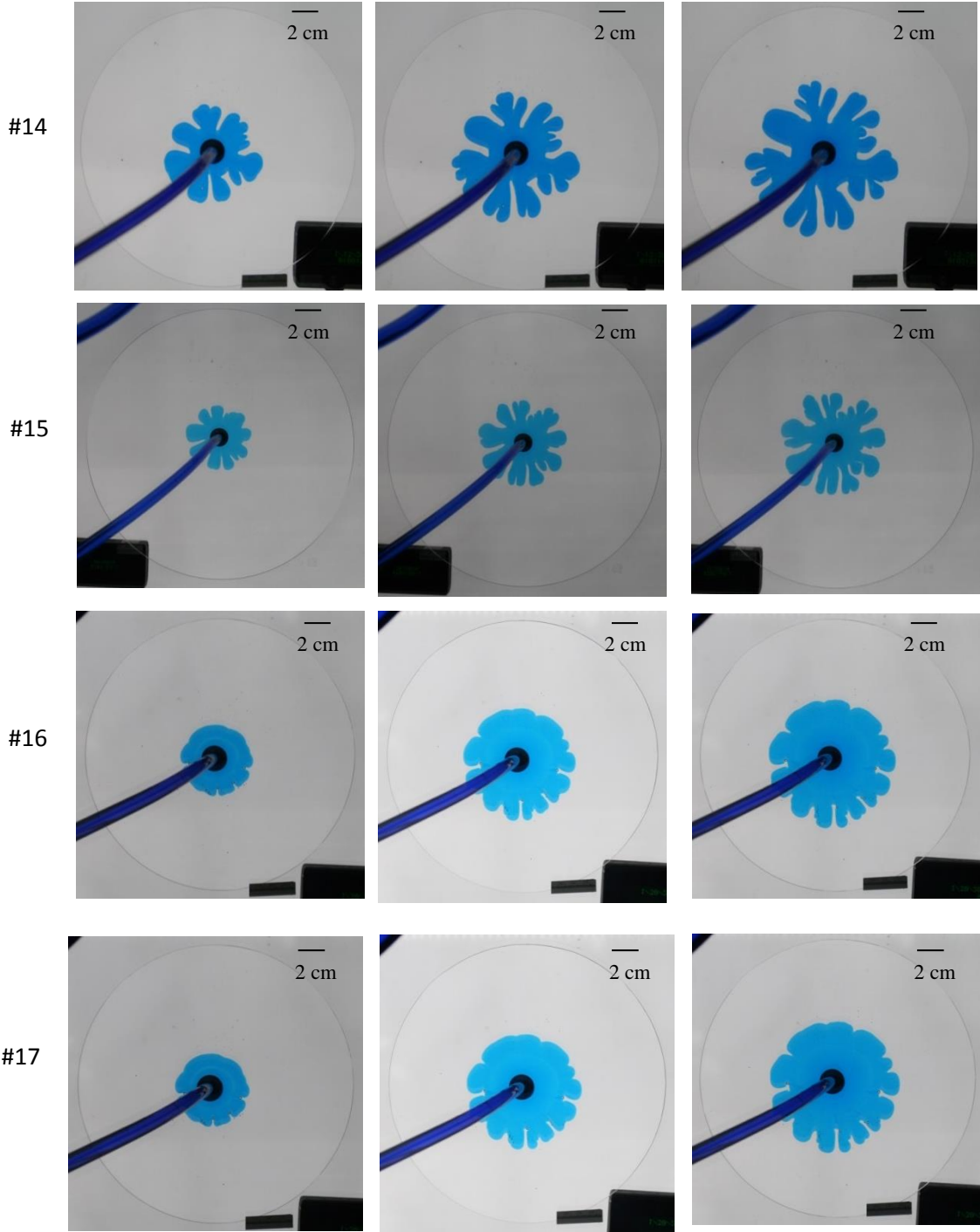


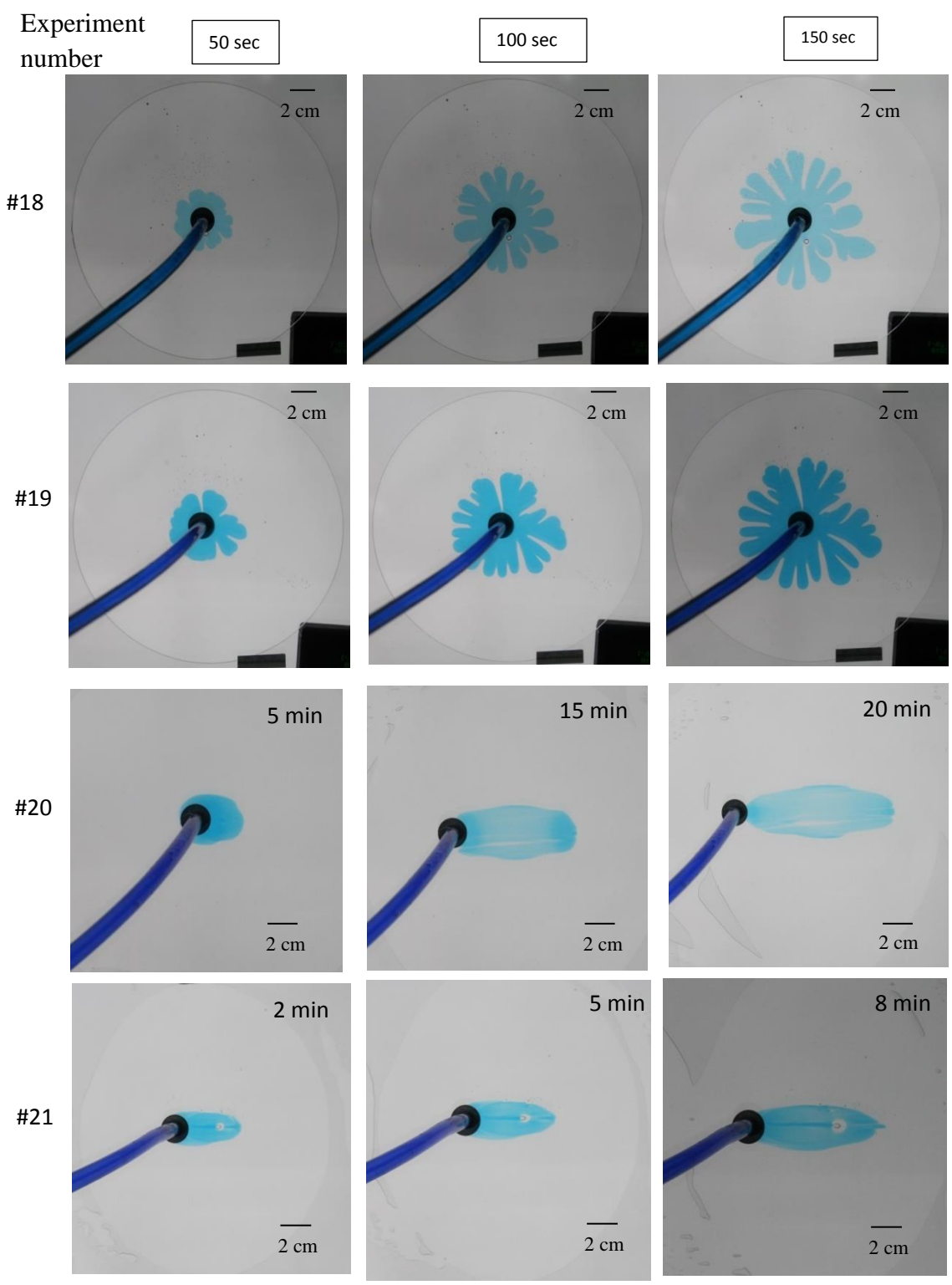


Experiment
number



Experiment
number





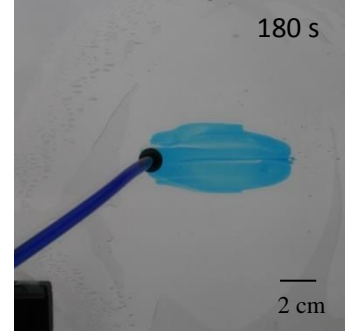
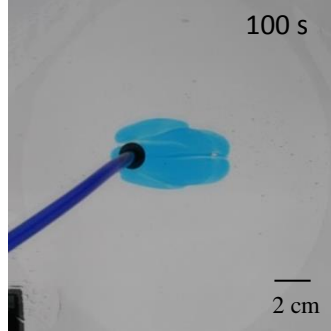
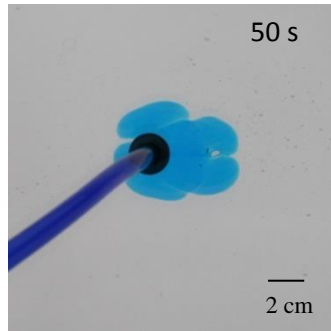
Experiment
number

50 sec

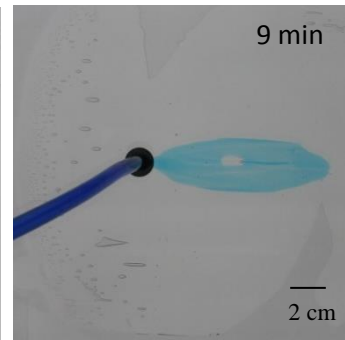
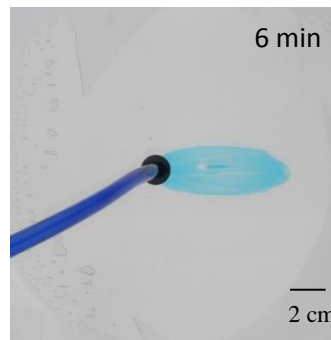
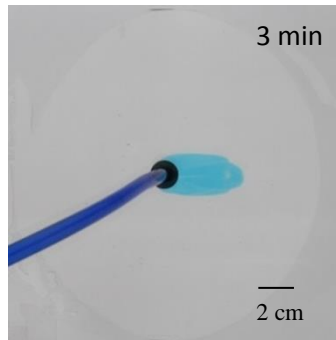
100 sec

150 sec

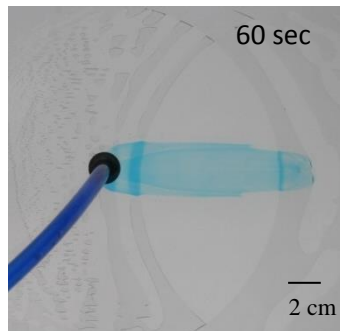
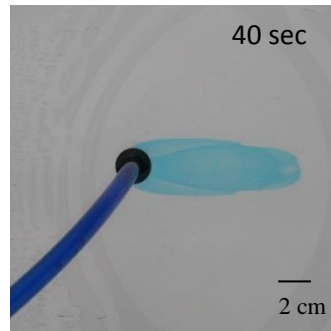
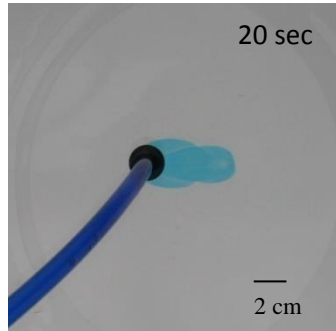
#22



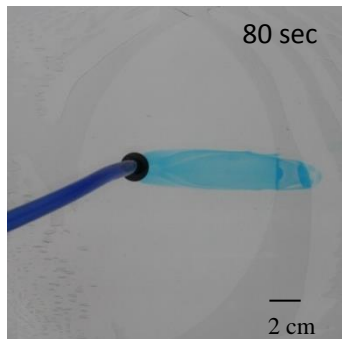
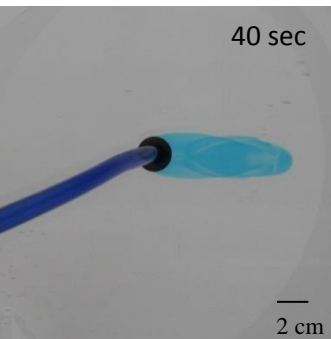
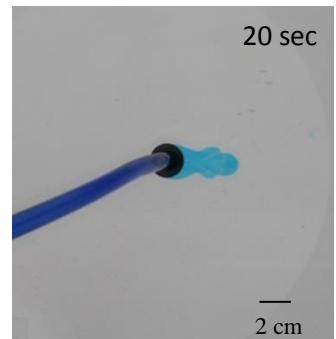
#23

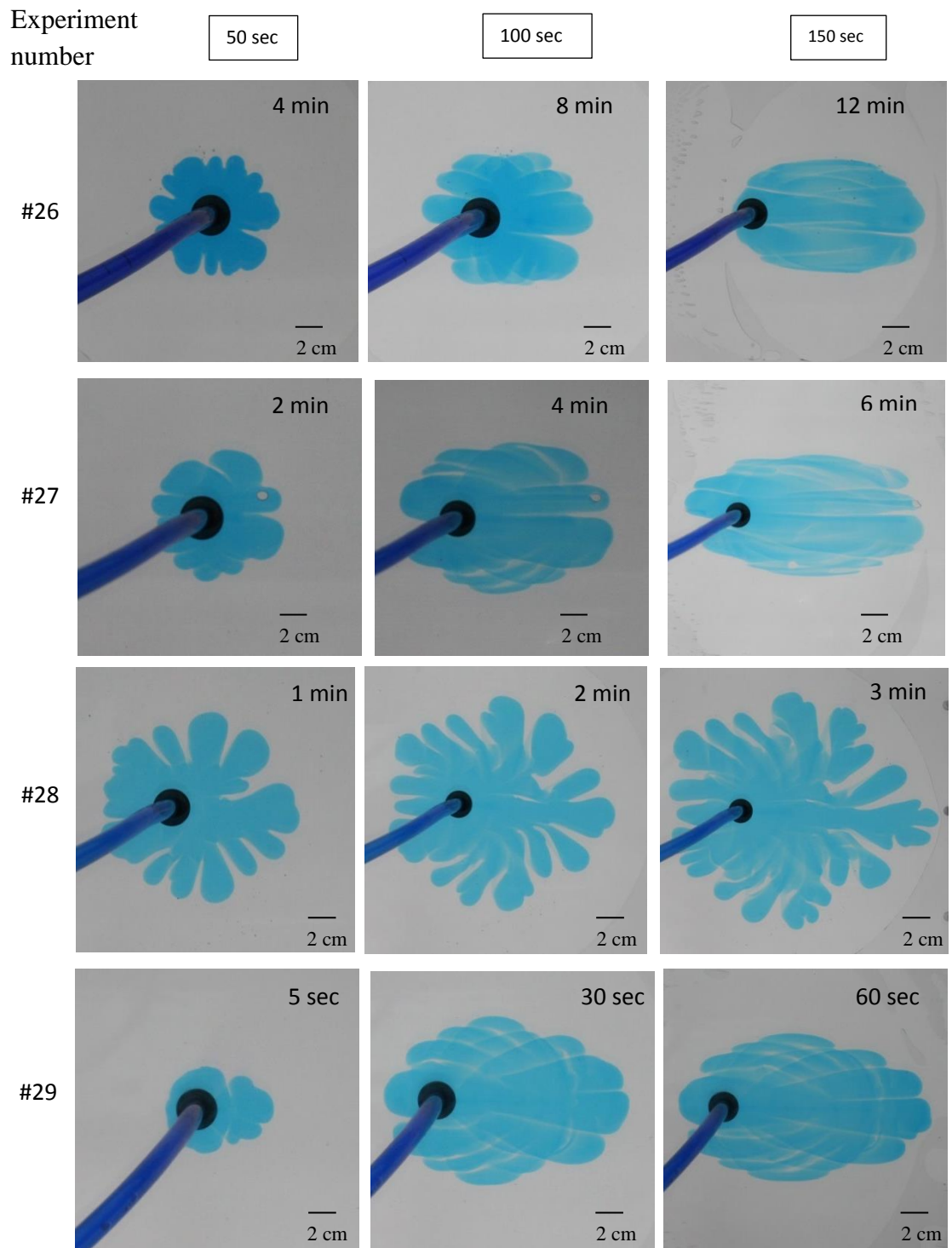


#24

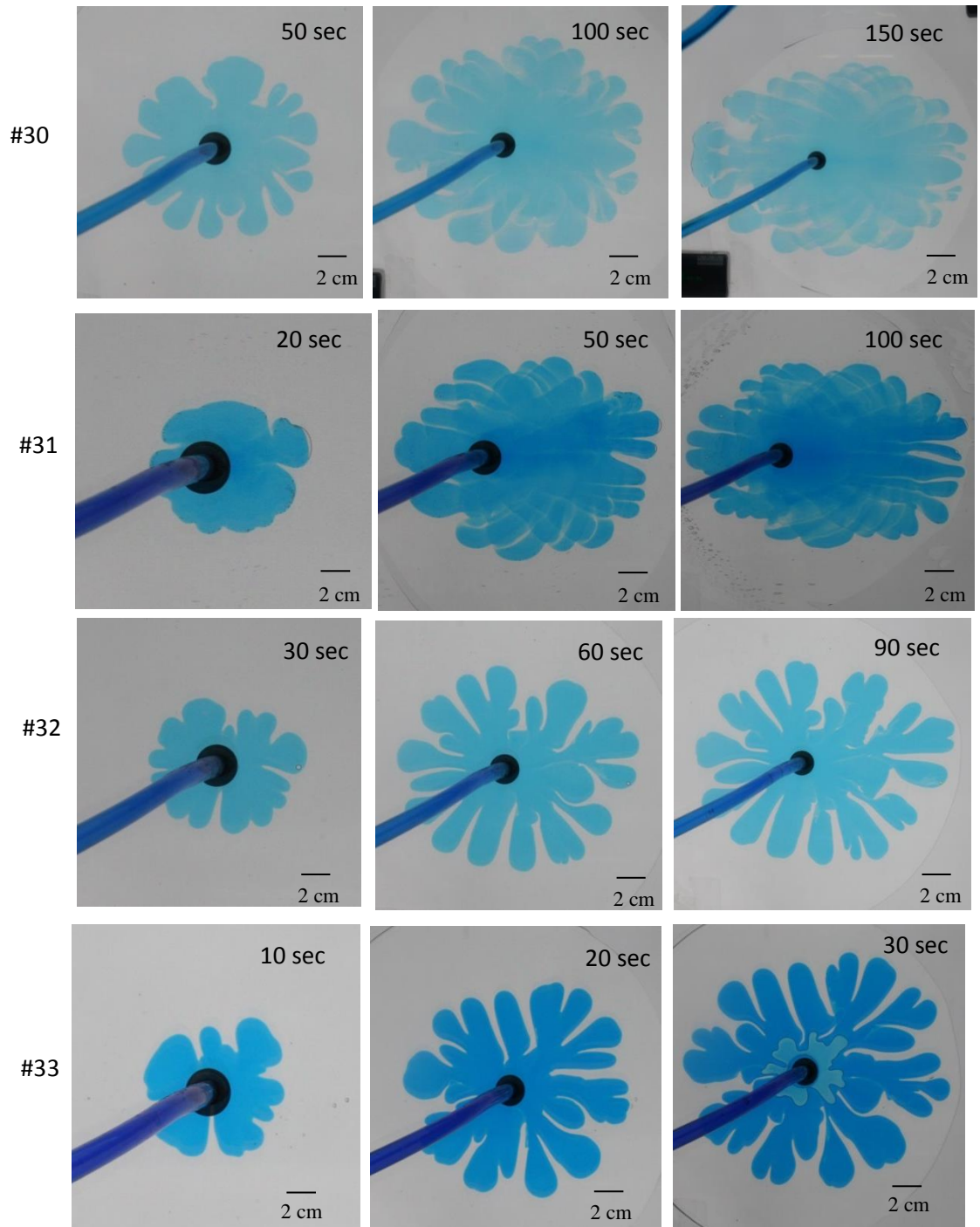


#25

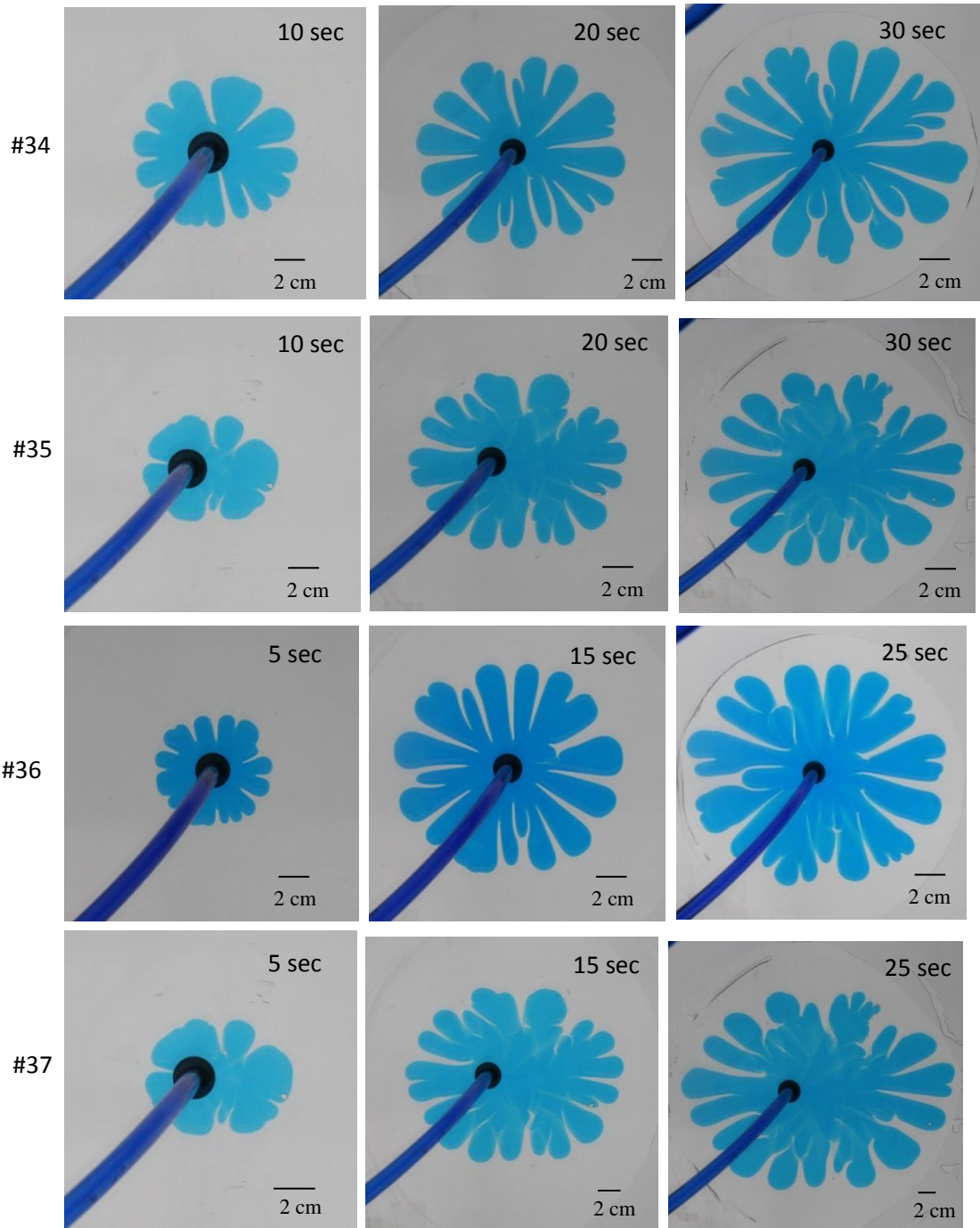




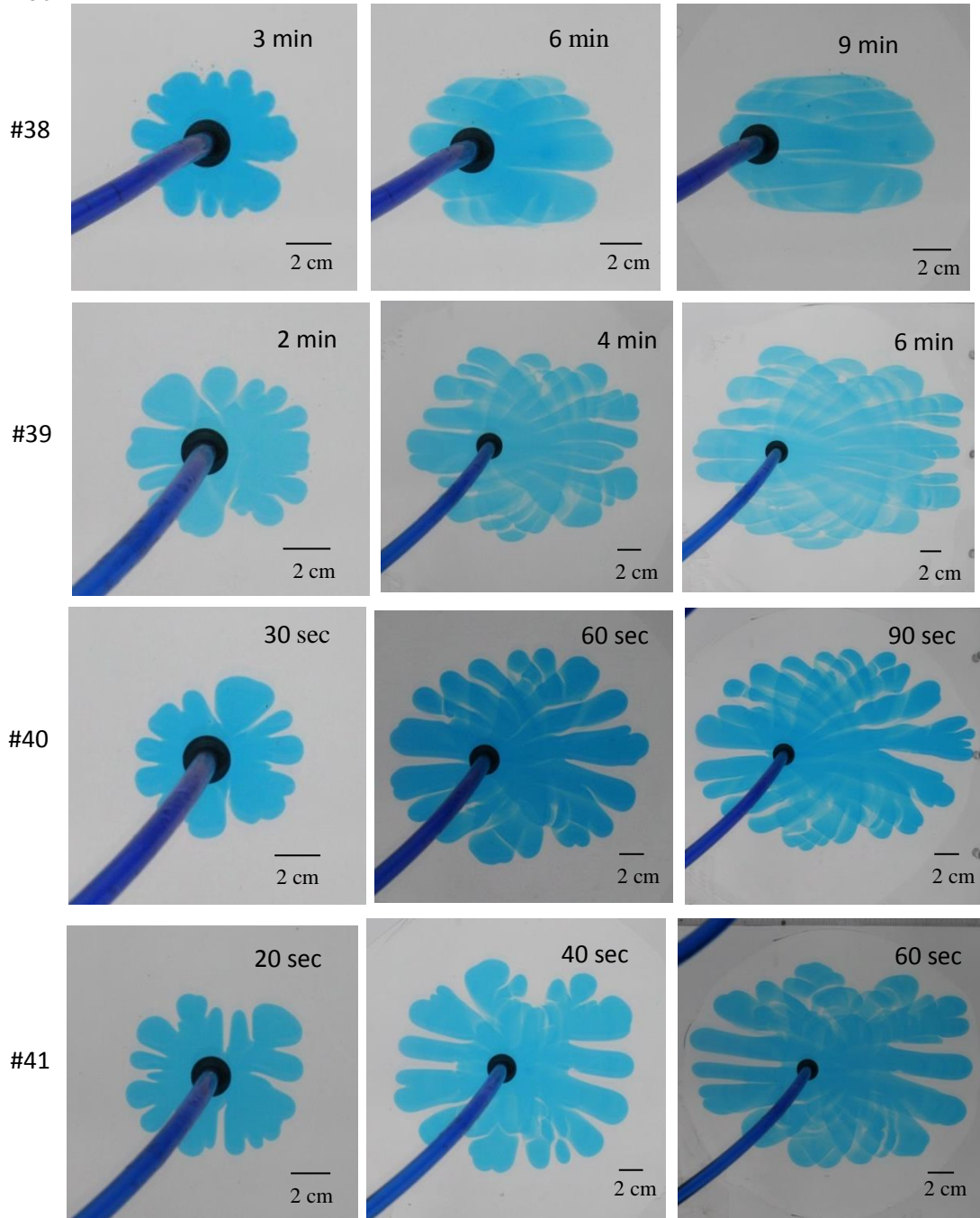
Experiment
number



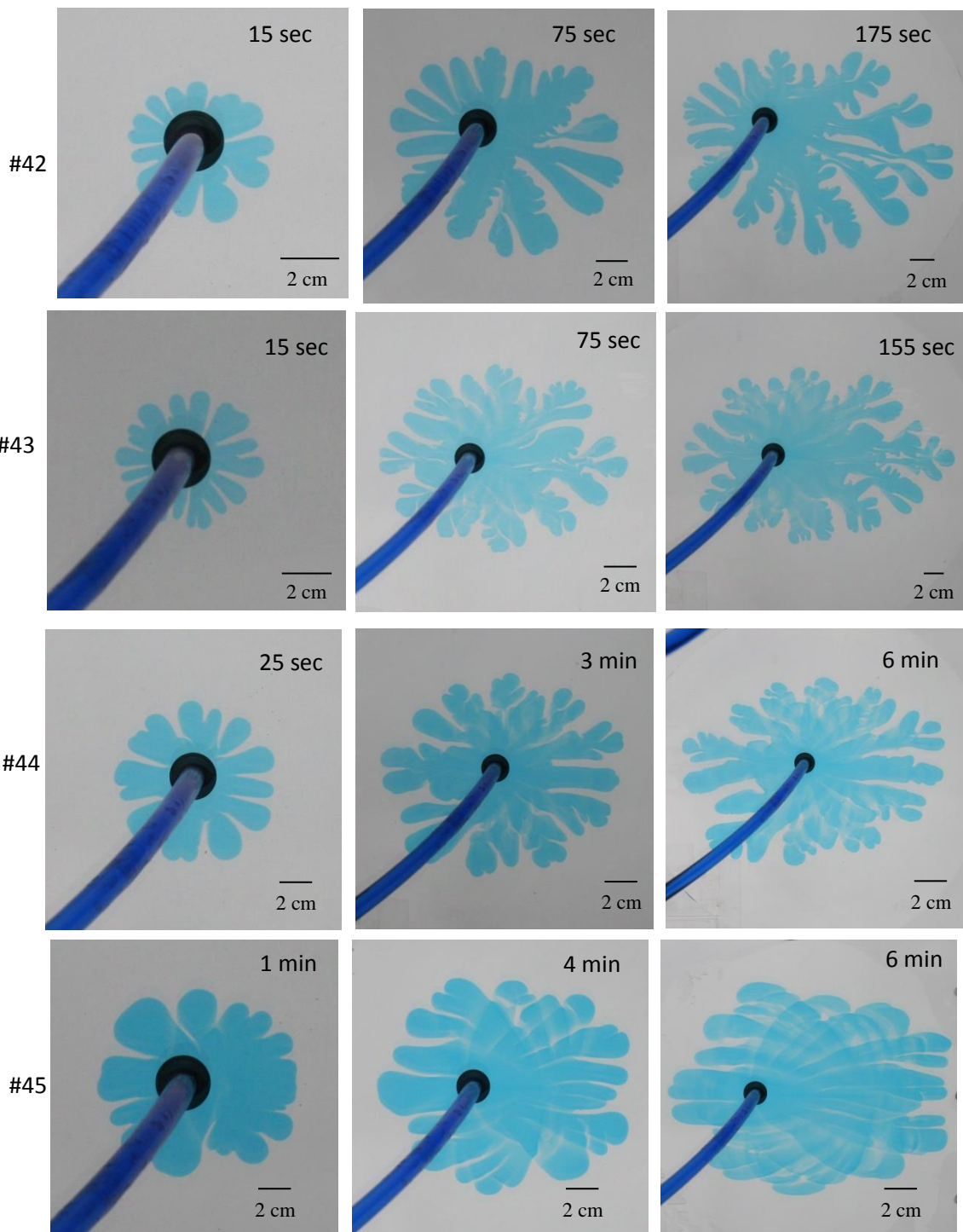
Experiment
number



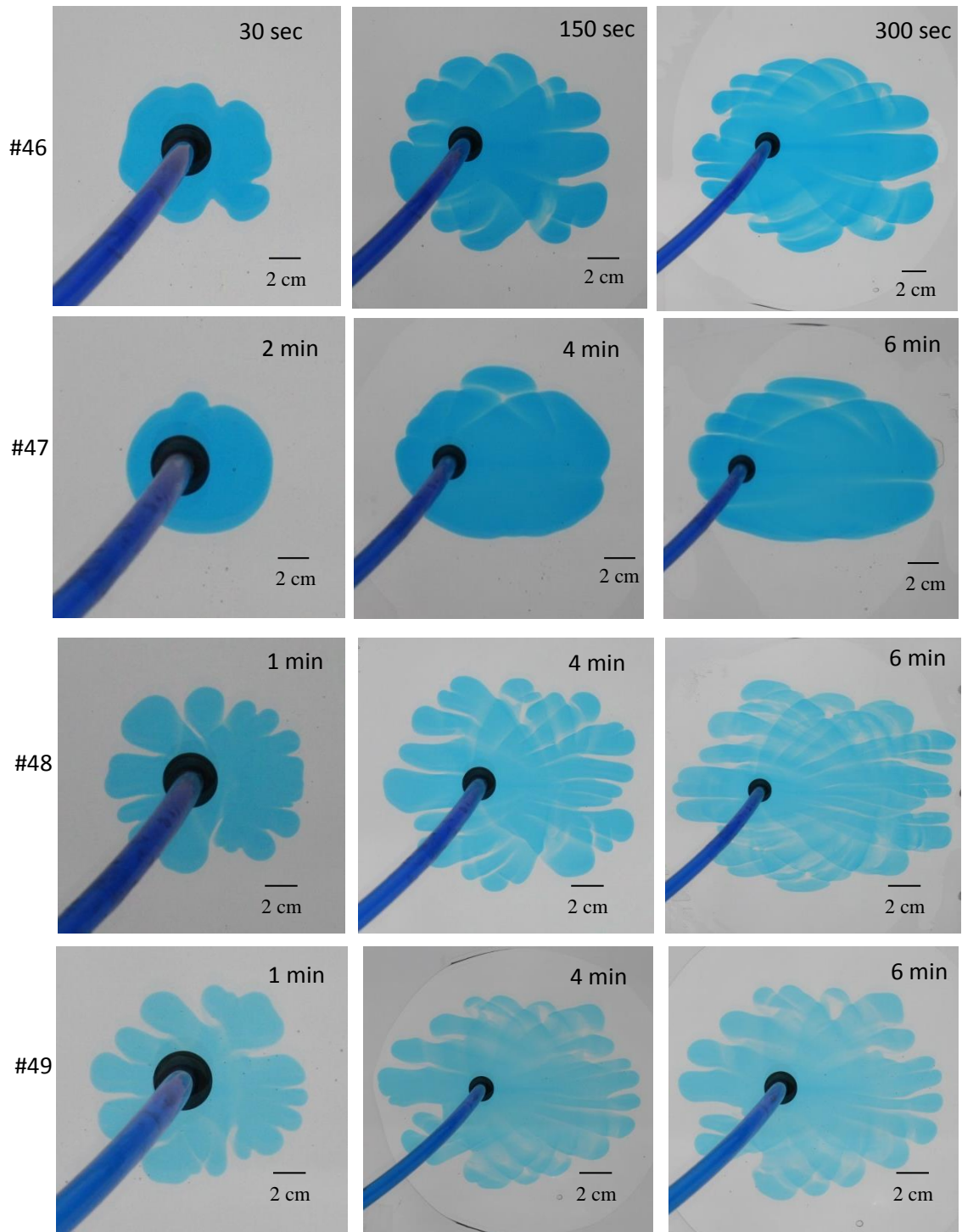
Experiment
number



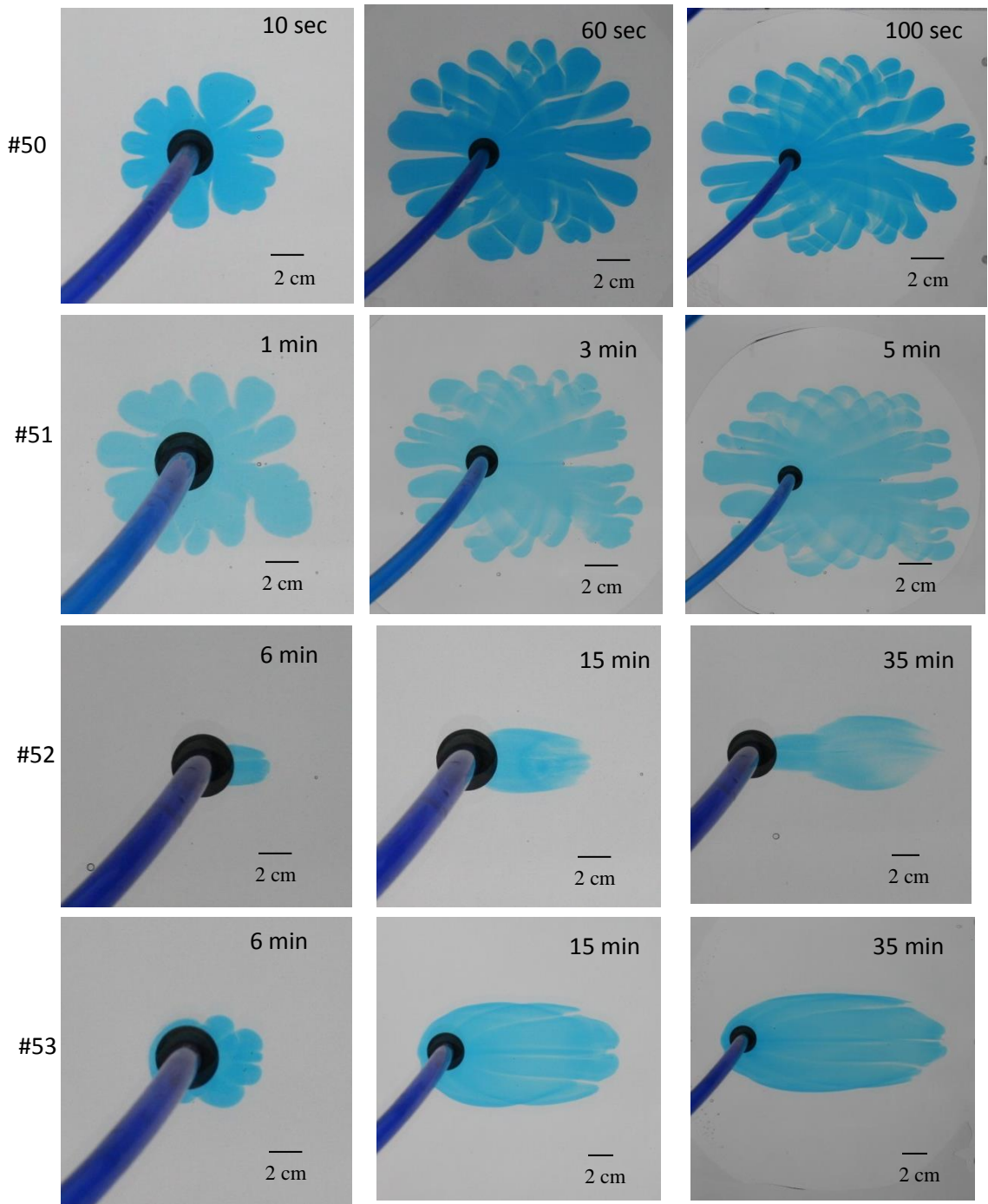
Experiment
number



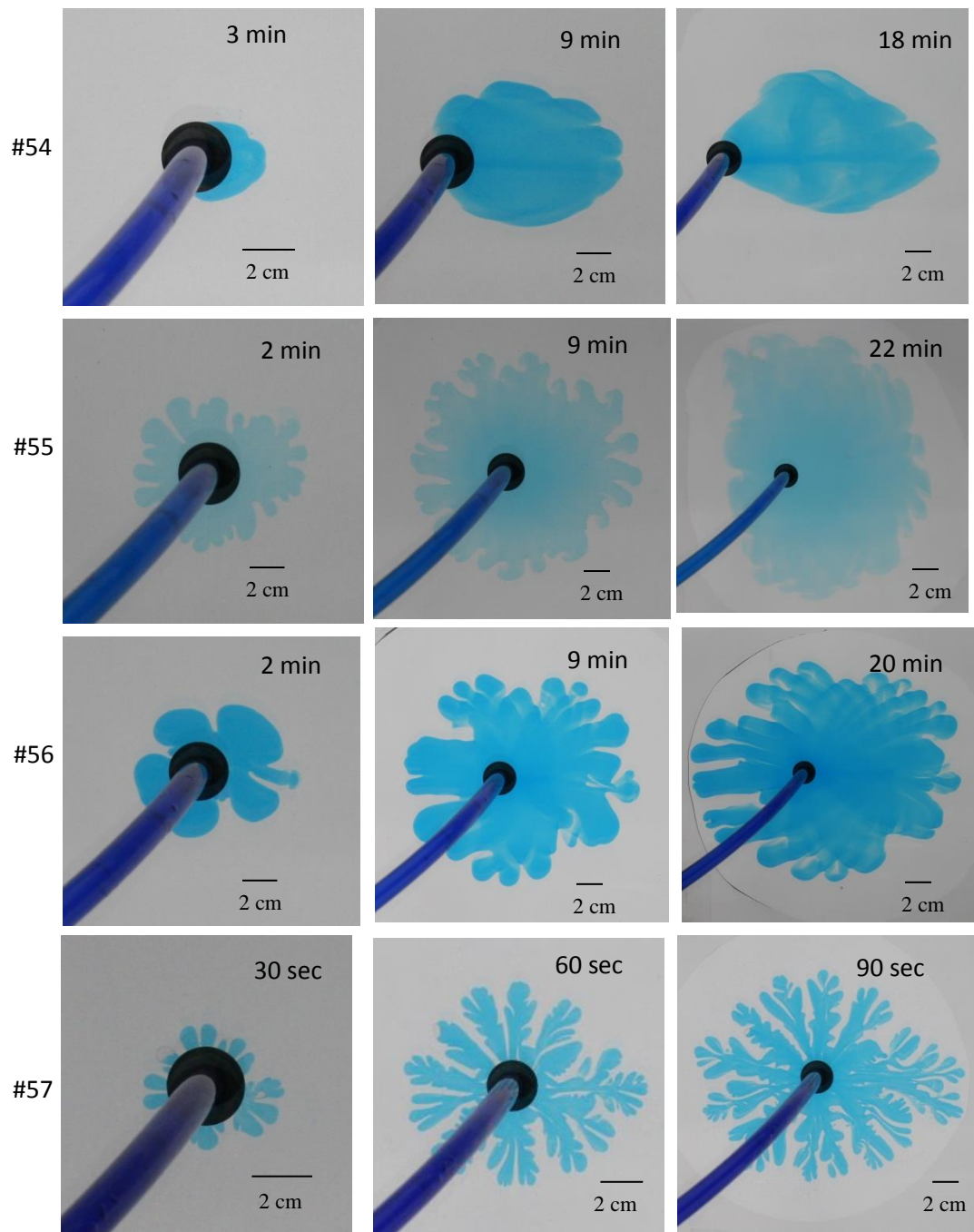
Experiment
number



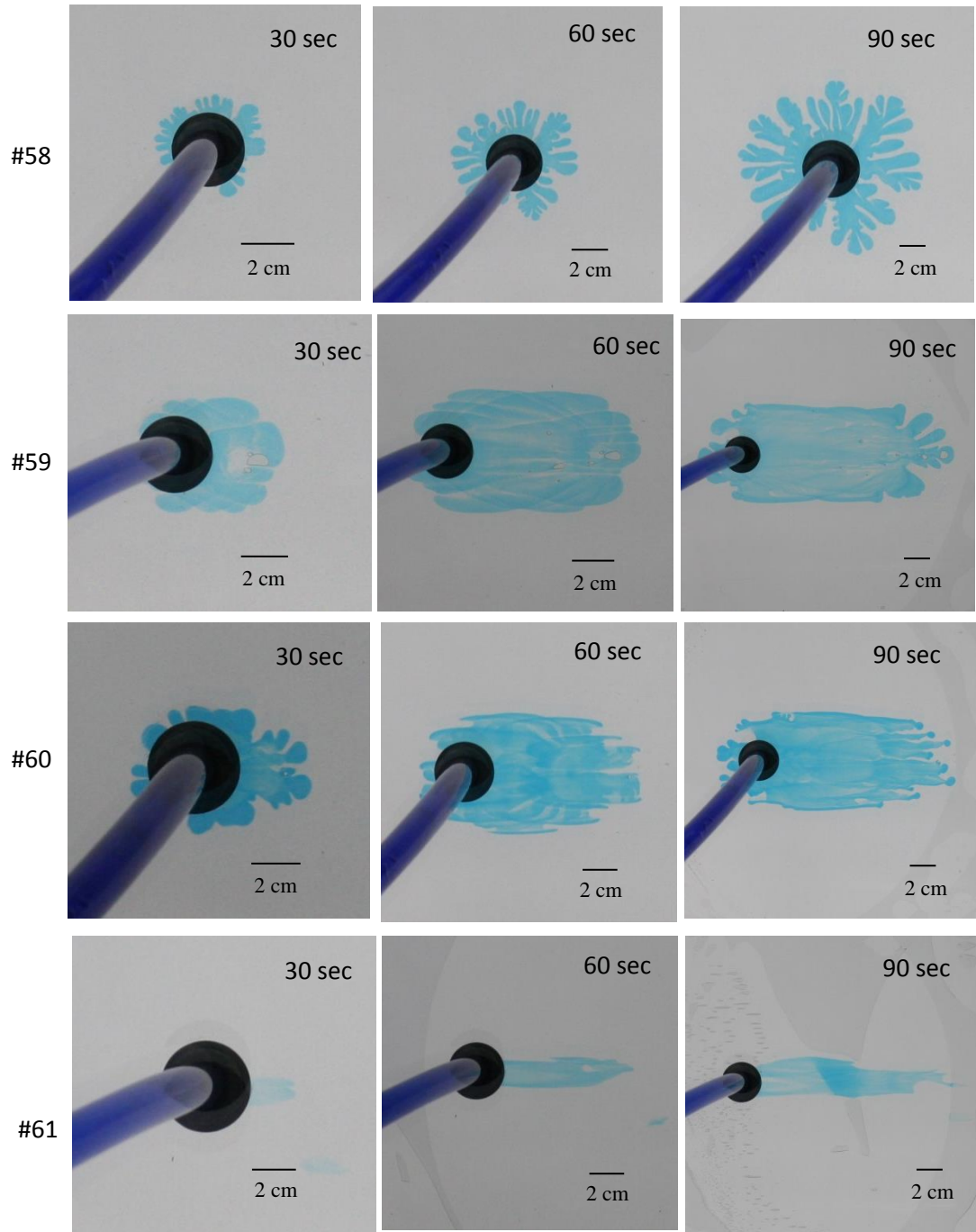
Experiment
number



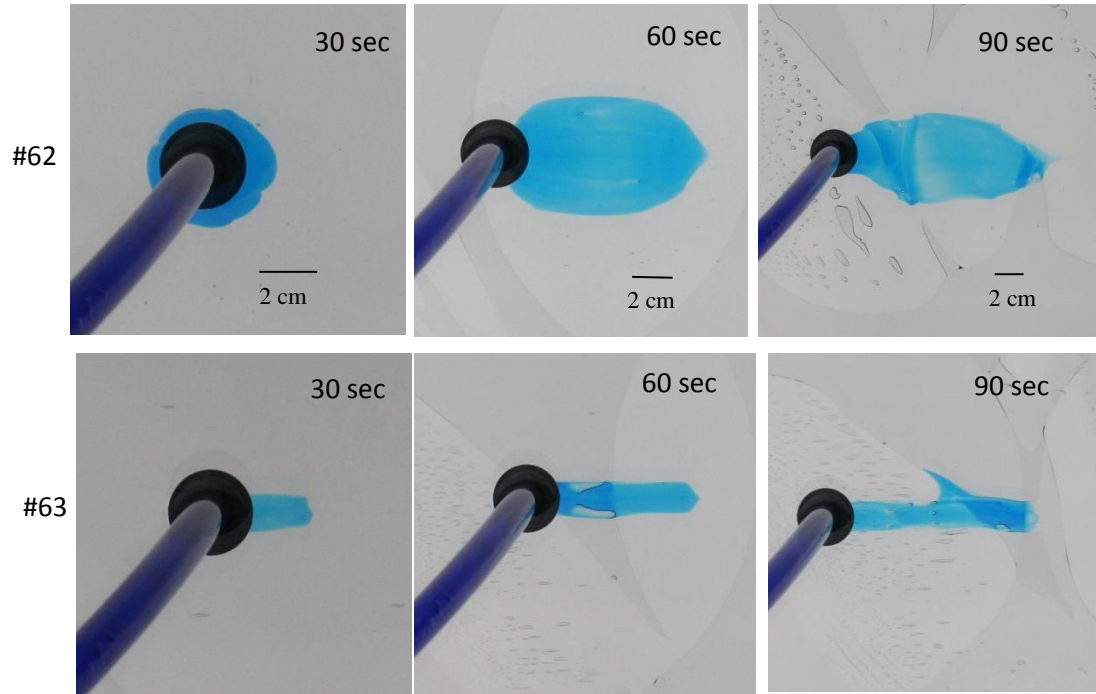
Experiment
number



Experiment
number



Experiment
number



Appendix C

Instability mechanisms,

$$\frac{dp}{dx} = \frac{-\mu U}{K} + \rho g \quad \text{Darcy's law for one dimensional steady flow}$$

$$\delta p = (\rho_2 - \rho_1) = \left[\frac{(\mu_1 - \mu_2)U}{K} + (\rho_2 - \rho_1)g \right] \delta x \quad (\text{Homsy, 1987})$$

$$U_c = (\rho_2 - \rho_1)gK / (\mu_1 - \mu_2)$$

Where, K = Permeability constant = $B^2/12$ (Chuoque et al., 1959)

B = Plate spacing

U_c = Critical velocity = R_0/t_0

R_0 = Initiation radius

$$U_c = (\rho_2 - \rho_1)gB^2/12(\mu_1 - \mu_2)$$

Solving for R_0

$$R_0 = (\rho_2 - \rho_1)gt_0B^2/12(\mu_1 - \mu_2)$$

$$R_0 = \frac{(\rho_2 - \rho_1)}{12(\mu_2 - \mu_1)} gt_0 B^2$$